BERNARDO ALAN DE FREITAS DUARTE

PHASE CHANGE MODELLING FOR NON-ISOTHERMAL FLOWS: A MATHEMATICAL, NUMERICAL AND COMPUTATIONAL MODEL FOR PURE SUBSTANCES

UNIVERSIDADE FEDERAL DE UBERLÂNDIA
FACULDADE DE ENGENHARIA MECÂNICA
2018

BERNARDO ALAN DE FREITAS DUARTE

PHASE CHANGE MODELLING FOR NON-ISOTHERMAL FLOWS: A MATHEMATICAL, NUMERICAL AND COMPUTATIONAL MODEL FOR PURE SUBSTANCES

Tese apresentada ao Programa de Pós-graduação em Engenharia Mecânica da Universidade Federal de Uberlândia, como parte dos requisitos para a obtenção do título de **DOUTOR EM ENGENHARIA MECÂNICA**.

Área de concentração: Transferência de Calor e Mecânica dos Fluidos.

Orientador: Prof. Dr. Aristeu da Silveira Neto

Uberlândia - MG
2018

Dados Internacionais de Catalogação na Publicação (CIP)
Sistema de Bibliotecas da UFU, MG, Brasil.

D812
2018

Duarte, Bernardo Alan de Freitas,
Phase change modelling for non-isothermal flows [recurso eletrônico] : a mathematical, numerical and computational model for pure substances / Bernardo Alan de Freitas Duarte. - 2018.

Orientador: Aristeu da Silveira Neto.
Tese (Doutorado) - Universidade Federal de Uberlândia, Programa de Pós-Graduação em Engenharia Mecânica.
Modo de acesso: Internet.
Disponível em: http://dx.doi.org/10.14393/ufu.te.2018.795
Inclui bibliografia.
Inclui ilustrações.

1. Engenharia mecânica. 2. Escoamento bifásico - Modelos matemáticos. 3. Escoamento bifásico - Simulação por computador. I. Silveira Neto, Aristeu da, 1955- (Orient.) II. Universidade Federal de Uberlândia. Programa de Pós-Graduação em Engenharia Mecânica. III. Título.

CDU: 621

Maria Salete de Freitas Pinheiro - CRB6/1262

UNIVERSIDADE FEDERAL DE UBERLÂNDIA
Coordenação do Programa de Pós-Graduação em Engenharia Mecânica
Av. João Naves de Ávila, nº 2121, Bloco 1M, Sala 212 - Bairro Santa Mônica, Uberlândia-MG, CEP 38400-902
Telefone: (34) 3239-4282 - www.posgrad.mecanica.ufu.br - secposmec@mecanica.ufu.br

TERMO

ALUNO: Bernardo Alan de Freitas Duarte **MATRÍCULA:** 11423EMC003

ÁREA DE CONCENTRAÇÃO: Transferência de Calor e Mecânica dos Fluidos **LINHA DE PESQUISA:** Dinâmica dos Fluidos e Transferência de Calor

PÓS-GRADUAÇÃO EM ENGENHARIA MECÂNICA: NÍVEL DOUTORADO

TÍTULO DA TESE: "Phase change modelling for non-isothermal flows: a mathematical, numerical and computational model for pure substances"

ORIENTADOR: Prof. Dr. Aristeu da Silveira Neto

A Tese foi **APROVADA** em reunião pública, realizada no auditório do Laboratório de Mecânica dos Fluidos, Bloco 5P, Campus Santa Mônica, em 09 de agosto de 2018, às 08 horas, com a seguinte Banca Examinadora:

Prof. Dr. Aristeu da Silveira Neto (orientador) - UFU

Prof. Dr. Solidônio Rodrigues de Carvalho - UFU

Prof. Dr. Aldemir Aparecido Cavallini Junior - UFU

Drª. Millena Martins Villar Vale - UFU

Prof. Dr. Guenther Carlos Krieger Filho - Poli/USP

Dr. Ricardo Serfaty - Petrobrás

Uberlândia, 09 de agosto de 2018

Documento assinado eletronicamente por **Aldemir Aparecido Cavalini Junior**, **Professor(a) do Magistério Superior**, em 09/08/2018, às 15:03, conforme horário oficial de Brasília, com fundamento no art. 6º, § 1º, do Decreto nº 8.539, de 8 de outubro de 2015.

Documento assinado eletronicamente por **Solidonio Rodrigues de Carvalho**, **Professor(a) do Magistério Superior**, em 09/08/2018, às 15:36, conforme horário oficial de Brasília, com fundamento no art. 6º, § 1º, do Decreto nº 8.539, de 8 de outubro de 2015.

Documento assinado eletronicamente por **GUENTHER CARLOS KRIEGER FILHO**, **Usuário Externo**, em 09/08/2018, às 16:54, conforme horário oficial de Brasília, com fundamento no art. 6º, § 1º, do Decreto nº 8.539, de 8 de outubro de 2015.

Documento assinado eletronicamente por **Aristeu da Silveira Neto**, **Professor(a) do Magistério Superior**, em 10/08/2018, às 07:36, conforme horário oficial de Brasília, com fundamento no art. 6º, § 1º, do Decreto nº 8.539, de 8 de outubro de 2015.

Documento assinado eletronicamente por **Millena Martins Villar Vale**, **Usuário Externo**, em 10/08/2018, às 08:03, conforme horário oficial de Brasília, com fundamento no art. 6º, § 1º, do Decreto nº 8.539, de 8 de outubro de 2015.

Documento assinado eletronicamente por **ricardo serfaty**, **Usuário Externo**, em 10/08/2018, às 10:39, conforme horário oficial de Brasília, com fundamento no art. 6º, § 1º, do Decreto nº 8.539, de 8 de outubro de 2015.

A autenticidade deste documento pode ser conferida no site https://www.sei.ufu.br/sei/controlador_externo.php?acao=documento_conferir&id_orgao_acesso_externo=0, informando o código verificador **0633263** e o código CRC **E46CEA01**.

"Energy cannot be created or destroyed, it can only be changed from one form to another."

Albert Einstein

Aknowledgments

First, I would like to thank God for allowing me to live great experiences in Uberlândia. I thank my supervisor, Prof. Dr. Aristeu da Silveira Neto, for the constant example of dedication and respect. For providing the support in the present work, I thank the Graduate Mechanical Engineering program, specially the Laboratory of Fluid Mechanics (MFLab) of UFU (Federal University of Uberlândia).

I would like to thank my family for the inconditional love. I thank my mother Iara for her sweetness, my father João for his trust and my sister Gisele for the complicity. I thank my fiancé Pedro for teaching me that life has meaning only when we put love above all. In memory, I thank my mother-in-law Beatriz who taught me that a new day brings possibility to everything goes right.

I thank my friend Hélio Ribeiro Neto for being good and kind to me whenever I needed. For all the colleagues and staff from MFLab, I'm deeply gratefull for each moment lived. I'm also gratefull to my master degree supervisor, Hersília de Andrade e Santos, who told me about the Graduate Mechanical Engineering program of UFU.

Finally, I thank the financial support from CNPQ, CAPES, FAPEMIG and PETROBRAS to conduct the present work.

DUARTE, B.A.F., **Phase change modelling for non-isothermal flows: A mathematical, numerical and computational model for pure substances.** 2018. 178 f. Tese de Doutorado, Universidade Federal de Uberlândia, Uberlândia.

RESUMO

A dinâmica de fluidos computacional é uma importante ferramenta para o estudo de escoamentos presentes na natureza e em aplicações de engenharia. A modelagem computacional de problemas típicos de engenharia permite aumentar a eficiência de processos produtivos e de equipamentos em diversos setores da economia. Além disso, o estudo de características fundamentais de escoamentos possibilita a criação de um arcabouço teórico importante para diversas linhas de pesquisa dessa área. Nos últimos anos, a modelagem de problemas de mudança de fase tem sido conduzida utilizando modelos computacionais. Na presente tese de doutorado, foi desenvolvido um modelo matemático, numérico e computacional de escoamentos não-isotérmicos com mudança de fase. O código MFSim foi utilizado para a performance de todas as simulações computacionais e o cluster do Laboratório de Mecânica dos Fluidos (MFLab) foi empregado para a execução das simulações na Universidade Federal de Uberlândia (UFU). O modelo computacional foi verificado e validado com inúmeros casos da literatura. Finalmente, um complexo caso de condensação de contato direto (DCC) em cross-flow foi conduzido, demonstrando a potencialidade do código MFSim para modelar até mesmo problemas de grande complexidade. Problemas de ebulição de líquido ao redor de uma bolha de vapor foram utilizados para vallidação com solução teórica e analítica. Os resultados do presente trabalho apresentaram baixos desvios em relação aos resultados prévios da literatura. Correntes espúrias foram investigadas e quantificadas. Finalmente, forças particulares a problemas de mudança de fase em CFD foram quantificadas e sua influência nos problemas estudados foram nulas mesmo para situações críticas.

Palavras chave: CFD, DCC, ebulição, condensação, bolhas, força de recuo.

ABSTRACT

The Computational Fluid Dynamic (CFD) is an important methodology to study the characteristics of flows in nature and in several engineering applications. Modelling non-isothermal flows may be usefull to predict the main flow dynamics which allows the improvement of efficiency in equipments and processes for industrial purpose. In addition, investigations using computational models may provide key information about the fundamental characteristics of flow, developing the theoretical groundwork of physical processes. In the last years, the topic of phase change has been intensively studied using CFD due to the computational and numerical advances reported in the literature. In the present work, phase change is studied using a mathematical, numerical and computational model developed in this thesis. The homemade code MFSim was used to run all the computational simulations in the cluster from the Fluid Mechanics laboratory (MFLab) from the Federal University of Uberlandia (UFU). The computational model was verified and validated against several cases from the literature. The model developed in the present thesis showed results with high accuracy and low differences compared to previous works in the literature. After the performance of several validation cases, some topics were deeply investigated. Finally, a complex case study of Direct contact condensation (DCC) was studied and the computational model provided accurate results compared to the literature. The present thesis reported the advances on modelling computationally the topic of phase change using the homemade code MFSim and several interesting conclusions were developed and some numerical issues were overcame. Boiling cases were validated against theoretical and analytical solution from the literature. The results show low deviations compared to the references. Finally, spurious currents magnitude were quantified for phase change problems and particular forces due to phase change were investigated. The results show null importance of these forces in the phase change model studied.

Keywords: CFD, DCC, boiling, condensation, bubble, recoil force.

List of Figures

List of Tables

LIST OF SYMBOLS

Abbreviations

A	Atwood number
AMR	Adaptive mesh refinement
CFD	Computational Fluid Dynamic
CSF	Continuum surface force method
CFL	Courant-Friedrich-Lewis condition
DCC	Direct Contact Condensation
DHC	Differentially heated cavity
Delta	Delta function method
DOI	Digital Object Identifier
GFM	Ghost Fluid method
Gr	Grashof number
Ja	Jakob number
LES	Large eddy simulations
MFLab	Fluid Mechanics Laboratory of UFU
NOB	Non-Oberbeck-Boussinesq approximation
OB	Oberbeck-Boussinesq approximation
PLIC	Piecewise-linear interface calculation method
Pr	Prandtl number
Ra	Rayleigh number
STP	Standart temperature pressure
UFU	Federal University of Uberlandia
VOF	Volume of Fluid method
We	Weber number

Subscript

con	Continuos phase
dis	Dispersed phase
l	liquid phase
v	Vapor phase

Greek letters

α	volumetric fraction
β	volumetric expansion coefficient
Cp	Specific heat capacity $[J/kg]$
ε	relative error $[\%]$
ρ	specific mass $[kg/m^3]$
μ	dynamic viscosity $[kg/ms]$
η	AMR efficiency $[\%]$
k	Thermal conductivity $[W/mK]$
κ	interface curvature
L	Latent heat $[J/kg]$
ψ	indicator function (VOF)
δ	Delta de Dirac
σ	superficial tension coefficient

Mathematical operators

∂	gradient
∇	gradient
∇^2	Laplacian
$\int$	integral

SUMMARY

CHAPTER I

INTRODUCTION

These chapter describes the objectives, justification, originality, highlights and organization of the thesis. The objective subsection describes the main and secondary objectives; the justification subsection presents the arguments supporting the thesis motivation; the highlights subsection shows the main topics investigated in the present work; finally, the organization subsection describes the arrangement employed in the thesis composition.

The present work was focused on modelling mathematically, numerically and computationally phase change in non-isothermal flows. The study was restricted to investigate flows considering pure substances and monocomponent fluids. The continuos hypothesis was adopted and the fluids were considered Newtonian.

According to the First Law of the Thermodynamic, the energy from a given system cannot be created or destroyed, since it can only be transformed from one form to another. There are several phenomena in nature and in engineering applications where one form of energy is converted to another, respecting the principle of total energy conservation.

The phase change phenomenon is a common example of an energy conversion process, where a certain amount of sensible energy is converted to latent energy, leading to complex chemical reactions (PAN; WEIBEL; GARIMELLA, 2016). The main consequence of the phase change process is the modification of the physical state of a given substance (POLING; PRAUSNITZ; O'CONNELL, 2001).

When flow is subjected to phase change, its physical state is modified and the fluid properties are modified where the phase transition occured. It's imperative to study the phase change phenomenon since the phase change process may deeply modify the fluid properties in the region where phase transition occurs. Water, for example, at Standart Temperature Pressure (STP) condition, presents specific mass of approximately $1000kg/m^3$ when is liquid; however, water vapour presents specific mass of approximately $1.5kg/m^3$ (POLING; PRAUSNITZ; O'CONNELL, 2001). In addition, phase change may severely modify the temperature field affecting the flow dynamics of several phenoma. In the present thesis, the phase change phenomenon was studied from a mathemathical, numerical and computational model developed which was applied to the in house code MFSim.

1.1 Objectives

The present work aimed to achieve one general objective and seven specific objectives. These objectives were described in details in the following subsections.

1.1.1 General objective

The main objective of the present work was to develop a mathematical, numerical and computational model of non-isothermal two-phase flows subjected to phase change. The MFSim code was the plataform chosen to the computational implementation of the model developed in the present thesis, as well as the model verification and validation.

1.1.2 Specific objectives

The following objectives were defined for the present work:

1. Develop a bibliographic revision about the state of art of computational modelling non-isothermal two-phase flows and phase change;
2. Develop the thermal energy module in the MFSim code and perform verification and validation cases;
3. Develop a model to predict specific mass variations due to temperature variations and apply the model in the MFSim code;

4. Develop a mathematical, numerical and computational model of two-phase flows with phase change;

5. Include the phase change model in the MFSim code and perform validation cases;

6. Compose scientific papers and reports from the results obtanied in the present work;

7. Compose the thesis.

1.2 Justification

The present thesis was the first work focused on the study of non-isothermal flows with phase change in the research group from the Fluid Mechanics Laboratory (MFLab) in the Federal University of Uberlandia (UFU). MFLab research group has a strong insertion in mathematical, numerical and computational methodologies for general fluid mechanics problems and most part of its motivation has been research projects related to the brazilian industry. However, the influence of phase change process and temperature field variations have been generally not taken into consideration in the previous investigations conducted before the present thesis; since the purpose of the previous works were restricted to evaluate other variables of interest.

Recently, some research problems from MFLab projects have required the study of some complex phenomena where phase change is relevant to the fluid dynamics of flow. Then, the justification of the present thesis is the development of the initial steps of a new research line in the MFLab group where phase change is studied.

The main contributions from the present work was the development of a energy equation module as well as a phase change module in the MFSim code, allowing to study several important engineering applications.

1.3 Originality of the present thesis

According to the thesis objectives, several original contributions were proposed to be achieved at the end of the present work. The major contributions expected from the present thesis were the investigation of the following items:

1. Mathematical, numerical and computational methodologies of a temperature-dependent specific mass approach for non-isothermal flows;

2. Mathematical, numerical and computational methodologies for flows subjected to phase change;

3. Evaluation of the influence of dimensionless parameters in non-isothermal flows such as the Grashof, Prandtl, Nusselt and Jakob numbers.

Additional original contributions were obtanied according to the thesis progression in time, such as the following items:

1. Investigation of the recoil force in phase change problems;

2. Evaluation of a particular effect in phase change problems when using the non-divergent form of momentum equation;

3. Computation of adaptive mesh refinement (AMR) efficiency in phase change simulations using MFSim code

4. Comparison between two different approaches of pressure interface treatment in phase change problems.

The introduction of a phase change model in the MFSim code was itself an original contribution in the brazilian research scenario, since few relevant publications from Brazil of flows with pure substances subjected to phase change have been found in the main cientific databases (ISI Web of Knowlegde and ScienceDirect).

The later topics provided the production of relevant information for composing papers which are in progress of publication in some scientific journals. One paper was published in the Journal of the Brazilian Society of Mechanical Sciences and Engineering (10.1007/s40430-018-1181-x). There is another work under review in the International Journal of Multiphase flows. In addition, three papers were published in the 24th ABCM International Congress of Mechanical Engineering and another paper was published in the 57th Brazilian Conference of Chemistry.

1.4 Highlights

In this section, some results-oriented points were presented to provide the readers an overview of the main findings of the present thesis.

1.4.1 Grashof number influence in local thermal transfer rate

In single-phase flows, the increase of Grashof number increases the local thermal transfer rate and isotherms pattern. Figure 1.1 illustrates the isotherms for different Grashof numbers in a simulation of natural convection of single-phase flow.

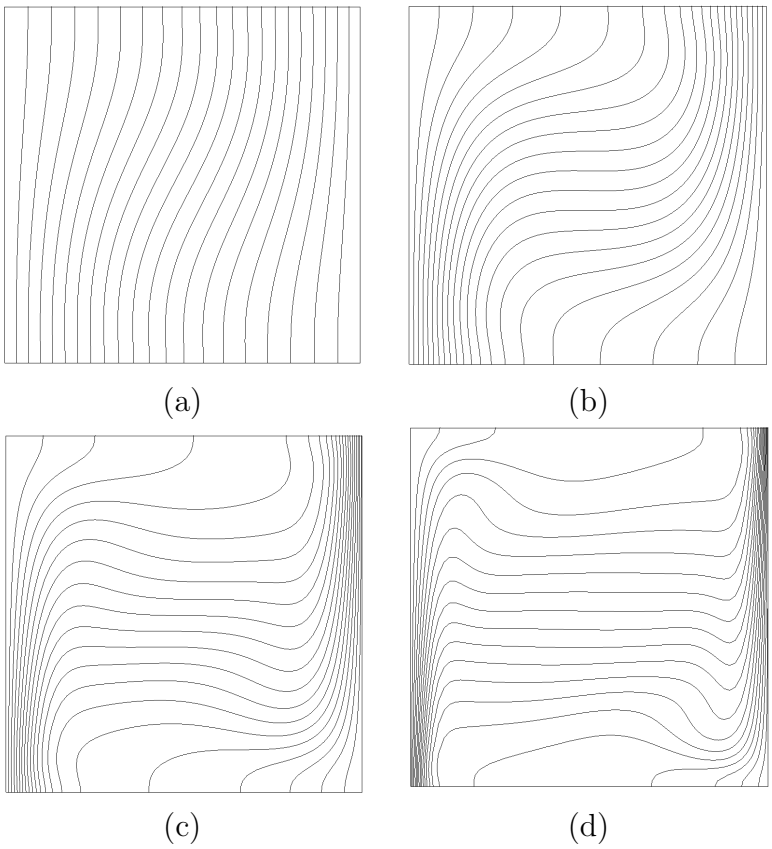

Figure 1.1: Central slice showing isotherms considering Pr=0.71 and Gr=1.4×10^3 (a), Gr=1.4×10^4 (b), Gr=1.4×10^5 (c), Gr=1.4×10^6 (d).

In two-phase flows, the inclusion of a dispersed phase with lower Grashof number than the continuos phase lowered the local thermal transfer rate. Figure 1.2 shows the isotherms in a case of natural convection with a bubble considering an initial radius of $0.15L$ and $0.31L$, respectively.

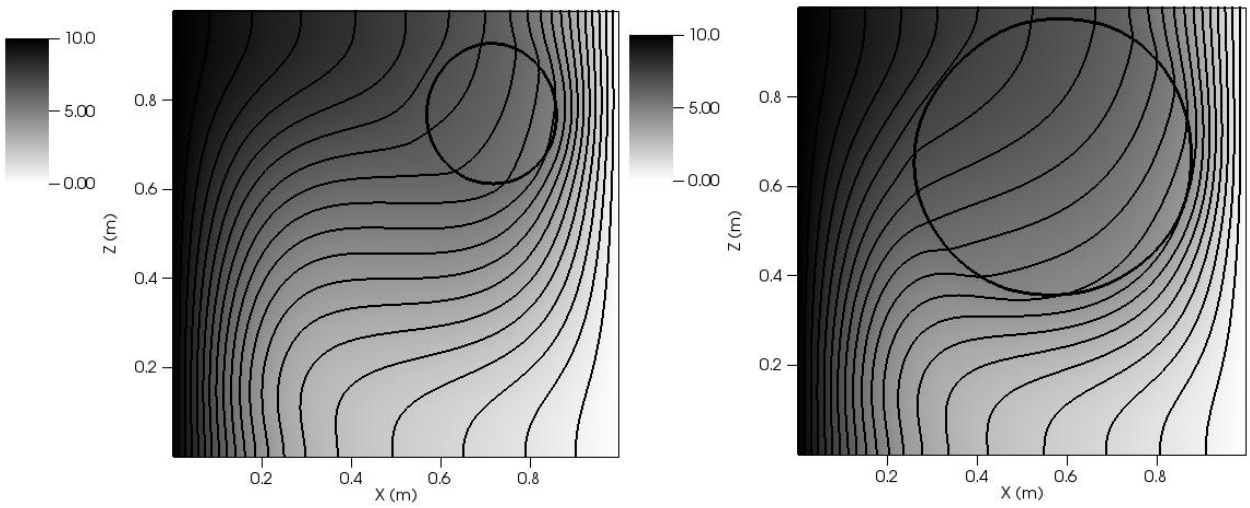

(a) (b)

Figure 1.2: Isotherms at central xz-plane for $r = 0.15L$ (a) and $r = 0.31L$ (b). Interface is represented by a contour line.

1.4.2 Atwood number influence in the development of a Rayleigh-Taylor instability

The increase of Atwood number increases the intensity of the baroclinic torque and the speed of the developement of the Rayleigh-Taylor instability. In addition, the simulation with higher Atwood number presented a higher local thermal transfer rate. Figure 1.3 shows the velocity field for the simulations of Rayleigh-Taylor instability for Atwood number of 1 and 0.33, respectively.

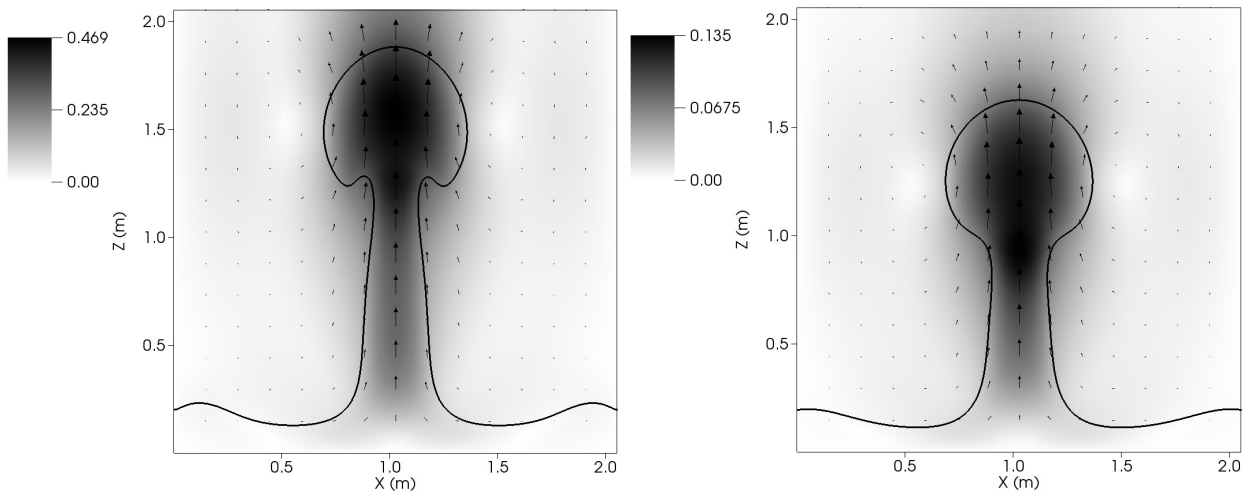

(a) (b)

Figure 1.3: Velocity vectors at central xz-plane for $A = 1.0$ (a) and $A = 0.33$ (b). Interface is represented by a contour line.

1.4.3 Prandtl number influence in local thermal transfer rate

In two-phase flows, the introduction of a dispersed phase with different Prandtl number than the continuos phase may affect the local thermal transfer rate. The inclusion of a dispersed phase with lower Prandlt number than the continuos phase would reduce the local thermal transfer rate; as well as, the inclusion of a dispersed phase with a higher Prandtl number than the continuos phase would increase the local thermal transfer rate.

Figure 1.4 shows the isotherms for the case where the inclusion of a dispersed phase have increased and reduced the local thermal transfer rate, respectively.

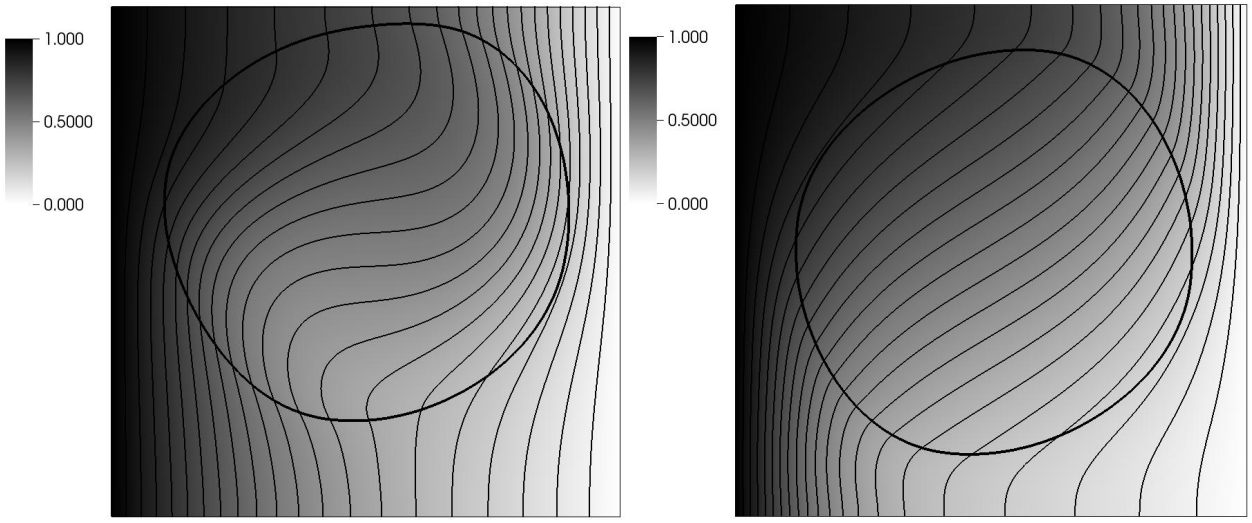

(a) (b)

Figure 1.4: Isotherms at central xz-plane for the case of thermal transfer increase (a) and reducement (b). Interface is represented by a contour line.

1.4.4 Benchmark between Oberbeck-Boussinesq approximation (OB) X new temperature-dependent specific mass approach (NOB)

A new temperature-dependent specific mass approach showed results with higher accuracy than OB, indicating that the variations of specific mass in energy and momentum equations are relevant, particularly for turbulent flows. The analysis of the flow for a large range of Rayleigh number was performed and a typical turbulent structure was found in the turbulent regime. Figure 1.5 shows the presence of Tollmien–Schlichting instability for turbulent flow ($Ra = 10^{10}$).

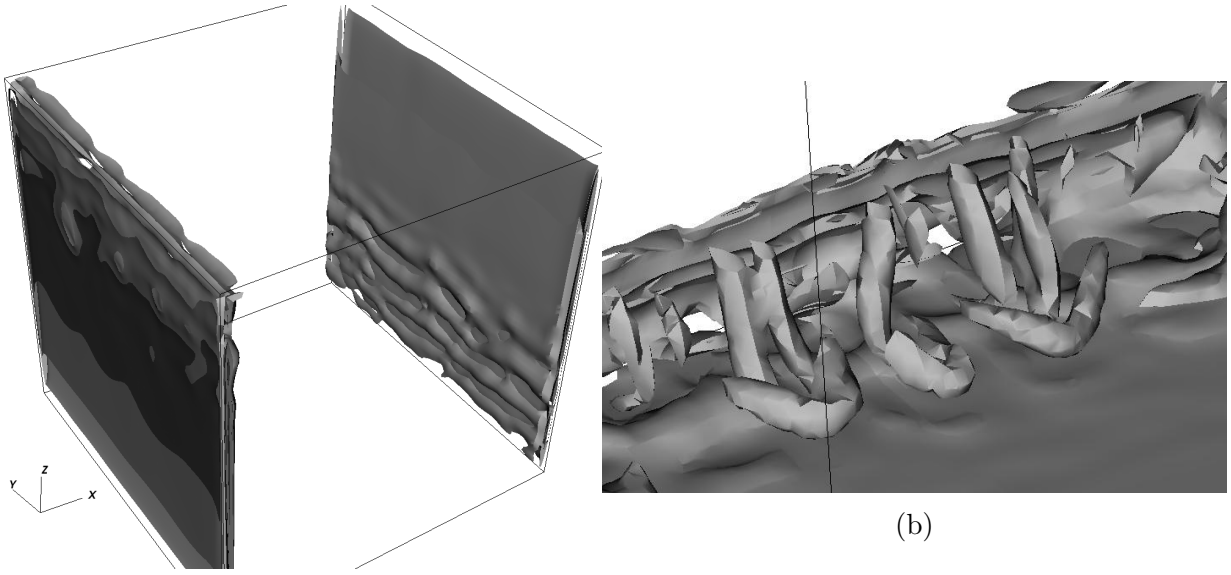

(a) (b)

Figure 1.5: Tollmien–Schlichting instability in a case of single-phase flow natural convection.

1.4.5 Particular forces in phase change problems included in the computational model

The present work has described for the first time in the literature the importance of an additional force due to the use of the non-divergent form of momentum equation when phase change occurs. The magnitude of the force was quantified and its importance was evaluated in some test cases.

In additional, the recoil force was investigated. The recoil force effects were also measured in phase change simulations and its magnitude was compared to the effects of interfacial tension force.

1.4.6 Evaluation of spurious currents in phase change problems

A diffuse and a sharp interface treatment for pressure were evaluated in phase change problems.

Figure 1.6 shows the spurious currents in phase change simulations considering a constant mass density flux of $10.0 kg/m^2 s$.

1.4.7 Calculation of the adaptive mesh refinement efficiency in several problems

Adaptive mesh refinement efficiency was computed and compared to previous works in the literature. Figure 1.7 illustrates the mesh configuration at the beggining and at the end of a

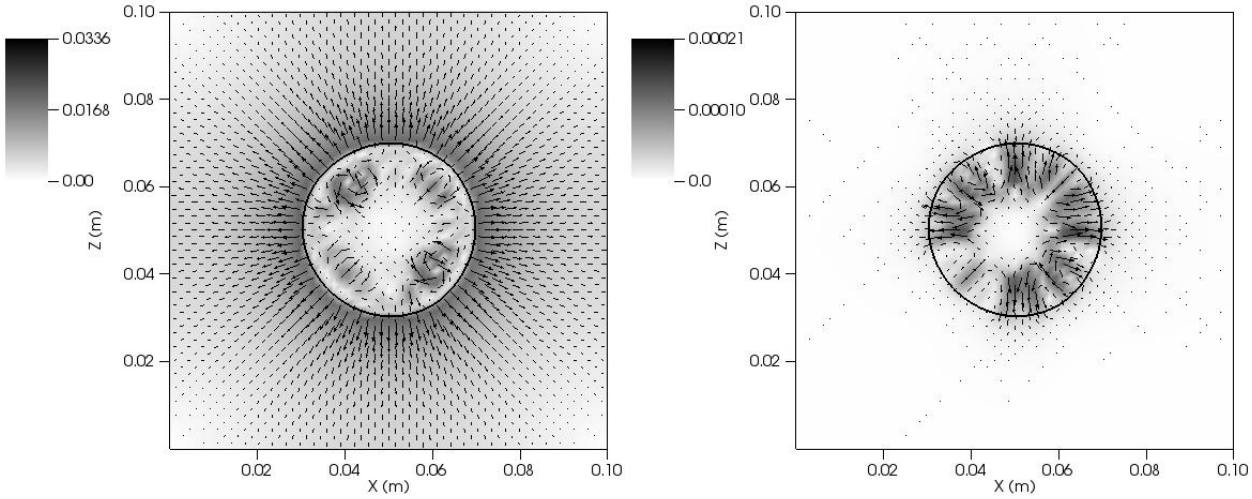

(a) (b)

Figure 1.6: Spurious currents in phase simulations considering $\dot{m}' = 10.0$ using a diffuse (a) and a sharp (b)interface treatment.

simulation of a Rayleigh-Taylor instability.

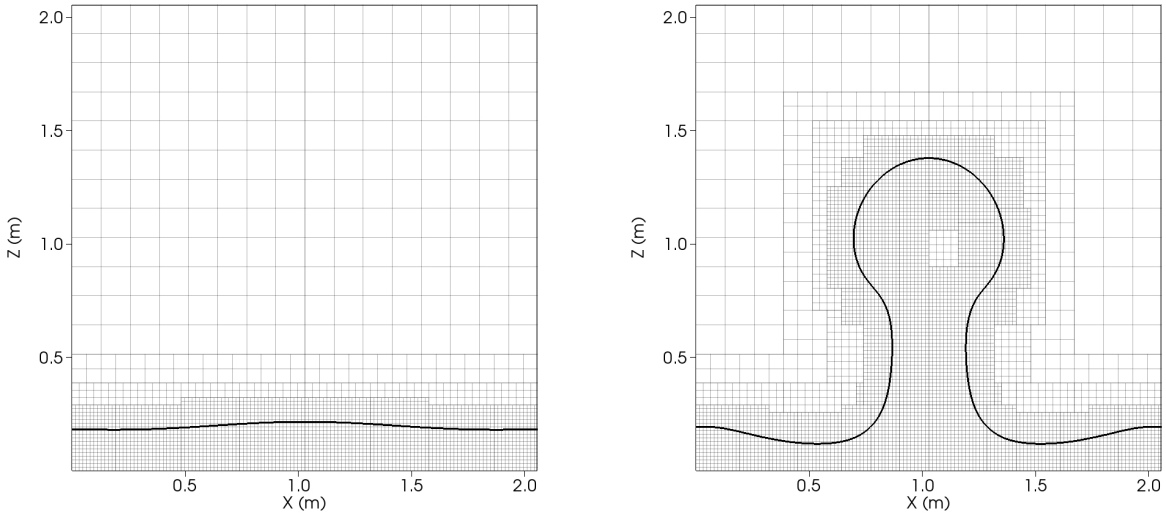

(a) (b)

Figure 1.7: Interface and mesh configuration (a) at the initial time of the simulation and (b) at the final time.

1.4.8 Film boiling simulations using AMR

Film boiling simulations were performed and the two typical structures (bubble and spikes) of Rayleigh-Taylor instability were identified. Fig. 1.8 shows the interface contour and the grid configuration employed at the initial time of the simulation and at the final time.

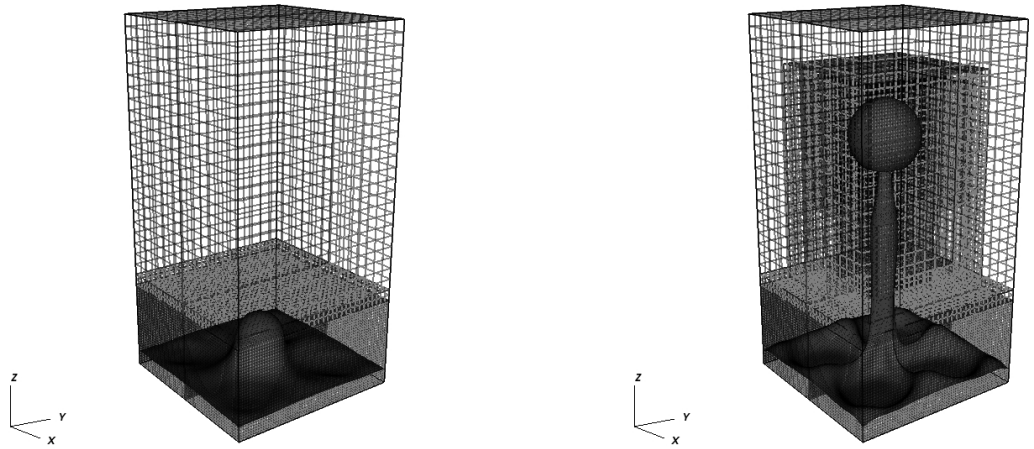

(a) (b)

Figure 1.8: Interface and mesh configuration (a) at the initial time of the simulation and (b) at the final time.

1.4.9 Simulation of a water bubble condensation

Simulations of an ascending water bubble in condensation were performed and the results were compared to the literature. The figure below shows the water bubble interface at the initial time and after 3ms when condensation has almost completely vanished the vapor phase.

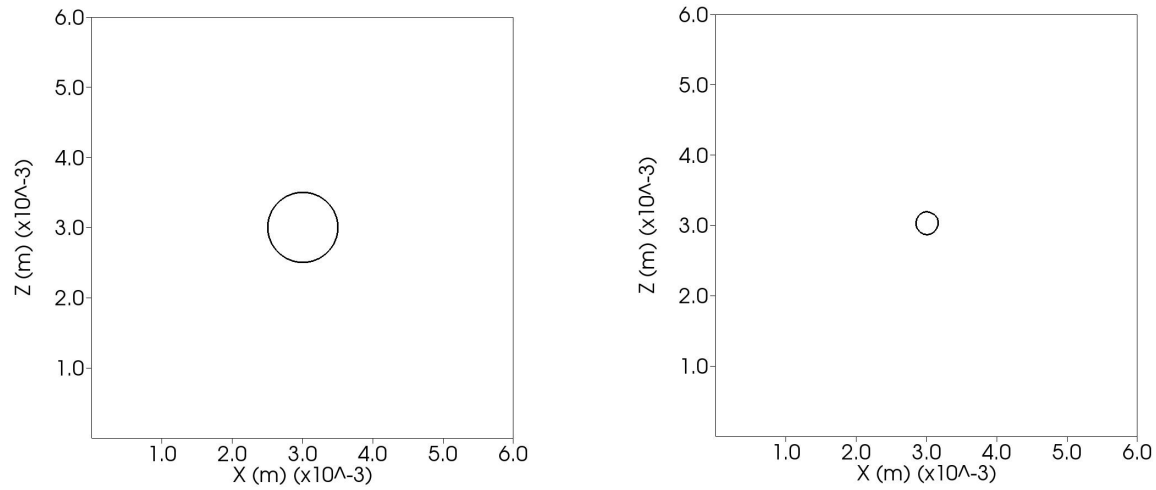

(a) (b)

Figure 1.9: Water vapour bubble in condensation at the initial and final time of the computational simulation.

1.4.10 Simulation of steam jet in condensation subjected to a liquid cross-flow

Simulations of a steam jet condensation with a liquid cross-flow was investigated. The figure below shows the interface contour from the saturated vapour jet in cross-flow with liquid water.

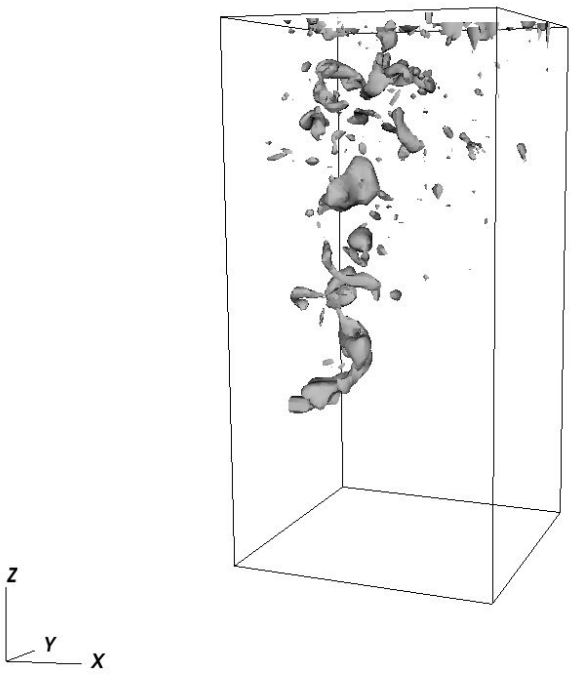

Figure 1.10: Water vapour jet in cross-flow with liquid water.

1.5 Thesis organization

The present work was organized in 7 chapters, namely:

- Chapter 1: it contains the introduction of the work. The objectives and the main original contributions are described. The thesis main results are highlighted and the thesis organization is informed;
- Chapter 2: a background of the thesis topic is presented and the state-of-art of computational modelling of non-isothermal flows subjected to phase change is described in details;

- Chapter 3: the mathematical model used in the simulations is described. First, the mathematical model of non-isothermal flows without phase change is presented; then, the mathematical model of non-isothermal flows subjected to phase change is reported. Finally, a detailed subsection described the equations used in the cases where the specific mass variations were modelled according to the temperature field.

- Chapter 4: the numerical and computational models employed in the present work are described. Details about the numerical discretizations, numerical treatment of interface and fluid variables were presented. The code MFSim is presented and its main characteristics are described.

- Chapter 5: the results are presented and compared to literature previous results. In addition, the main results were summarized and a discussion was subsequentely provided.

- Chapter 6: the conclusions of the present thesis were presented. Each specific objective previously defined in the thesis plan provided one or more conclusions according to the results obtanied.

- Chapter 7: it presents the main suggestions of future works based on the advances achieved in the present thesis.

CHAPTER II

BACKGROUND

In this chapter, the authors present the central aspects related to modelling computationally non-isothermal flows with and without phase change, according to the literature. The main topics related to the thesis investigations are here described using the information found in the literature.

The majority of ordinary fluid dynamic problems usually does not require information about the temperature field (TRYGGVASON; SCARDOVELLI; ZALESKI,), since the variables of interest are usually the velocity or pressure (DUARTE *et al.*, 2018). However, for most of the engineering applications, the temperature is an indispensable variable, affecting directly the flow characteristics such as in phase change problems (TANGUY *et al.*, 2014) or indirectly, modifying the physical properties of fluids due to the temperature variations (MONTIEL-GONZALEZ *et al.*, 2015; DUARTE *et al.*, 2018).

The importance of the temperature field in the computational fluid dynamics (CFD) is usually restricted to problems where the effects of temperature are proeminent or necessary to the flow characteristics since it represents the additional costs to solve the energy equation (TRYGGVASON; SCARDOVELLI; ZALESKI,). To model the phase change phenomenon, the temperature field is obviously necessary to be known in the computational simulations; however, for several other problems, the temperature field hardly call attention to the literature, although it may bring severe consequences to the flow dynamic (DUARTE *et al.*, 2018).

In the next sections, a background about non-isothermal flows is presented. First, compu-

tational aspects of modelling non-isothermal flows without phase change are reported. Then, the state-of-art of modelling phase change computationally is presented and its main characteristics are described.

2.1 Non-isothermal flows without phase change

In this section, some topics related to the computational aspects of modelling non-isothermal flows without phase change are reported. First, the importance of the specific mass variations due to the temperature field will be described. Then, the influence of some dimensionless parameters in non-isothermal flows are presented. Finally, the influence of bubbles in non-isothermal flows are briefly reported.

2.1.1 Specific mass variations due to temperature field

Although the term "density" is more commonly used than "specific mass" in the literature, the authors of the present work consider that "density" is suitable for referring to the property of an object or of a composed substance. On the other hand, "specific mass" refers to the property of a substance. Therefore, in the present thesis, the term "specific mass" will be used to define the amount of mass per unit volume.

Most of the fluid physical properties are temperature-dependent since the variations of temperature may modify the fundamental characteristics of fluids (POLING; PRAUSNITZ; O'CONNELL, 2001). In the computational fluid dynamics (CFD), the importance of these fluids properties variation is restricted to problems where the temperature fields affects directly the flow dyamics such as natural convection problems (MONTIEL-GONZALEZ *et al.*, 2015). For most of the natural convection problems, the traditional Oberbeck-Boussinesq approximation is sufficient to model computationally the flow dynamic correctly. On the other hand, the majority of the engineering applications are related to turbulent flows and usually with the presence of strong temperature gradients (AKHTAR; KLEIS, 2013).

The literature presents some alternative forms to model the effects of specific mass variations without invoking the OB. One form to model the specific mass variations is to solve the continuity, momentum and energy equations considering variable specific mass in all the equa-

tions. The later way requires to solve the flow as compressible, where the continuity equation is solved without the usual simplification seen for incompressible flows. The literature also presents another form to account the effects of specific mass variations without invoking OB or solving the diferential equations considering the flow as compressible. The later form is generally known as non-Oberbeck Boussinesq models (NOB), where the specific mass is considered variable in all the terms from the momentum and energy equations; although the continuity equation preserves the incompressible condition with null velocity-divergence.

The NOB method was fundamentally based on Markatos e Pericleous (1984), who previously studied natural convection in a 2D numerical model. Markatos e Pericleous (1984) employed an extension of OB, considering specific mass as a function of the temperature in all the terms of the momentum and energy equations. More recently, Montiel-Gonzalez *et al.* (2015) presented a numerical investigation of thermal convection problems with a comparison between OB and a new temperature-dependent method for all the fluid properties, and considering null velocity divergence. Their work obtained numerical results with higher accuracy in the approach using variable fluid properties as functions of temperature.

Most of what is known about natural convection is due to the use of OB (GRAY; GIORDINI, 1976) and more than one hundred years after the publication of OB, it is still probably the most employed formulation for natural convection (ZEYTOUNIAN, 2003). Some of the literature, e.g., Montiel-Gonzalez *et al.* (2015) and Markatos e Pericleous (1984), have proposed alternative mathematical formulations to achieve more accurate results about thermal transfer without invoking OB, but still assuming null velocity divergence. A large number of flows subjected to thermal transfer are assumed to be incompressible, since the impact of a variable specific mass in the continuity equation is not relevant. On the other hand, the effects of a temperature-dependent approach for the specific mass in the momentum equation are particularly important for non-isothermal flows, as previously stated by OB (BOUSSINESQ, 1903). Therefore, when the flow is assumed incompressible, the velocity divergence is small enough to be considered null. However, variations of the specific mass in the momentum and energy equations may be pertinent due to the influence of temperature on the properties of the fluid, as found by Montiel-Gonzalez *et al.* (2015).

The importance of modeling variations in the properties of the fluid depending on the

temperature field is recently being more investigated in several non-isothermal problems and this research has been important for bringing new insights into thermal transfer mechanisms. Several studies have investigated the thermodependency of the fluid variables in non-isothermal flows, such as Darbouli *et al.* (2016) and Montiel-Gonzalez *et al.* (2015).

The relevance of the specific mass variations due to the temperature field is particularly critical to a major part of fluid dynamic problems, namely natural convection cases. The variations of specific mass plays an important role on the flow characteristics modifying the velocity and pressure fields. Therefore, the specific mass is modeled here using a temperature-dependent approach and a benchmark is conducted with the traditional Oberbeck–Boussinesq approximation (OB).

In the literature, similar numerical studies on non-Oberbeck–Boussinesq buoyancy induced flows have been reported in the laminar and turbulent regimes; however, no similar investigation has been presented in three dimensions, which is particularly relevant for turbulence.

2.1.2 Influence of relevant dimensionless numbers on non-isothermal flows

There are several dimensionless numbers related to the physics of non-isothermal flows such as the Grashof, Prandtl, Rayleigh, Eckert, Brinkman and Nusselt numbers. These dimensionless numbers generally characterize the relation between the temperature field and the flow dynamics. Next, these dimensionless numbers are briefly described.

The Grashof number represents the ratio of gravitational to viscous force on a fluid and it's defined according to the following equation (WHITE, 1974):

$$Gr = \frac{g\beta(T_s - T_\infty)L^3}{\nu^2} \tag{2.1}$$

where: g is the gravity acceleration field, β is the volumetric expansion coefficient, T_s is the temperature at a given reference surface, T_∞ is the temperature of reference, L is the characteristic length and ν is the kinematic fluid viscosity. The Prandtl number defines the ratio of momentum diffusivity to thermal diffusivity and it's given by the following expression (WHITE, 1974):

$$Pr = \frac{\mu Cp}{k} \tag{2.2}$$

where: Cp is the specific thermal energy, μ is the dynamic viscosity and k is the thermal conductivity. The Rayleigh number consist of the product of Prandtl and Grashof numbers which is expressed below:

$$Ra = PrGr \tag{2.3}$$

The Rayleigh number expresses the ratio between the buoyancy and viscosity forces as well as the ratio between the momentum and thermal difussivities. The Eckert number consist of the ratio between the kinetic energy by the boundary layer enthalpy and is defined by the expression given below:

$$Ec = \frac{u^2}{Cp\delta T} \tag{2.4}$$

where u is the local flow velocity, Cp is the specific thermal energy and δT is the difference between wall and local temperature. The Brinkman number is a dimensionless number associated to the ratio between the thermal energy produced by viscous transformation and thermal energy transported by molecular diffusion. The Brinkman number is given by the following expression:

$$Br = \frac{\mu u^2}{k(T_w - T_0)} \tag{2.5}$$

where T_w is the wall temperature and T_0 is the temperature of reference.

The Nusselt number may be defined according to the following expression (DEEN; KUIPERS, 2013):

$$Nu = \frac{L}{\Delta T}\frac{\partial T}{\partial x}|_{x=0} \tag{2.6}$$

where: T is the temperature and ΔT is the temperature difference between the east and west walls. The Nusselt number (Nu) represents the ratio between the conductive and advective thermal transfer processes; therefore, when $Nu < 1$, there is the predominancy of conduction, and when $Nu > 1$, the advection effects are more proeminent than the conduction (WAN; PATNAIK; WEI, 2001).

According to the literature, the Grashof and the Prandtl numbers directly affect the thermal transfer rate in non-isothermal flows. The work from Chandra e Chhabra (2012) investigated the impact of the variations of these dimensionless numbers on the Nusselt number and the later authors found the increasement of the Nusselt number when Prandtl and Grashof number increased. However. the later work studied only single-phase flows. The influence of the Grashof number on the Nusselt number is already consolidated in the literature (PADILLA; LOURENCO; SILVEIRA-NETO, 2013; WAN; PATNAIK; WEI, 2001) and its increasement necessarily increases the thermal transfer rate. However, the role of the Prandtl number is yet not so studied in the literature.

2.1.3 Influence of bubbles on non-isothermal flows

It has been extensively reported in the literature the increasement of the thermal transfer rate due to the introduction of bubbles in single-phase flows; however, this topic has not yet been completely elucidated.

The thermodynamic effects of the addition of bubbles in single-phase flows are widely described in several experimental and numerical studies in the literature. According to Deen e Kuipers (2013), it is generally agreed in the literature that the introduction of a gas into a liquid enhances the turbulence in the medium and thus increases the thermal transfer rate to immersed surfaces. Deen e Kuipers (2013) additionally defend that higher gas velocities enhances even more the thermal transfer rate. Deckwer (1980) suggested that the presence of bubbles can increase the thermal transfer rate in a gas-liquid bubble column by more than one order of magnitude. Oresta *et al.* (2007) studied the thermal transfer mechanisms in a case of Rayleigh-Benard convection in a liquid with vapor bubbles. The authors from the later work concluded that the presence of bubbles had a profound effect on the flow structure and on the Nusselt number calculated. Deen e Kuipers (2013) found that the passage of a bubble in a vertical chanel increased the local thermal transfer from a hot wall. Tamari e Nishikawa (1976) reported that the presence of bubbles increased the convection due the addition of bouyancy force. Dabiri e Tryggvason (2015) studied turbulent bubbly flow and reported that the presence of bubbles increased the mixing and reduced the temperature difference between the hot wall and the bulk of the flow. The later work presents the Nusselt number increasement of 60% when bubbles were included in the domain

(considering 3% of volume fraction).

According to Dabiri e Tryggvason (2015), the presence of moving bubbles generally increases the local thermal transfer. Bukhari e Siddiqui (2007) studied natural convection for two-phase flow and concluded that thermodynamic patterns, such as the thermal exchange at the interface, may be directly affected by some hydraulic patterns such as the velocity field. The authors from the later work concluded that the turbulent structures on the air and water phases played an important role enhancing the thermal and mass transfer rates. Chandra e Chhabra (2012) presented a quantitative analysis of the influence of the Prandtl and the Grashof numbers in single-phase flows, reporting the Prandtl number importance in regulating the thermal transfer rate on immersed surfaces in single-phase flows.

Although the literature has obtained, majority, higher thermal transfer coefficients in two-phase flows compared to single-phase flows; there is no quantitative analysis or conclusions elucidating the causes of the numerical or experimental results obtained. In addition, some works have presented opposite results, such as Qiu, Wang e Jiang (2014) which obtanined the decreasement of the thermal transfer rate by the inclusion of bubbles in the flow.

It's imperative to examine the thermal transfer characteristics using dimensionless parameters in order to establish general conclusions and to improve the understanding of the underlying mechanisms involving the thermal transfer mechanisms. Since information about the thermal transfer rate in single-phase and two-phase flows are crucial to several industrial processes as well as in a variety of equipments employed in engineering applications, computational investigations may guide and improve the efficiency of the thermal transfer processes. In addition, new studies on these topics may report new insights into the thermal transfer mechanisms, openning new research opportunities related to non-isothermal two-phase flows.

2.2 Non-isothermal flows with phase change

In this section, a general overview of modelling phase change computationally will be presented. Phase change is a topic yet few consolidated in the literature of CFD since several issues remain few understood, such as micro-layer phase change (CHEN; UTAKA, 2015), nucleation points (AKHTAR; KLEIS, 2013) and phase change in multicomponent fluids (STROTOS *et al.*,

2011).

The main topics related to the thesis investigations are reported in this section and the state-of-art of modelling phase change computationally are described according to the literature.

2.2.1 Computational simulations of phase change

Phase change is a relevant issue in industrial applications (HAELSSIG; THIBAULT; ETEMAD, 2010) since it plays a critical role in a large number of processes (WELCH; WILSON, 2000; JURIC; TRYGGVASON, 1998). Boiling, for example, is a highly efficient way to transfer thermal energy, notably in industrial thermal exchangers (NIKOLAYEV *et al.*, 2016). Moreover, chemical separation techniques, such as distillation, are characterized by simultaneous mass and energy transfer (HAELSSIG; THIBAULT; ETEMAD, 2010). Droplet evaporation is another indubitable important phenomenon presenting great importance for certain applications (STROTOS *et al.*, 2011), particularly burning liquid-fuels. The earlies phase change numerical works in the literature presented important aspects of mathematical and numerical modelling which can be seen in (JURIC; TRYGGVASON, 1998) and (WELCH; WILSON, 2000). Later, several advances in mathematical and numerical modelling have been achieved and reported in the literature with even complex simulations for industrial applications (TANGUY *et al.*, 2014).

Numerical simulations of phase change are relevant to collect information about flow characteristics since experiments dealing with phase change are usually difficult to be correctly conducted (PAN; WEIBEL; GARIMELLA, 2016) due to the small spatial scales (WELCH; WILSON, 2000) and the rapidity of phase change process (JURIC; TRYGGVASON, 1998). Phase change simulations present several numerical obstacles (TRYGGVASON; LU, 2015). One of the most challenging aspects is notably the physical properties discontinuities occuring at the interface between two fluids (TSUI *et al.*, 2014). In addition, the jump conditions across the interface of fluid properties, such as pressure, represent an important aspect to be considered in phase change simulations (TANGUY *et al.*, 2014).

In order to impose jump conditions at the interface, a sharp or a diffuse interface treatment can be used for each fluid variable. A sharp interface treatments usually provide an accurate definition of a fluid variable across the interface, improving the resolution of the jump condition (TANGUY; MENARD; BERLEMONT, 2007). On the other hand, the results from a diffuse

interface treatment generally presents a poor representation of the jump conditions at the interface since the fluid properties are smoothed across the boundary between the two fluids (TANGUY *et al.*, 2014). The development of spurious currents at the interface is a typical consequence in the velocity field due to the employment of a diffuse interface treatment for pressure.

Fictitious velocities emerges due to an erroneous estimation of the surface tension force (HARVIE; DAVIDSON; RUDMAN, 2006) and pressure gradient according to the numerical schemes employed (AKHTAR; KLEIS, 2013). In addition, the spurious currents tend to be intensified in the phase change problems (TANGUY *et al.*, 2014), then they should be particularly controlled in these numerical simulations. The spurious currents generally appear close to the interface when computations of a static bubble or droplet are performed with a diffuse interface treatment for pressure due to the surface tension force calculation (FRANCOIS *et al.*, 2006). According to Tanguy *et al.* (2014), the spurious currents intensity increases when phase change occurs due to the jump condition on the velocity field. In addition, the presence of spurious currents may be partly responsible for an inaccurate interface evolution in time since this boundary's advection is performed using the local velocity field.

Tanguy *et al.* (2014) have presented inaccurate results for a diffuse interface treatment in phase change simulations. Other works in the literature using a diffuse interface treatment, as Samkhaniani e Ansari (2016) and Lee, R. e Aute (2017) found numerical results with a low deviation with the literature. More studies are necessary to understand the consequences of using a diffuse interface treatment instead of a sharp strategy for one or more fluid variables in phase change simulations. In addition, it's appropriate to quantify these fictitious velocity field in the phase change simulations in order to evaluate its consequences and to visualize the behavior of the interface motion in time to confirm the acuracy of the numerical model employed.

As previously seen, modelling phase change computationally may be difficult due to the small scales of time and space. Using dimensionless numbers it is possible to model even complex problems by modifying some physical properties of the problems but preserving the main dimensionless number related to the phenomenon represented. One important dimensionless number in the phase change topic is the Jakob number. The Jakob number is defined according to the

following expression:

$$Ja = \frac{\rho_l Cp_l (T_\infty - T_{sat})}{\rho_v L} \tag{2.7}$$

where: T_∞ is the temperature of reference far from the dispersed phase, T_{sat} is the saturation temperature and L is the latent energy.

2.2.2 Jump conditions in phase change simulations

Literature presents two numerical strategies to impose jump conditions of fluid variables across the interface, namely the Whole Domain formulation and the Jump Condition formulation (TANGUY *et al.*, 2014). The Whole Domain methodology uses a Delta Functions method (Delta), in which the jump conditions are smoothed around the interface, smearing out discontinuities terms. On the other hand, the Jump Condition formulation uses a Ghost Fluid Method (GFM) in which the interface is treated imposing the jump conditions by ghost cells (TANGUY *et al.*, 2014; TANGUY; MENARD; BERLEMONT, 2007).

The Delta method computes the surface tension force using a continuum surface force (CSF) model (BRACKBILL; KOTHE; ZEMACH, 1992) which usually generates spurious currents due to a numerical imbalance between the pressure gradient and the related surface tension force (FRANCOIS *et al.*, 2006). Even though the presence of spurious currents has been extensively observed by researchers since CSF conception, to date there has been little quantitative analysis of their importance (HARVIE; DAVIDSON; RUDMAN, 2006), specially when applied to problems involving phase change. Numerous approaches have been proposed to supress spurious currents; although, several methods have difficulties to not induce unphysical flows due to the numerical error in estimating the interfacial surface tension (PAN; WEIBEL; GARIMELLA, 2016). Conversely, the GFM approach computes the surface tension force without a smooth transition due to a sharp jump condition for pressure at the interface (FRANCOIS *et al.*, 2006).

2.2.3 Particular forces in phase change problems

Two forces were evaluated in the present work in order to better understand the importance and consequences of modelling them in phase change problems, namely: the recoil force and the

additional force due to the use of the non-divergent form of momentum equation. For the first time in the literature of phase change, the additional force due to the use of the non-divergent form of momentum equation is presented and quantified. The need of this additional term in phase change problems is reserved to the use of the non-divergent form of momentum equation and the occurence of mass transfer at the interface. Since the interface cells do not present null-divergence velocity in phase change problems, the non-divergent form of momentum equation naturally receives an additional term from the continuity equation. The details of this extra force term are described in the mathematical model section; later, the computational results section presents a quantitative analysis of the additional force term in phase change simulations.

During phase change, a recoil force appears at the interface between the two fluids due to volume change (RAGHUPATHI; KANDLIKAR, 2016). The intensity of recoil force depends on the mass density flux occuring at the interface. The recoil force may be defined according to the following expression (NIKOLAYEV *et al.*, 2016):

$$\vec{f}_{recoil} = \dot{m}''^2 \left(\frac{1}{\rho_v} - \frac{1}{\rho_l} \right) \vec{n} \tag{2.8}$$

where: $\dot{m}''$ is the mass density flux (this term is described in the mathematical model section), ρ is the specific mass and $\vec{n}$ is the normal vector.

The study of the recoil force in CFD investigations begun in the last 30 years (RAGHUPATHI; KANDLIKAR, 2016); however, few numerical works dealing with phase change have quantified or evaluated the role and the importance of this force in momentum equation. The term which models the influence of the recoil force is included in several works in the literature as Lee, R. e Aute (2017), Tanguy *et al.* (2014), although is not even cited in other works such as Welch e Wilson (2000), Akhtar e Kleis (2013). Until the present moment, few works have studied the influence of the recoil force in phase change problems, such as Raghupathi e Kandlikar (2016). The relevance of this term have been ignored in several works of the phase change literature and at the same time it has been included in numerous numerical works without an evaluation of its importance or influence. The knowledge of the relevance of the recoil force in phase change problems may be important to understand the underlying mechanisms behind phase change fundamentals. Therefore, in the present work, numerical simulations were performed to

compute the magnitude of this force and its importance to phase change problems.

2.2.4 Adaptive mesh refinement (AMR) in phase change problems

It's known that an accurate numerical solution of partial differential equations rely on the discretization on a computational grid with sufficiently high resolution. On the other hand, the simulations using uniform grids overly increase the computational costs due to a large domain region unnecessarily refined. A uniform and fine grid is generally associated with a high computational cost which may limit the applicability of solving several complex problems of interest. Conversely, the AMR methodology is a computational tool allowing the definition of a criteria to guide a spatially non-uniform mesh refinement according to an indicator function, such as vorticity, temperature gradient or interface presence.

AMR may provide a strategy to solve complex problems using lower computational resources compared to uniform grids (AKHTAR; KLEIS, 2013) and it reduces the computational power requirement without affecting the precision from the numerical results (NINGEGOWDA; PREMACHANDRAN, 2014). The interest in using AMR in multiphase flows is particularly large since the interface region frequently requires fine grids due to the calculation of high gradients and the rest of the domain usually do not require fine grids (NIKOLOPOULOS; THEODORAKAKOS; BERGELES, 2007).

Recently, phase change literature present several works which employ AMR strategy to model some large scale or complex problems. In the present work the refinement criteria was related to the interface location which the majority of works in the phase change literature does, such as Akhtar e Kleis (2013). In order to compute a quantitative evaluation of the improvement of time and computational power saved with AMR compared to uniform grids, an expression of AMR efficiency is used to quantify the enhancement of AMR strategy from the literature.

2.2.5 Direct contact condensation

Modelling complex fluid dynamic problems to predict its main characteristics is important to the improvement of a variety of industrial processes and engineering applications. Since the majority of these problems are related to non-isothermal flows as well as phase change phenomenon, there is the need to include models to consider the influence of these particular effects. In the

field of phase change phenomenon, the Computational Fluid Dynamic (CFD) has become a progressively important tool to solve complex flows for a variety of engineering applications (TRYGGVASON; SCARDOVELLI; ZALESKI,). An important problem related to phase change is the cross-flow of a liquid with a condensing vapour jet which is present in several industrial applications (ZOHOU *et al.*, 2017; CLERX *et al.*, 2011; PATEL; TANSKANEN; R.KYRKI-RAJAMÃ¤KI, 2014). The later problem is part of a well-known field in the phase change literature which is denominated direct contact condensation (ZARE; JAMALKHOO; PASSANDIDEH-FARD, 2018). Direct contact condensation (DCC) is the process where saturated vapour contacts and condenses directly through a subcooled liquid interface (PATEL; TANSKANEN; R.KYRKI-RAJAMÃ¤KI, 2014). The DCC phenomenon is deeply complex and; modelling it in a cross-flow becomes even more challenging, since the fundamental processes are still few understood (ZARE; JAMALKHOO; PASSANDIDEH-FARD, 2018).

Jets in cross-flow are widely encountered in a large variety of industrial applications, such as pipe tee mixers. A recurrent case of cross-flow is the application of condensing jets of a saturated vapor injected into a flowing liquid (CLERX; GELD; KUERTEN, 2013; XU *et al.*, 2016). Direct steam injection is an efficient procedure to heat fluid in a fast way (WISSEN; SCHREEL; GELD, 2005), specially when a high mixing rate is needed (CLERX; GELD; KUERTEN, 2013). The technique of systems with direct heating via steam injection is widely used by the dairy industry for the sterilization of milk products (CLERX *et al.*, 2011).

Experiments modelling condensing jets are particularly difficult to be performed since a number of expensive and complex equipments are necessary to control the thermodynamic conditions as well as to collect the data to future analysis (TRYGGVASON; SCARDOVELLI; ZALESKI,). Most of the information found in the literature related to condensing jets studied the jet centerline trajectory using the temperature or the velocity fields (CLERX; GELD; KUERTEN, 2013; CLERX *et al.*, 2011). Other works, were focused on the axial velocity and pressure distribution as well as the jet penetration length (ZOHOU *et al.*, 2017). There is few information about the condensing jet characteristics and specially when subjected to cross-flow (ZARE; JAMALKHOO; PASSANDIDEH-FARD, 2018); in addition, most of the previous numerical works presents limitations, such as performing simulations in 2D (ZOHOU *et al.*, 2017; TANSKANEN *et al.*, 2014).

The general physical behavior of the case of condensing jet in cross-flow is well known in

the literature which usually reports the formation of three different regions when steam is injected in the domain. The first region is composed of pure steam right next to the nozzle exit which is commonly called steam plume due to its shape. The second region is generally named interface since it consists of a small region next to the plume where the condensation process is more intense due to the larger temperature gradients (CLERX; GELD; KUERTEN, 2013). Finally, the third region represents hot liquid with small vapour bubbles, comprising the most part of the domain (ZARE; JAMALKHOO; PASSANDIDEH-FARD, 2018).

The flow characteristics of the condensing jet in cross-flow modifies according to the steam mass flux imposed (CLERX; GELD; KUERTEN, 2013). At high steam mass fluxes, the steam forms an oscillatory or a stable vapor which ends at a certain distance from the injector. At low steam mass flux, the condensing steam forms a vapor pocket which continuosly grows and collapses at the steam injection hole. At very low mass flux, the steam-liquid interface is advected periodically in and out of the injection hole, characterizing the chugging regime (CLERX *et al.*, 2011).

Recently, the literature has presenting relevant phase change studies with accurate results using computational models, namely the movement of bubbles (TANGUY *et al.*, 2014) or even jets (ZOHOU *et al.*, 2017) and sprays (KITANO *et al.*, 2014). The numerical and computational models found in the phase change literature allows the performance of simulations on even large domains, however relevant information at the microscale is inevitably lost.

CHAPTER III

MATHEMATICAL MODEL

In this chapter, the mathematical model used for non-isothermal flows without and with phase change is described. First, the mathematical model used for the cases without phase change is reported. Then, the mathematical formulation used for modelling non-isothermal flows with phase change is presented.

3.1 Non-isothermal flows without phase change

In this section, the mathematical model used for non-isothermal flows without phase change is described. Two different approaches were employed to model non-isothermal flows without phase change, namely the OB and NOB models.

3.1.1 Formulation using the Oberbeck-Boussinesq approximation (OB)

In OB, the continuity, momentum, and energy equations are given by the following expressions (GRAY; GIORDINI, 1976):

$$\vec{\nabla}.\vec{v} = 0, \tag{3.1}$$

$$\rho_0 \frac{D\vec{v}}{Dt} = -\vec{\nabla}p + (\rho - \rho_0)\vec{g} + \vec{\nabla}.\left[\mu\left(\vec{\nabla}\vec{v} + (\vec{\nabla}\vec{v})^T\right)\right], \tag{3.2}$$

$$\frac{DT}{Dt} = \alpha\nabla^2 T, \tag{3.3}$$

where v represents the velocity, ρ_0 represents the specific mass of reference, p is the pressure, ρ represents the specific mass, and μ is the dynamic viscosity, T represents the temperature and α is the thermal diffusivity.

The following thermodynamic relation was employed in the momentum equation to compute variable specific mass effects as a function of the temperature (WANG; ZHANG; GUO, 2017):

$$(\rho - \rho_0)\vec{g} = -\rho_0\beta(T - T_0)\vec{g}, \tag{3.4}$$

where T_0 represents the temperature of reference and β is the volumetric expansion coefficient. The total variation of ρ is given by $d\rho = \frac{\partial\rho}{\partial T}|_{p=cte}dT + \frac{\partial\rho}{\delta p}|_{T=cte}dp = \frac{\partial\rho}{\partial T}|_{p=cte}dT$. Equation 4 can be found by integrating this last expression and taking $\beta = \frac{1}{T}$ and M, R and p constant.

3.1.2 Formulation using the new temperature-dependent specific mass approach (NOB)

The non-Oberbeck–Boussinesq (NOB) comprises a relaxation of OB restrictions by allowing a variable specific mass in all the terms of the momentum and energy equations (MONTIEL-GONZALEZ *et al.*, 2015). In addition, the limitation of the Oberbeck–Boussinesq approximation (OB) to single-phase flows is overcome. However, the mathematical formulation introduced in the present thesis still remains an approximation since the continuity equation is solved as null velocity-divergent (DUARTE *et al.*, 2018).

The specific mass is calculated based on the temperature field and a divergence free-velocity is imposed on the NOB due to the small effects of variations of the specific mass in the continuity equation, as previously demonstrated by the OB. The purpose of the NOB is to overcome the

OB's restriction to single-phase flows, as well as to model the effects of specific mass variations more accurately, especially in problems with prominent thermal transfer effects, as occur in the turbulent regime. Since the effects of a variable specific mass in the momentum and energy equations were taken into account by the NOB, it was expected that the thermal transfer results of the NOB would be improved compared with those of the OB (DUARTE *et al.*, 2018).

In NOB, the continuity, momentum, and energy equations are given by the following expressions, as seen in Markatos e Pericleous (1984):

$$\vec{\nabla}.\vec{v} = 0, \tag{3.5}$$

$$\rho\frac{D\vec{v}}{Dt} = -\vec{\nabla}p + \vec{\nabla}.\left[\mu\left(\vec{\nabla}\vec{v} + (\vec{\nabla}\vec{v})^T\right)\right] + \rho\vec{g}, \tag{3.6}$$

$$\rho Cp\frac{DT}{Dt} = \nabla.(k\nabla T). \tag{3.7}$$

The specific mass is calculated using the ideal gas law, given by the following equation (POLING; PRAUSNITZ; O'CONNELL, 2001):

$$\rho = \frac{pM}{RT}, \tag{3.8}$$

where M is the molar mass and R is the gas constant.

A constant atmospheric pressure was assumed since the experimental data available in the literature used for validation has assumed an imposed constant pressure in order to conduct the experiments. Details are described in Leong, Hollands e Brunger (1999).

3.2 Non-isothermal flows with phase change

In this section, the mathematical formulation used to model non-isothermal flows with phase change is presented. First, the general mathematical formulation is described; then, an

issue related to the use of the non-divergent form of the momentum equation is described.

3.2.1 Description of the general mathematical formulation

The mathematical formulation was employed in the non-divergent form as recommended by Deen e Kuipers (2013). Putting ρCp inside the substantial derivative would lead to a non-physical change of the enthalpy if two materials next to each other present the same temperature but different ρCp, as demonstrated by Deen e Kuipers (2013). Therefore, the non-divergent form was used in the numerical simulations in order to avoid non-physical issues.

In order to compute the amount of phase change occuring at the interface, the present model uses the calculation of the mass density flux ($\dot{m}''$). The mass density flux is included in the mathematical formulation using source terms in the continuity and energy equations and it is defined according to the following expression (TANGUY *et al.*, 2014):

$$\dot{m}'' = \frac{k_l \vec{\nabla} T_l . \vec{n} - k_v \vec{\nabla} T_v . \vec{n}}{L} \tag{3.9}$$

where: k is the thermal conductity, L is the latent energy, T is the temperature and $\vec{n}$ is the normal vector.

Phase change problems present null velocity-divergent in the bulk of each phase and at the interface there is a source term for mass balance (JURIC; TRYGGVASON, 1998). The continuity equation is expressed using a Dirac delta function in the right-hand-side to account the source term only over the interface, according to the following equation (TANGUY *et al.*, 2014):

$$\vec{\nabla} . \vec{v} = \int_\Gamma \left(\frac{1}{\rho_v} - \frac{1}{\rho_l} \right) \dot{m}'' \delta(\vec{x_k}) d\Gamma \tag{3.10}$$

where: $\vec{v}$ is the velocity, ρ is the specific mass, δ represents the Dirac Delta function, $\vec{x_k}$ is the position of the interface Γ. Considering low Mach number flows with low temperature variations, it can be expected the divergence-free condition (except at the interface when phase changes occurs).

The momentum balance equation is given by (JURIC; TRYGGVASON, 1998):

$$\rho\left(\frac{\partial\vec{v}}{\partial t}+\vec{\nabla}.(\vec{v}\vec{v})\right)=-\vec{\nabla}p+\vec{\nabla}.\left[\mu\left(\vec{\nabla}\vec{v}+(\vec{\nabla}\vec{v})^{T}\right)\right]+\rho\vec{g}+\vec{f_{st}}+\vec{f_{recoil}} \tag{3.11}$$

where: p is the pressure, μ is the dynamic viscosity, $\vec{g}$ is the gravity acceleration, $\vec{f_{st}}$ is the source term to account the surface tension effects and $\vec{f_{recoil}}$ is the source term which computes the recoil force effects at the interface.

The effects of surface tension are included in the formulation using the model of Brackbill, Kothe e Zemach (1992). This model specifies the surface tension force per unit volume as:

$$\vec{f_{st}}=\frac{\rho\sigma\kappa\vec{\nabla}\alpha}{\frac{1}{2}(\rho_l-\rho_v)} \tag{3.12}$$

where σ is the surface tension coefficient, κ is the local curvature and α is the volume fraction of the dispersed phase.

Since this study deals with isobaric phenomena which only imply weak pressure gradients due to dynamical effects, the energy equation was formulated using the internal energy as primitive variable, as recommended by Tanguy *et al.* (2014). The energy equation also presents a source term using a Dirac delta function to model the energy transfered at the interface due to phase change (TANGUY *et al.*, 2014):

$$\rho Cp\frac{DT}{Dt}=\nabla.(k\nabla T)-\int_{\Gamma}\dot{m}''L\delta(\vec{x_k})d\Gamma \tag{3.13}$$

where: Cp is the specific thermal energy. The additional term in the energy equation corresponds to the amount of energy employed in phase change whenever a corresponding mass source term was also added. The source term in the energy equation is important to assure the correct calculations of the thermal fluxes at the interface (WELCH; WILSON, 2000) which is used to compute the mass density flux.

3.2.2 Additional term in the non-divergent form of momentum equation

The mass balance at the bulk of each phase is given by the following expression (LEE; R.; AUTE, 2017):

$$\frac{\partial\left(\alpha\rho\right)}{\partial t}+\vec{\nabla}.\left(\alpha\rho\vec{v}\right)=0, \tag{3.14}$$

where α presents the volume fraction from the continuos phase. Since the flow is incompressible, the mass balance at each phase is given by the following equation (LEE; R.; AUTE, 2017):

$$\vec{\nabla}.\vec{v}=0. \tag{3.15}$$

On the other hand, considering a fluid particle placed at the interface, an additional source term emerges due to phase change in order to consider the variations of specific mass in these cells during the volume expansion or contraction. Considering incompressible flow, the mass balance includes a source term at the interface cells given by the following expression:

$$\vec{\nabla}.\vec{v}=\int_{\Gamma}\left(\frac{1}{\rho_{v}}-\frac{1}{\rho_{l}}\right)\dot{m}''\delta(\vec{x_{k}})\,d\Gamma. \tag{3.16}$$

An interesting remark about the momentum equation in phase change problems which has not yet been described in the literature is the appearence of an additional force term in the non-divergent form compared to the divergent form. An additional force appears due to the non-zero velocity divergence in the continuity equation at the interface cells. Until the present moment, the literature has not pointed out the difference between the divergent or non-divergent forms of the momentum equation. Next, this difference will be described and quantified later in the numerical results section.

Writing the momentum equation in the not divergent form from the divergent form, the expression of the continuity equation appears naturally due to the product rule for the derivatives, as shown in the following expression:

$$\frac{\partial\left(\rho\vec{v}\right)}{\partial t}+\vec{\nabla}.\left(\rho\vec{v}\right)\vec{v}=\rho\left[\frac{\partial\vec{v}}{\partial t}+\left(\vec{v}.\vec{\nabla}\right)\vec{v}\right]+\underbrace{\vec{v}\left[\frac{\partial\rho}{\partial t}+\vec{\nabla}.\left(\rho\vec{v}\right)\right]}_{extra-term}=\rho\vec{g}+\vec{\nabla}.\bar{\sigma}+\vec{f_{\sigma}}. \tag{3.17}$$

Since the continuity equation is non-zero over the interface cells, an additional term appears at the interface cells due to phase change. This additional force is modelled according to the mass balance source term which is defined in the following expression only at the interface:

$$\rho\left[\frac{\partial\vec{v}}{\partial t}+\left(\vec{v}.\vec{\nabla}\right)\vec{v}\right]+\underbrace{\vec{v}\left[\rho\int_{\Gamma}\left(\frac{1}{\rho_v}-\frac{1}{\rho_l}\right)\dot{m}''\delta(\vec{x_k})\,d\Gamma\right]}_{extra-term}=\rho\vec{g}+\vec{\nabla}.\bar{\sigma}+\vec{f_\sigma}. \tag{3.18}$$

Therefore, the non-divergent form naturally imposes an additional force due to phase change which is not explicitly present in the divergent form of momentum equation. The simulations in the present paper were perfomed in the non-divergent form and tests were conducted comparing the effects of this additional force in the non-divergent form of momentum equation.

3.2.3 Turbulence model

Turbulence modeling was performed using Large Eddy Simulation (LES) and the turbulence closure was done via the dynamic model of Germano *et al.* (1991) and Lilly (1992). The dynamic turbulence model used was first proposed by Germano *et al.* (1991) and then modified by Lilly (1992).

3.2.4 Interface location and transport

The Volume of Fluid (VOF) method (HIRT; NICHOLS, 1981) was employed to define the location and transport of the interface in the two-phase flows simulations. The VOF method employed in the MFSim code uses the PLIC algorithm (WACHEM; SCHOUTEN, 2002).

The VOF model employs a color function $\varphi(\vec{x},t)$ to indicate the fractional amount of fluid present at a certain position $\vec{x}$ and time t. The color function φ was calculated using the following equation (WACHEM; SCHOUTEN, 2002):

$$\frac{\partial\varphi}{\partial t}+[\vec{v}_{normal}.\vec{\nabla}\varphi]=0. \tag{3.19}$$

The surface tension effects are included in the formulation using Brackbill, Kothe e Zemach

(1992) model. This model specifies surface tension force per unit of volume as:

$$\overrightarrow{f}_{st}(\vec{x},t) = \frac{\rho\sigma\kappa\nabla\phi}{\frac{1}{2}(\rho_{liq}+\rho_{vap})}, \tag{3.20}$$

CHAPTER IV

NUMERICAL AND COMPUTATIONAL MODEL

4.1 Numerical model

The partial differential equations were solved with a standard finite volume method on a staggered rectangular three-dimensional grid. Velocity–pressure coupling was accomplished using a two-step projection method (CHORIN, 1968) with an explicit treatment for advection terms and an implicit treatment for pressure and diffusion terms. The Barton scheme (CENTRELLA; WILSON, 1984) was used for the spatial discretization of the advective terms.

4.1.1 Phase change model

The phase change model employs an approach similar to Tanguy *et al.* (2014) in order to account for an adequate mass, momentum, and energy transport across the interface. The phase change amount is predicted using the thermal transfer information at the interface and considering the energy source term as the latent energy relevant to the phase change in the interface cells when solving the energy equation (KIM; JEON; PARK, 2017).

In order to compute the temperature gradients at the interface to estimate the mass density flux, the interface is assumed to be at saturation temperature and the volume of fluid (VOF) method is used to construct the proper thermal flux, as previously described by Welch e Wilson (2000). The interface temperature was assumed to be constant in time, which is a

common simplification appropriate for most cases with low effects of thermal resistance and pressure jump, as previously investigated by Juric e Tryggvason (1998). Much of the phase change literature has employed this simplification, which is adequate for modeling classical and even complex problems, cf. Tanguy *et al.* (2014) and Pan, Weibel e Garimella (2016). Therefore, the interface temperature variations in time have been ignored.

If no phase change occurs, the interface velocity is equal to the fluid velocity at the interface. Otherwise, the interface velocity should be computed with the fluid motion and using a phase change component (TANGUY *et al.*, 2014; LEE; R.; AUTE, 2017), as shown in the following expression:

$$\vec{v}_{normal} = \vec{v}_{fluid-motion} + \vec{v}_{phase-change}. \tag{4.1}$$

The velocity component due to a phase change is defined according to the mass density flux previously calculated (LEE; R.; AUTE, 2017).

$$\vec{v}_{phase-change} = \dot{m}'' \left(\frac{1}{\rho_v} - \frac{1}{\rho_l} \right) \vec{n} \tag{4.2}$$

The imposition of a constant mass density flux allows an exact solution for the interface velocity when the fluid motion does not affect the interface position. Therefore, expression 4.3 is useful for the purpose of validating static problems, as previously described by Tanguy *et al.* (2014) and Lee, R. e Aute (2017).

4.1.2 Interface treatment for pressure

The whole domain formulation treats the interface as diffuse, using the Delta function method (Delta). The earliest work on phase change used the Delta method, described in Welch e Wilson (2000) and Juric e Tryggvason (1998). In this approach, the jump conditions at the interface are expressed by introducing singular source terms in the equations.

In the Delta method, an additional source term is placed for the temporal discretization of

the momentum equation according to the following algorithm (TANGUY *et al.*, 2014):

$$\vec{v}^{*} = \vec{v}^{n} - \Delta t \left[\vec{v}^{n}.\vec{\nabla}\vec{v}^{n} - \frac{\vec{\nabla}.(2\mu S^{n})}{\rho^{n+1}} + \frac{\sigma\kappa\vec{n}}{\rho^{n+1}} - \frac{\vec{g}}{\rho^{n+1}} - \frac{\vec{f}_{recoil}}{\rho^{n+1}} \right], \tag{4.3}$$

$$\vec{\nabla}.\left(\frac{\vec{\nabla}p^{n+1}}{\rho^{n+1}} \right) = \frac{\vec{\nabla}.\vec{v}^{*}}{\Delta t} - \frac{\int_{\Gamma} \left(\frac{1}{\rho_v} - \frac{1}{\rho_l} \right) \dot{m}'' \delta(\vec{x_k}) d\Gamma}{\Delta t}, \tag{4.4}$$

$$\vec{v}^{n+1} = \vec{v}^{*} - \Delta t \frac{\vec{\nabla}p^{n+1}}{\rho^{n+1}}, \tag{4.5}$$

where S is the deformation tensor.

On the other hand, the Jump Condition formulation treats the interface as sharp by using the Ghost Fluid Method (GFM), described in Liu, Fedkiw e Kang (2000), who developed a Ghost Fluid Method (GFM) to capture sharp interface boundary conditions in multiphase flows. They proposed a boundary condition capturing approach for the variable coefficient Poisson equation on domains with an embedded interface. In this approach, the equations are written in each phase separately and additional jump conditions have to be imposed at the interface to respect mass conservation. The GFM treats the Poisson equation with both variable coefficients and a discontinuous solution can be obtained, according to Liu, Fedkiw e Kang (2000); alternatively, the Delta method uses a projection method to solve the momentum and Poisson equations with a source term.

Finally, in the GFM method, the pressure must respect the following jump condition (TANGUY *et al.*, 2014):

$$[p]_{\Gamma} = \sigma\kappa - \left(\frac{1}{\rho_v} - \frac{1}{\rho_l} \right) \dot{m}^{2''}, \tag{4.6}$$

where the second term represents the recoil pressure occuring with a phase change (TANGUY *et al.*, 2014). This term represents the pressure jump condition due to a recoil force presence at the interface. A vapor recoil force appears due to the fluid's expansion while transforming liquid to

vapor (NIKOLAYEV *et al.*, 2016).

4.2 Computational model

The transient equations were solved according to the finite volume method using the MFSim program, which has been developed over the last ten years in cooperation with a large research group and with the scientific support of Petrobras, a semi-public Brazilian multinational corporation in the petroleum industry, headquartered in Rio de Janeiro, Brazil.

The code MFSim provides a powerful computational plataform allowing any user to solve even complex engineering problems. The code presents the energy and momentum equations in the divergent and non-divergent form. In the last year, a module for solving compressible flows has been added to MFSim code, allowing the user to perform simulations with the complete continuity equation. The MFSim code allows the user to include any immersed boundary inside the computational domain using the method of Peskin (PESKIN, 1982).

The general algorithm of MFSim code comprises the following steps:

1. Fluid physical properties definition in the computational domain;
2. Interface advection using VOF according to the PLIC algorithm;
3. Definition of the new position of the interface;
4. Calculation of the estimated velocity field according to the fractional step method previously described;
5. Calculation of the pressure correction field;
6. Correction of the velocity field using the pressure correction;
7. Solution the energy equation.

The code MFSim is written mainly using the language Fortran 90 and some particular modules are writeen in C language. In the last year, a graphic interface was created to the MFSim code in order to allow users without any know-how perform computational simulations. The code is continuosly in progress, since it is the product of multiple masters and thesis works. At this

moment, there are about 20 undergraduate and graduate students working on the development of the code. Related to the topic of the present thesis, a module of phase change using a lagrangian approach is also being developed by another student.

The present thesis has contributed to the creation of the energy equation module as well as the phase change module using an eulerian approach. All simulations were performed in a parallel ambient in the fluid mechanics laboratory cluster at the Federal University of Uberlândia, Brazil. The code uses single and multi-block structured meshes and a variable time step. The magnitude of the allowable time step for stable calculations is determined from the convective and viscous terms. The constraint is defined according to the CFL (Courant-Friedrichs-Lewis condition) and the mesh size (AKHTAR; KLEIS, 2013).

The tolerance of the numerical model in providing a solution to the continuity, momentum, and energy equations was 10^{-6}. The code MFSim uses a composite grid, which is block-structured and is defined as an hierarchical sequence of nested, progressively finer grid levels. Each level is formed by a set of non-overlapping parallelepipedal grid blocks aligned with the cartesian coordinate axes and the refinement ratio between two successive levels is two. If the user choose to use dynamic mesh, the mesh is replaced dynamically to ensure that the region of interest represented by the mesh refinement criteria is covered with the finest level at all times. The figure 4.1 illustrates a simulation of a boiling liquid jet impact on an immersed conical surface.

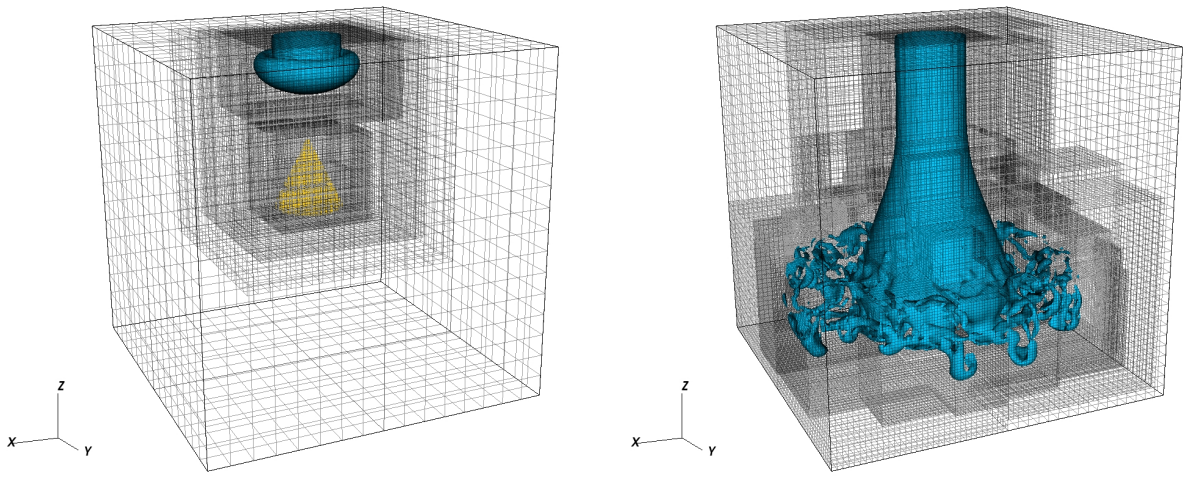

(a) (b)

Figure 4.1: Boiling liquid jet with an immersed conical surface at time t=0.17s (a) and t=1.37s (b).

The phase change algorithm is written separately in a module of the MFSim code; however, the phase change model has connections to the algorithm of the thermal energy equation, the Poisson equation and VOF algorithm. The general algorithm from the phase change module consists of the following steps:

1. Calculation of the mass density flux
2. Calculation of the additional velocity components due to phase change
3. Incorporation of the additional velocity field due to phase change in the VOF advection
4. Incorporation of the mass density flux in the source terms in the Poisson equation
5. Incorporation of the mass density flux in the energy equation

The figure 4.2 illustrates the general nomenclature adopted to the domain faces according to geographic orientation; in addition, the coordinate axis components are also presented.

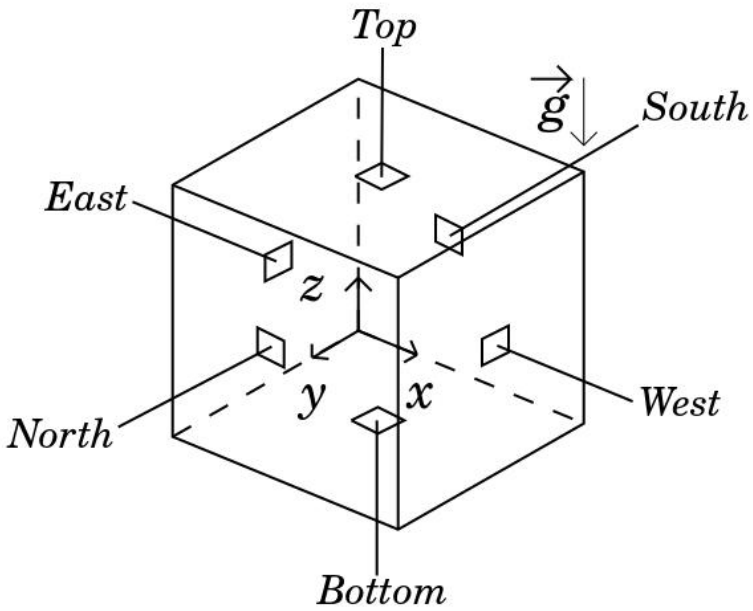

Figure 4.2: Three-dimensional view of the general computational domain of the simulations performed in the present work.

CHAPTER V

RESULTS

This chapter reports the results obtanied in the present thesis. All the results were presented and discussed according to literature previous results. The main results were here described in details; for further information and to cite the work found here, the readers are invited to read the papers published by the authors (DOI information is provided in the introduction chapter).

This chapter presents nine sections, namely:

1. Verification of the thermal energy equation;
2. Validation of the thermal energy equation;
3. Benchmark between OB and NOB;
4. Influence of dimensionless parameters in non-isothermal single-phase flows;
5. Influence of dimensionless parameters in non-isothermal two-phase flows;
6. Validation of the phase change model;
7. Investigation about the spurious currents in phase change problems;
8. Investigation about particular forces in phase change problems;
9. Case study of a Direct Contact Condensation (DCC) with a jet in cross-flow.

5.1 Numerical verification of the thermal energy equation in the MFSim code

The first step in the present work was the implementation of the thermal energy equation in the MFSim code. This implementation was based on the module of the transport equation of a generical scalar, which already was available in the MFSim code. Therefore, a new module was created in the MFSim code to hold the thermal energy equation.

Initially, the thermal energy equation was implemented in the divergent form and some simulations were conducted. The thermal energy equation in the divergent form is given by the following expression.

$$\frac{\partial(\rho C_p T)}{\partial t} + \vec{\nabla}.(\rho C_p T \vec{v}) = \vec{\nabla}.(k\vec{\nabla}T) + S_{reac} + S_{temp} \tag{5.1}$$

where $\vec{v}$ is the velocity, ρ is the specific mass, T is the temperature, k is the thermal conductivity, C_p is the specific thermal energy, S_{reac} is the reactional source term to account the phase change process and S_{temp} is the source term used to numerical verification procedure.

According to the literature review, it was suggested to employ the non-divergent form of the thermal energy equation as seen on the phase change works of Tanguy *et al.* (2014), Welch e Wilson (2000) and Lee, R. e Aute (2017). According to Deen e Kuipers (2013), the divergent form of the energy equation may pose some numerical difficulties since the divergent form of the thermal energy equation may lead to inconsistent physical generation of entrophy, and then a non-divergent form was needed.

The non-divergent form of the thermal energy equation was implemented and all the simulations presented in the present thesis employed these mathematical formulation as suggested by the literature. The non-divergent form of the thermal energy equation implemented in the MFSim code is given by the following expression:

$$\rho C_p \frac{\partial T}{\partial t} + \rho C_p \vec{\nabla}.(T\vec{v}) = \vec{\nabla}.(k\vec{\nabla}T) + S_{reac} + S_{temp}. \tag{5.2}$$

In this section, the verification procedure will be presented for the thermal energy equation implemented in the MFSim code. The verification procedure is the act of checking if a particular equation included in a code has been correctly written. Since the MFSim code uses a composite

grid, the verification process is conducted using more than one mesh level to test the code considering non-uniform grids.

The implementation of the thermal energy equation was verified by a procedure using the method of manufactured solutions in a cubic domain. The method of manufactured solutions is a technique by which numerical methods within computational codes can be verified to ensure that they have been implemented correctly.

The procedure of numerical verification is based on the calculation of the order of convergence of a given variable of interest. As the temperature is calculated using a second order numerical scheme, it was expected to obtain order of convergence of two. The order of convergence of a given method is the quotient of the error (between exact and numerical solution) by the refinement ratio (quotient of the number of cells used in the more refined mesh by the less refined mesh). The code verification was conducted according to Roache (1998).

In order to perform the verification procedure, an analytical solution was proposed for all the fluid and flow variables. The expressions defined to each flow variable were selected to preserve the flow physical characteristics as well as to ensure relevant variations in time and space, trying to test the variations which the variable would be subjected in a common physical problem to be simulated later. Therefore, all the fluid properties could not assume negative or null values and each variable was subjected to relevant variations inside the domain and through the simulation time.

The figure 5.1 illustrates the u-velocity component field at the simulation's final time.

The exact analytical solutions proposed for the velocities componenents, pressure, temperature, specific mass, dynamic viscosity, specific heat capacity and thermal conductivity are presented by the following expressions, respectively:

$$u_e(\vec{x}, t) = [sin(a_1\pi x + a_2\pi y + a_3\pi z + a_4 t)]^2, \tag{5.3}$$

$$v_e(\vec{x}, t) = -[cos(a_1\pi x + a_2\pi y + a_3\pi z + a_4 t)]^2, \tag{5.4}$$

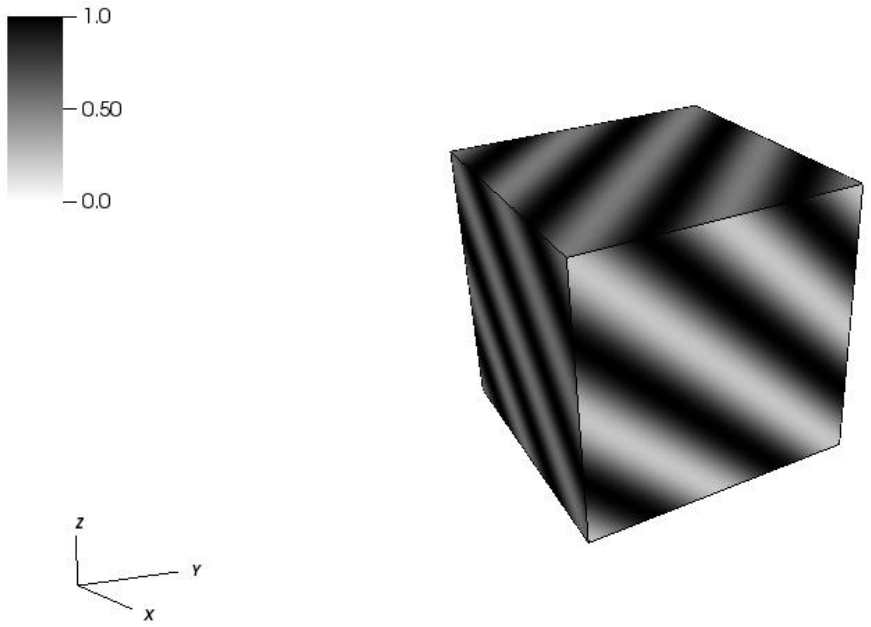

Figure 5.1: Three-dimensional view of the u-velocity component field at 10.0s.

$$w_e(\vec{x},t) = \frac{a_1(cos(a_1\pi x + a_2\pi y + a_3\pi z + a_4 t)^2)}{a_3} + \frac{a_2(cos(a_1\pi x + a_2\pi y + a_3\pi z + a_4 t)^2)}{a_3}, \tag{5.5}$$

$$p_e(\vec{x},t) = 1.1\{[cos(a_1\pi x + a_2\pi y + a_3\pi z + a_4 t)]^2\}, \tag{5.6}$$

$$T_e(\vec{x},t) = sin(a_1\pi x + a_2\pi y + a_3\pi z)cos(a_4 t), \tag{5.7}$$

$$\rho_e(\vec{x},t) = 1.2\{[a_1 + a_2(sin(a_1\pi x + a_2\pi y + a_3\pi z + a_4 t)]^2\}, \tag{5.8}$$

$$\mu_e(\vec{x},t) = 1.3\{[cos(a_1\pi x + a_2\pi y + a_3\pi z + a_4 t)]^2\}, \tag{5.9}$$

$$Cp_e(\vec{x},t) = 1.4\{[cos(a_1\pi x + a_2\pi y + a_3\pi z + a_4 t)]^2\}, \tag{5.10}$$

$$k_e(\vec{x},t) = 1.5\{[cos(a_1\pi x + a_2\pi y + a_3\pi z + a_4 t)]^2\}, \tag{5.11}$$

where a_1, a_2 and a_3 are 1 and a_4 is 2.

The verification was performed with structured non-uniform grids with two physical levels and the bottom level presented the configuration of $8\times8\times8$, $16\times16\times16$, $32\times32\times32$, $64\times64\times64$, $128 \times 128 \times 128$ cells. For each mesh configuration, the error between the numerical and the exact solution was calculated in all time-steps. In this study, the error was estimated by the L_2 norm, which was calculated using the following expression for a generic variable x:

$$L_2(x) = \sqrt{\frac{1}{NxNyNz}\sum_{k=1}^{Nz}\sum_{j=1}^{Ny}\sum_{i=1}^{Nx}(x_n - x_e)^2_{ijk}}. \tag{5.12}$$

where Nx, Ny and Nz are the number of cells used in spatial discretization, x_n is the numerical solution and x_e is the exact solution for a generic variable x.

The error estimation according to L_2 norm and the convergence ratio between a fine grid and a coarse grid were then calculated and analyzed at the simulation final time $(10s)$. As the grids configurations were sucessively refined by ratio of 2 and the temperature uses a second order scheme, it was expected to have convergence ratio of approximately 4 and order of convergence of 2.

The table 5.1 presents the grid configuration at the bottom physical level, the error between numerical and exact solution, the convergence ratio and the order of convergence.

According to the table 5.1, the error is sucessively reduced as the mesh becomes more refined and the order of convergence was approximately 2 for all the tests performed, indicating that the thermal energy equation was correctly coded in the MFSim code. Therefore, the MFSim code has been verified and one can conclude that it solves correctly the implemented thermal

Table 5.1: Grid configuration, error, refinement ratio, convergence ratio and order of convergence for temperature.

Grid	Error	Refinement ratio	Convergence ratio	Order of convergence
$8 \times 8 \times 8$	2.0513E-002	-	-	-
$16 \times 16 \times 16$	4.9221E-003	2	4.16	2.08
$32 \times 32 \times 32$	1.2228E-003	2	4.03	2.02
$64 \times 64 \times 64$	3.0598E-004	2	4.01	2.01
$128 \times 128 \times 128$	7.6630E-005	2	4.00	2.00

energy equation since it presents the expected order of convergence from the numerical method used.

5.2 Validation of the thermal energy equation in the MFSim code

In this section, four validation cases will be presented. First, the OB and NOB approaches were validated. The second case presents the simulation of natural convection in the classic (Differentially heated cavity) DHC problem. Then the third validation case shows the results from the simulation of natural convection with a bubble inside the cavity. Finally, the fourth validation case presents the performance of a simulation of the Rayleigh-Taylor instability in non-isothermal flow.

5.2.1 Validation case 1: OB and NOB models

Natural convection simulations in a cubic cavity assuming a Rayleigh number of 1.89×10^5 were performed using OB and NOB for validation purposes. Temperature profiles were plotted and then compared with the results of Krane and Jessee's experimental study (KRANE; JESSEE, 1983) and the numerical results of Padilla, Lourenco e Silveira-Neto (2013).

OB and NOB models were proposed for incompressible flows; therefore, the continuity equation represents irrelevant specific mass variations, as previously seen in Markatos e Pericleous (1984) and in Montiel-Gonzalez *et al.* (2015). During the computational simulation process, the velocity divergence was constantly evaluated in order to preserve the divergence-free velocity condition and it was never higher than 10^{-11} s^{-1}.

A uniform temperature field was imposed on the east (T_{high}) and west (T_{low}) walls. The south and north walls were considered adiabatic, and a linear temperature field, given by the

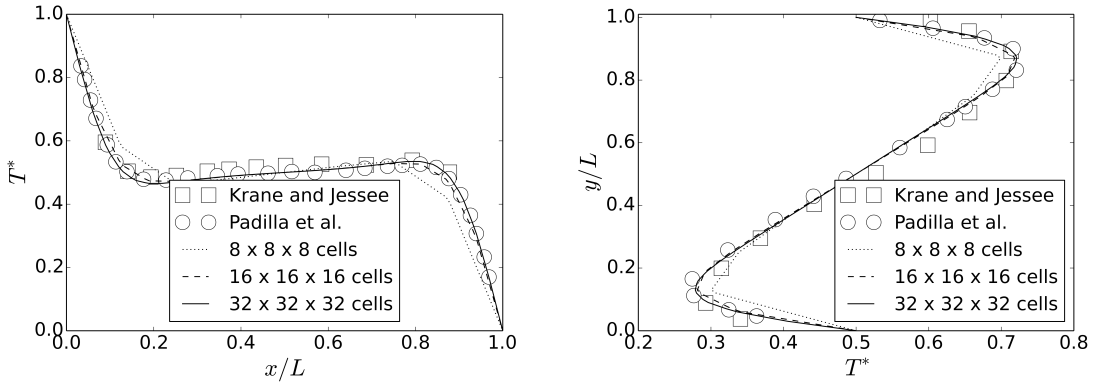

Figure 5.2: Dimesionless temperature along the line $T^*(x, L/2, L/2)$ and $T^*(L/2, y, L/2)$, respectively, for $Ra = 1.89 \times 10^5$ with OB

expression $T(x, y, 0) = T(x, y, L) = T_{high} - (T_{high} - T_{low})\frac{x}{L}$, was imposed on the bottom and top walls.

Two dimensionless temperature lines from inside the domain were extracted from the numerical results, namely, $T^*(x, L/2, L/2)$ and $T^*(L/2, y, L/2)$. Figures 5.2-a and 5.3-a present the dimensionless temperature along the line $T^*(x, L/2, L/2)$ for OB and NOB, respectively. Likewise, Figs 5.2-b and 5.3-b present the dimensionless temperature along the line $T^*(L/2, y, L/2)$ for OB and NOB, respectively. In order to demonstrate the agreement of the results with the literature, Figs. 5.2 and 5.3 present the numerical results from three different meshes. The expression for the dimensionless temperature is given by

$$T^*(dimensionless) = \frac{T}{T_{east} - T_{west}}, \tag{5.13}$$

where T_{east} represents the temperature at the east wall and T_{west} represents the temperature at the west wall.

The simulations using OB demonstrated good agreement with the experimental data of Krane e Jessee (1983) and with the numerical data of Padilla, Lourenco e Silveira-Neto (2013), as observed in Fig.5.2. The numerical results from the present paper are slightly closer to those reported in the numerical work of Padilla, Lourenco e Silveira-Neto (2013) than those from the experimental work of Krane e Jessee (1983). The NOB results also presented good agreement with Krane e Jessee (1983) and Padilla, Lourenco e Silveira-Neto (2013), as shown in Fig.5.3.

The average relative difference (ε) between the experimental data and the computed values

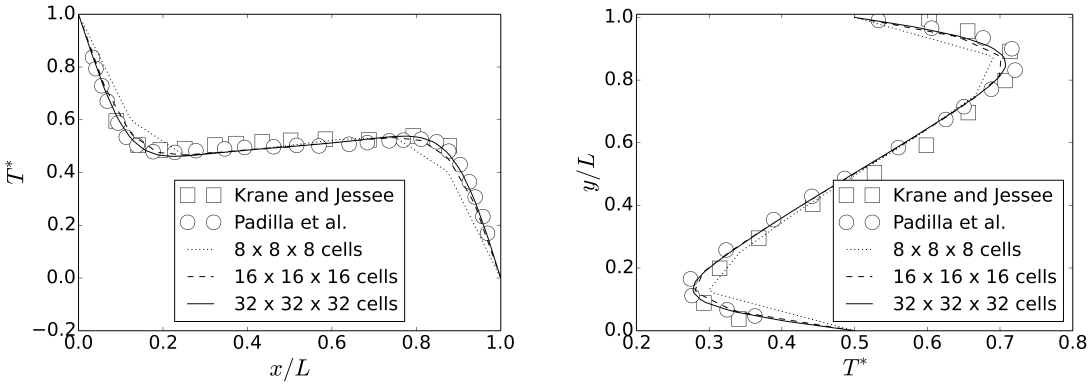

Figure 5.3: Dimensionless temperature along the line $T^*(x, L/2, L/2)$ and $T^*(L/2, y, L/2)$, respectively, for $Ra = 1.89 \times 10^5$ with NOB

Table 5.2: Average relative difference (ε) between OB and NOB from experimental data of Krane e Jessee (1983)

Mesh configuration	ε (%) using NOB	ε (%) using OB
$8 \times 8 \times 8$	6.3	6.5
$16 \times 16 \times 16$	5.1	5.1
$32 \times 32 \times 32$	4.9	4.9

from the present work are shown in Table 5.2. According to the results seen in Table 5.2, OB and NOB provide numerical results with low deviation from the experimental data of Krane e Jessee (1983). In addition, the maximum difference between the experimental data and NOB was 7.3%, and 7.3% between OB and Krane e Jessee (1983) for the most fine grid.

In order to present a grid quality analysis, the dimensionless temperatures obtained for the three different meshes were compared. The temperature from the line $T^*(x, L/2, L/2)$ was chosen for the comparison between the different meshes. Tables 5.3 and 5.4 show the data for $x/L = 0.2$, $x/L = 0.5$ and $x/L = 0.8$ using NOB and OB, respectively. The relative difference between two sucessive grid configurations (ψ) is also presented in tables 5.3 and 5.4.

Since the temperature field is solved using a second-order scheme, it is expected that the error found for a grid with size ζ is four times lower than the error obtanied for a grid with size 2 ζ. When the relative difference between the error obtanied for two grids is significantly low and its values are close to the reference, it is assumed that this grid present good quality. As seen in table 5.3 and 5.4, the grid configuration of $32 \times 32 \times 32$ present a great quality since its values

Table 5.3: Dimensionless temperature for NOB for $x/L = 0.2$, $x/L = 0.5$ and $x/L = 0.8$ from the line $T^*(x, L/2, L/2)$

Mesh configuration	$x/L = 0.2$	$\psi(\%)$	$x/L = 0.5$	$\psi(\%)$	$x/L = 0.8$	$\psi(\%)$
$8 \times 8 \times 8$	0.52	-	0.50	-	0.48	-
$16 \times 16 \times 16$	0.47	10.63	0.50	0	0.52	7.69
$32 \times 32 \times 32$	0.46	2.17	0.50	0	0.53	1.88

Table 5.4: Dimensionless temperature for OB for $x/L = 0.2$, $x/L = 0.5$ and $x/L = 0.8$ from the line $T^*(x, L/2, L/2)$

Mesh configuration	$x/L = 0.2$	$\psi(\%)$	$x/L = 0.5$	$\psi(\%)$	$x/L = 0.8$	$\psi(\%)$
$8 \times 8 \times 8$	0.51	-	0.50	-	0.49	-
$16 \times 16 \times 16$	0.47	8.51	0.50	0	0.53	7.54
$32 \times 32 \times 32$	0.46	2.17	0.50	0	0.53	0

are very close to the experimental data from the literature (seen in table 5.2), as well as, the relative difference between the error with the courser grid is not relevant compared to the grid of $32 \times 32 \times 32$. Therefore, based on the numerical results obtained in the simulations presented in this section, it can be concluded that both formulations are in accordance with the literature, assuring the accuracy of the numerical methods employed.

Finally, the mean Nusselt number at the east wall was computed in order to compare it with the data in the literature. Although Krane e Jessee (1983) and Padilla, Lourenco e Silveira-Neto (2013) did not calculate the Nusselt number for $Ra = 1.89 \times 10^5$, Leong, Hollands e Brunger (1999) presented an experimental Nusselt number value for $Ra = 1.0 \times 10^5$ using similar conditions. The Nusselt number found by Leong, Hollands e Brunger (1999) was 3.10 and, in the present paper, was 3.17 for OB and NOB. Hence, the mean Nusselt number is close to the expected value despite the small difference in the Rayleigh number between the literature and the present paper.

5.2.2 Validation case 2: Simulations of natural convection in single-phase flows

Natural convection in single-phase flow was examined using the Oberbeck-Boussinesq approximation. The simulations were performed considering Prandtl number of 0.71 and a range of

Rayleigh numbers from $Ra = 1.0 \times 10^3$ to $Ra = 1.0 \times 10^6$.

Null velocities and null pressure gradient were imposed to all the domain faces. The east and west walls have, respectively, a uniform high and low temperature. The south, north, bottom and top walls are adiabatic.

Isotherms were analyzed in the central xz-plane in the figure 5.4 and compared qualitatively to Wan, Patnaik e Wei (2001) in the figure 5.5.

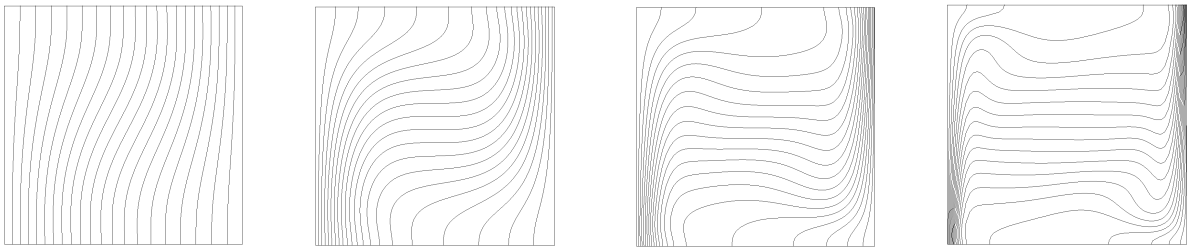

(a) (b) (c) (d)

Figure 5.4: Isotherms of the present study at central xz-plane for $Pr = 0.71$ and: (a) Ra=1.0×10^3; (b) Ra=1.0×10^4; (c) Ra=1.0×10^5 and (d) Ra=1.0×10^6.

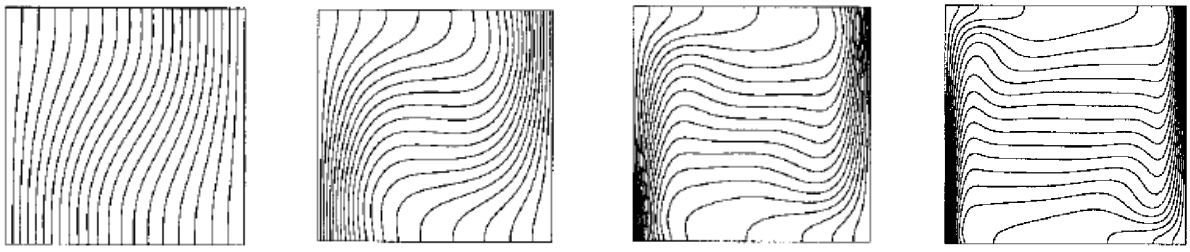

(a) (b) (c) (d)

Figure 5.5: Isotherms of the Wan, Patnaik e Wei (2001) at central xz-plane for $Pr = 0.71$ and: (a) Ra=1.0×10^3; (b) Ra=1.0×10^4; (c) Ra=1.0×10^5 and (d) Ra=1.0×10^6.

The isotherms from the present work (figure 5.4) were very similar from those found by Wan, Patnaik e Wei (2001) (figure 5.5). As reported by Padilla, Lourenco e Silveira-Neto (2013), it was observed that the isotherms topology became more complex as Rayleigh number increases.

The spatial mean Nusselt number at the east wall was calculated and a good agreement was found between the present work and the literature previous works, as shown at the table 5.5.

Since the Prandtl number was considered 0.71 in all the simulations and the Rayleigh number is the product of the Grashof and Prandtl numbers, the variations of the Rayleigh number refered to the augmentation of Grashof number. Therefore, the increasement of the Grashof

Table 5.5: Spatial mean Nusselt number at the east wall for a range of Rayleigh numbers.

	$\mathrm{Ra} = 10^3$	$\mathrm{Ra} = 10^4$	$\mathrm{Ra} = 10^5$	$\mathrm{Ra} = 10^6$
Padilha et al.	1.072	2.068	4.427	8.865
Tric et al.	1.070	2.054	4.337	8.641
Fusegi et al.	1.085	2.100	4.361	8.770
Present work	1.072	2.090	4.390	8.901

number has increased the local thermal transfer rate, as the spatial mean Nusselt number measurements have shown.

The results of the calculation of the spatial mean Nusselt number at the heated wall from the table 5.5 were in good agreement with other 3d works from the literature. The figure 5.6 shows the 3d view of the domain simulated with the isotherms in the central plane. The

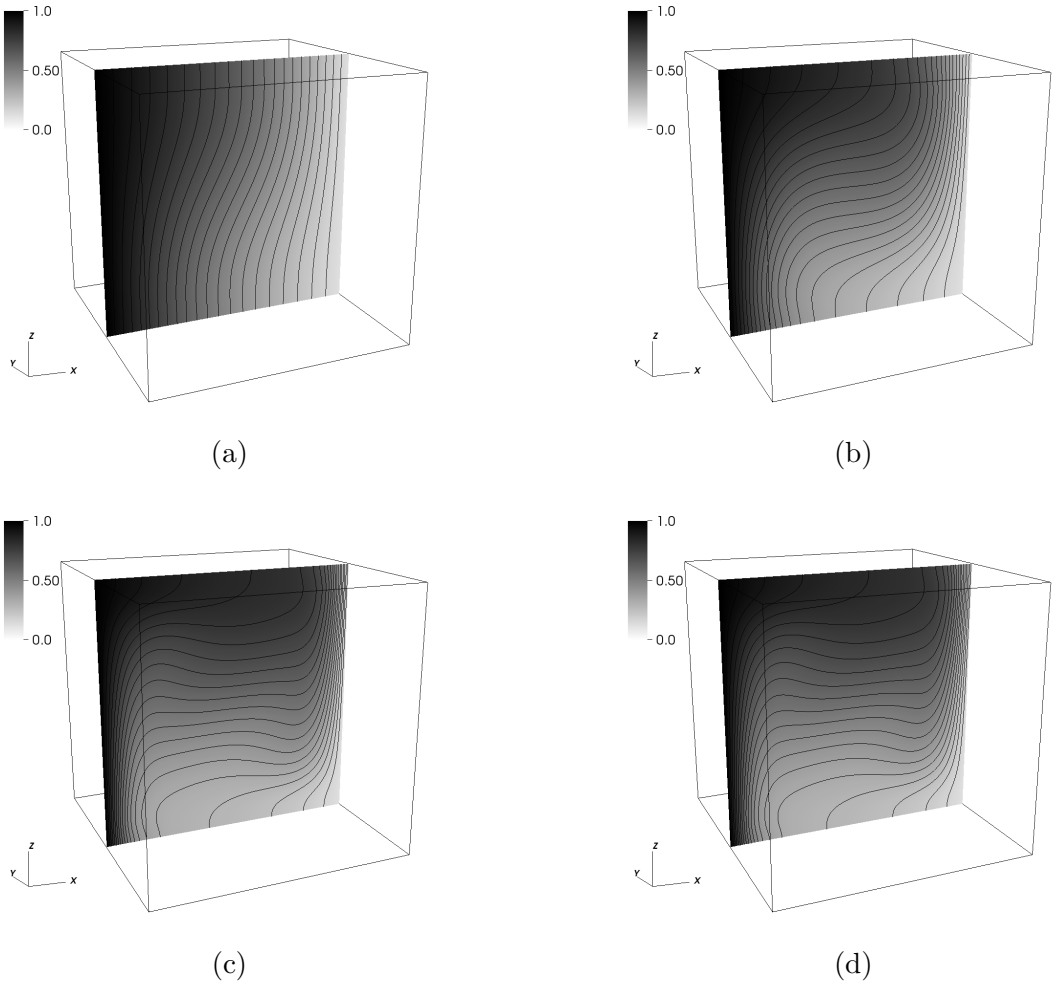

Figure 5.6: Isotherms from the present work with the isotherms at the central xz-plane for $Pr = 0.71$ and: (a) Ra=1.0×10^3; (b) Ra=1.0×10^4; (c) Ra=1.0×10^5 and (d) Ra=1.0×10^6.

visualization of the isotherms from the figure 5.6 confirmed the severe influence of the Grashof

number variations in the isotherms pattern.

The second validation case presented in this subsection showed a good quantitative and qualitative comparison with previous literature works. Next, a validation case considering two-phase flows is reported.

5.2.3 Validation case 3: Simulations of natural convection in two-phase flows

Natural convection in two-phase flow was simulated and validated by the calculation of the spatial mean Nusselt number at the east wall. Qiu, Wang e Jiang (2014) presented this numerical experiment of natural convection with two-phase flow using Oberbeck-Boussinesq approximation (since the specific mass was the same for the two fluids, and the other fluid properties were different).

Null velocities and null pressure gradient were imposed to all the domain faces. The east and west walls have, respectively, a uniform high (T_h) and low temperature (T_l). The south, north, bottom and top walls are adiabatic. The fluid is at rest in initial conditions and the temperature field is uniform and igual to T_l.

The Prandtl number was set as 0.71 and Rayleigh number was 10^3 for the dispersed phase and 10^4 for continuos phase. The dispersed phase consisted of a bubble in the center of the cavity. Two values of initial bubble radius were tested, namely: $0.15L$ and $0.31L$. The wall-to-fluid thermal transfer rate was examined by means of the spatial mean Nusselt number calculation. A computational grid with one level of refinement was employed and the base level presented $64 \times 64 \times 64$ cells.

The figure 5.7 shows the isotherms in the cases of a bubble initial radius of $0.15L$ and $0.31L$, respectively.

The presence of the bubble changed significantly the thermal transfer pattern inside the cavity as shown in the figure 5.7. As seen in the figure 5.7, the isotherms tend to be more vertical inside the bubble, as found by Qiu, Wang e Jiang (2014). The figure 5.8 shows the clockwise movement described by the bubble inside the cavity due to thermal bouyancy effects, as previously reported by Qiu, Wang e Jiang (2014).

A 3D visualization of the interface contour is shown in the figure 5.9

The spatial mean Nusselt number presented good agreement with Qiu, Wang e Jiang

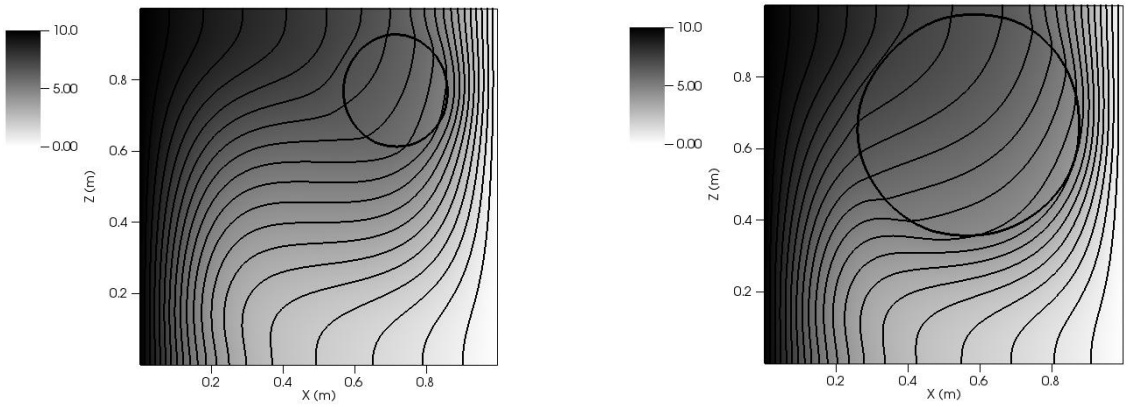

(a) (b)

Figure 5.7: Isotherms at central xz-plane for $r = 0.15L$ (a) and $r = 0.31L$ (b). Interface is represented by a contour line.

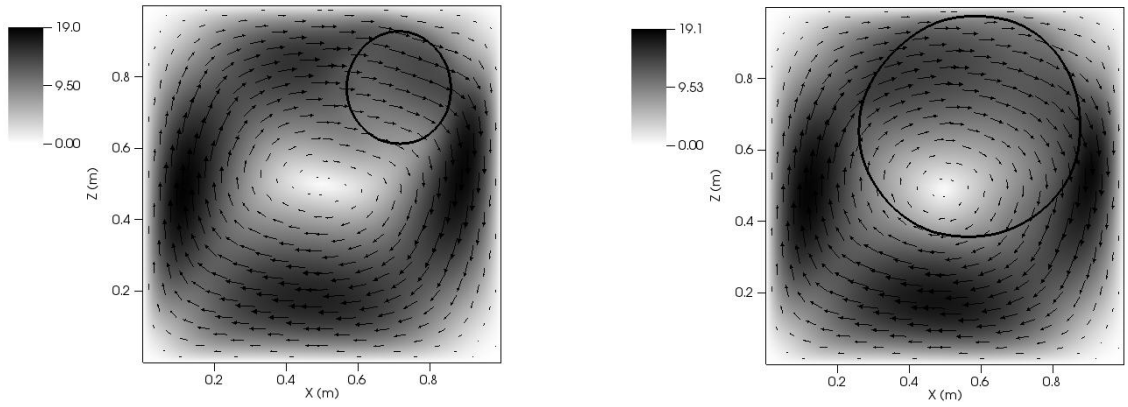

(a) (b)

Figure 5.8: Velocity field at the central xz-plane considering $r = 0.15L$ (a) and $r = 0.31L$ (b). The interface is represented by a contour line.

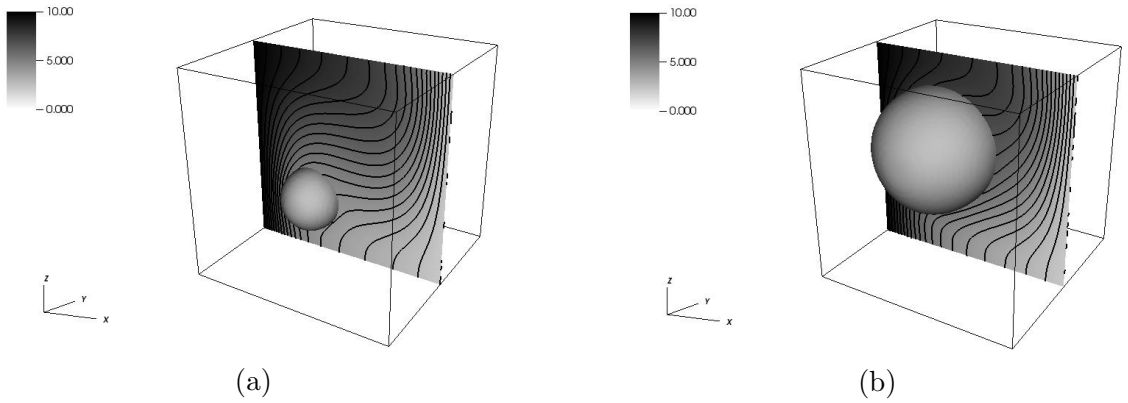

(a) (b)

Figure 5.9: Temperature and isotherms visualization for $r = 0.15L$ (a) and $r = 0.31L$ (b). The interface is represented by a contour line.

(2014) for the two different initial radius tested. The table 5.6 shows the spatial mean Nusselt number found in the present paper and the ones found from the literature.

The introduction of a bubble with a larger radius caused the reduction of the spatial mean

Table 5.6: Spatial mean Nusselt number at the east wall for two values of bubble's initial radius.

	Bubble radius of $0.15L$	Bubble radius of $0.31L$
Qiu, Wang e Jiang (2014)	2.13	2.08
Present work	2.03	2.00

Nussselt number at the heated wall, similarly to the results found by Qiu, Wang e Jiang (2014). Therefore, the influence of the Grashof number in the local thermal transfer was significantly visible in the previous table, since the overall Grashof number was lowered by the introduction of a dispersed phase.

5.2.4 Validation case 4: Numerical simulations of a Rayleigh-Taylor instability

This validation case consisted of modelling a Rayleigh-Taylor instability simulated in non-isothermal two-phase flow in a three-dimensional cavity with height aspect ratio of one. Null velocities and null pressure gradient were imposed to all the domain faces. The bottom and top walls have, respectively, a uniform high and low temperature. The south, north, west and east walls were considered adiabatic.

In order to simulate the Rayleigh-Taylor instability, a numerical pertubation must be applied to the physical model to promote the development of this flow instability. Then, the interface was initialized with trigonometric functions in order to create an initial pertubation, as proposed by Akhtar e Kleis (2013). The interface was initialized with a function that combines a reference height (Y_r) with trigonometric functions, given by the following expression:

$$Y = Y_r - A\left[\cos\left(\frac{2\pi x}{L}\right) + \sin\left(\frac{\pi x}{L}\right) + \cos\left(\frac{2\pi y}{L}\right) + \sin\left(\frac{\pi y}{L}\right)\right], \tag{5.14}$$

where A is the amplitude and L is the characteristic length of the problem.

As mentioned by Akhtar e Kleis (2013), the critical wavelength (λ_c) of this pertubation is given by the following expression:

$$\lambda_c = 2\pi\sqrt{\frac{\sigma}{g(\rho_h - \rho_l)}}, \tag{5.15}$$

where: λ_c is the critical wavelength of a given pertubation, σ is the interfacial tension coefficient,

ρ_h is the specif mass of the heavier fluid and ρ_l is the specif mass of the lighter fluid.

Any pertubation that has wavelength smaller than the critical one for the given problem will be dumped (SHARP, 1984). On the other hand, any pertubation that has the same or larger wavelength than the critical one will be amplified and then Rayleigh-Taylor instability will develop. In the present work, a test case was simulated where the wavelength of the initial pertubation (0.99m) was slightly smaller than the critical one (1.00m). As expected, the pertubation was dumped and the interface returned to the equilibrium position. According to Sharp (1984), the surface tension stabilizes pertubations with wavelength smaller than the critical one.

The two most relevant parameters that characterize Rayleigh-Taylor instabilities are the Atwood and Weber number (SHARP, 1984; TRYGGVASON, 1988), which are given respectively by the following expressions:

$$A = \frac{\rho_h - \rho_l}{\rho_h + \rho_l}, \tag{5.16}$$

$$We = \frac{2\sigma}{g(\rho_h - \rho_l)\lambda^2}, \tag{5.17}$$

where λ is the wavelength of the given pertubation.

The simulation performed presented $A = 0.65$ and $We = 0.0053$. The relation between lighter (l) and heavier (h) fluid properties were the same as Akhtar e Kleis (2013) employed. The data used in the simulation was presented at the table 5.7.

Table 5.7: Data used in the simulations of modelling a Rayleigh-Taylor instability in non-isothermal flows.

Parameter	Value
Domain size (m)	$1.12 \times 1.12 \times 1.12$
Amplitude of initial perturbation (m)	0.018
ρ_h/ρ_l	4.780
$\mu_h/\ \mu_l$	2.590
$k_h/\ k_l$	3.560
$Cp_h/\ Cp_l$	0.660
Gr number	17.93
Gravity acceleration (N/m^2)	9.810
Mesh size in the most refined level (m)	$1.604\ 10^{-2}$

Adaptive mesh refinement was employed in order to reduce the computational costs. The refinement criteria was the presence of the interface, since the interest here was the instability which develops at the interface. Four mesh levels were used and the bottom level presented $16 \times 16 \times 16$ cells. The figures 5.10,5.11,5.12 illustrate the evolution of the interface in time with the adaptive mesh refinement employed.

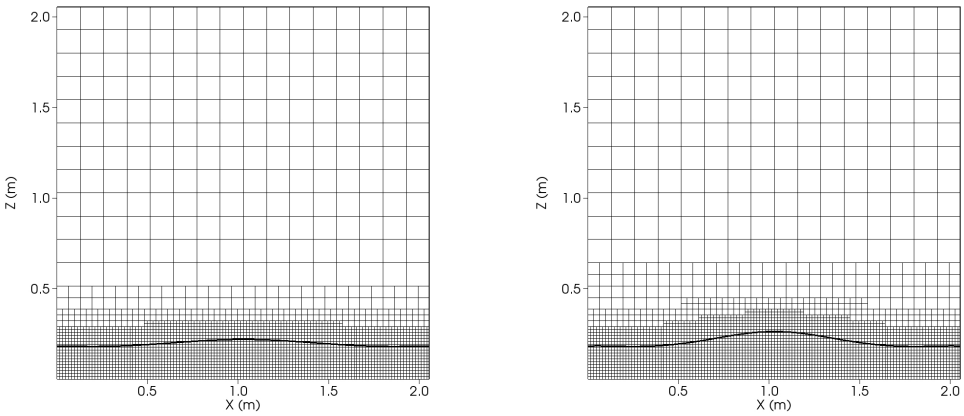

(a) (b)

Figure 5.10: Frontal view of the central xz-plane with interface evolution using adaptive mesh at times 2.25s (a), 4.49s (b).

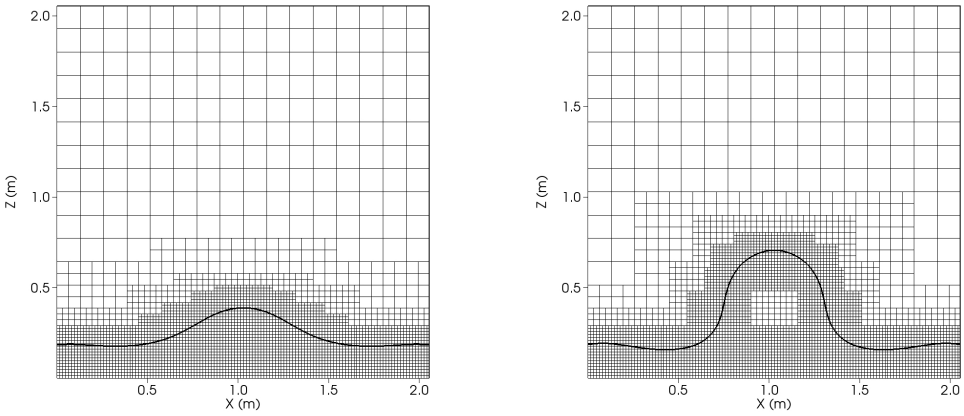

(a) (b)

Figure 5.11: Frontal view of the central xz-plane with interface evolution using adaptive mesh at times 6.74s (a), 8.99s (b).

Adaptive mesh refinement promote great reduction of computational costs, because as the figures 5.10,5.11,5.12 shows, the regions away from the interface have a course grid, which helps the simulation to run faster than with a uniform grid. Since the interface is the region where the phenomena is developed, the other regions of the domain can be solved with a relatively course

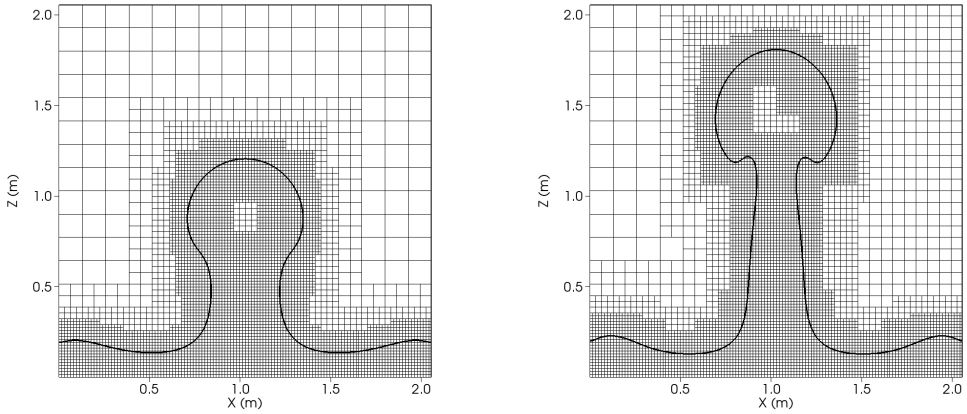

(a) (b)

Figure 5.12: Frontal view of the central xz-plane with interface evolution using adaptive mesh at times 11.24s (a) and 13.48s (b).

grid. The region of course grid represents more than half of the domain total volume, specially at the beginning of the simulation, until 8.99s. If a uniform grid was employed using the most refined level in adaptive mesh simulation, the total number of cells would be 2,097,152. On the other hand, using adaptive mesh refinement, the total number of cells is 365,600 at 8.99s and 599,960 cells at 13.48s. Therefore, at the beginning of the simulation, the number of cells needed in simulation with adaptive mesh refinement is more than 5 times lower than simulations using a uniform grid and, at the end, is more than 3 times lower.

The Rayleigh-Taylor instability is developed more slowly at the beginning of the simulation. The instability is developed in a faster mode when the velocity vectors, that promotes the baroclinic torque at the interface, increases in module. This behaviour was previously reported by Tryggvason (1988). The mushroom-shapped bubble became more evident at the final stage of the simulation.

In order to understand the thermal transfer and the fluid dynamics in this simulation, the isotherms and velocity vectors were analyzed. The figure 5.13 presents the frontal view of the central xz-plane with, respectively, isotherms (colored by temperature) and velocity vectors (colored by velocity vector magnitude).

The isotherms in the figure 5.13 presented a visible thermal stratification and are slightly curved at the interface. The velocity vectors at the figure 5.13 presents the rotational characteristic of this flow, where the effects of the baroclinic torque, previously mentioned, is evident.

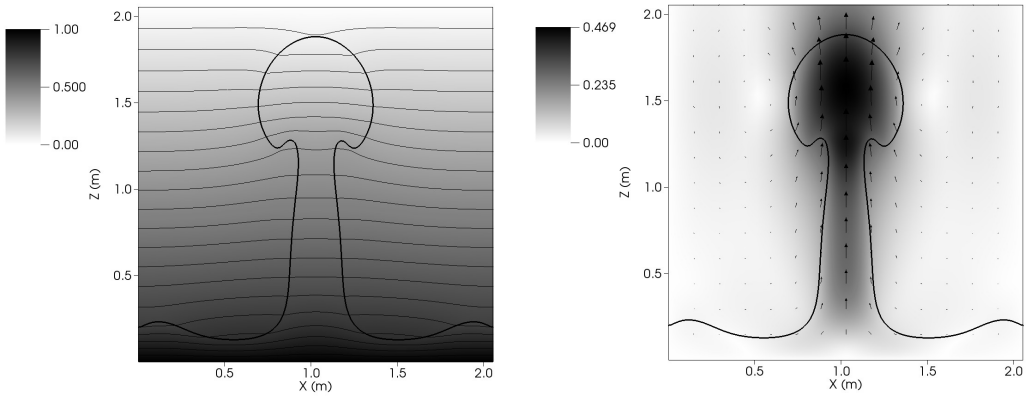

(a) (b)

Figure 5.13: Isotherms (a), velocity vectors (b) at time 13.48s.

The vapor mass that emerges from the bottom of the cavity has the higher velocity module of the domain.

According to the figure 5.13, at time 13.48s, vapor jet is well developed with mushroom shape and bubble break off does not occur as described by Akhtar e Kleis (2013). At this stage, the spatial mean Nusselt number at the bottom wall becomes almost constant. The spatial mean Nusselt number found by Akhtar e Kleis (2013) was 1.70 and in the present work it was found the value of 1.64. The spatial mean Nusselt number presents very good agreement with Akhtar e Kleis (2013), even though mass transfer was not taken into account in the present task. Since Jakob number is very low at this case (0.071), the effects of phase change are very low and thermal transfer was not strongly affected by mass transfer.

A three-dimensional view of the Rayleigh-Taylor instability at 13.48s is shown in the figure 5.14. In the figure 5.14 the two coherent structures that compose Rayleigh-Taylor instability are evident of identification. Firstly, there are four noticeable spikes (fluid structure of heavy fluid growing into light fluid) and, secondly, one mushroom-shaped bubble (fluid structure of light fluid growing into heavy fluid).

In order to verify how Atwood number would affect thermal transfer and flow pattern, a simulation with a lower Atwood number was performed. The properties were all the same used in the previous simulations, except the relation between specific mass of the lighter and heavier fluid, which were defined as $\rho_h/\rho_l = 2$. Then, the Atwood number employed in the next simulation was 0.33.

The figures 5.15,5.16 and 5.17 show the evolution of the interface with the adaptive mesh

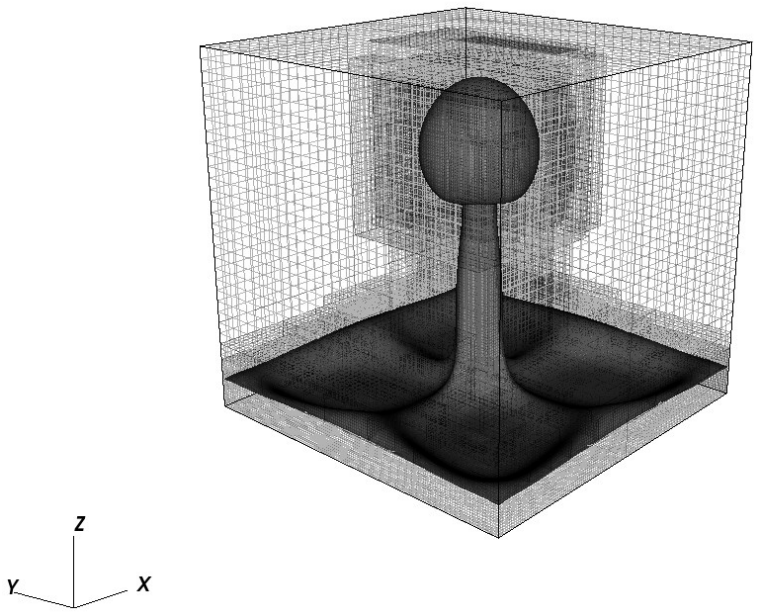

Figure 5.14: Rayleigh-Taylor instability at 13.48s.

refinement employed for $A = 0.33$ and $We = 0.0053$.

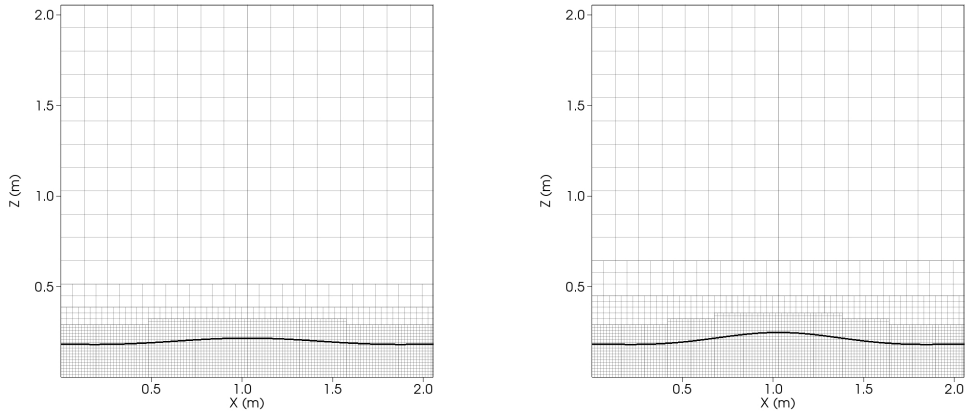

(a) (b)

Figure 5.15: Interface evolution with adaptive mesh at times 9.05s (a), 18.09s (b) for $A = 0.33$.

As described by Andrews e Dalziel (2010), a smaller Atwood number implicates that the Rayleigh-Taylor instability takes more time to develop. The Rayleigh-Taylor instability took 54.29s to develop for $A = 0.33$ and 13.48s for $A = 0.65$, which represents approximately 4 times more. As the previous simulation with higher Atwood number, adaptive mesh refinement presented a very significant reduction of computational costs. The more refined regions consist of small portions of the domain, specially at the beginning of the simulation.

The figure 5.18 presents the isotherms (colored by the temperature) and velocity vectors

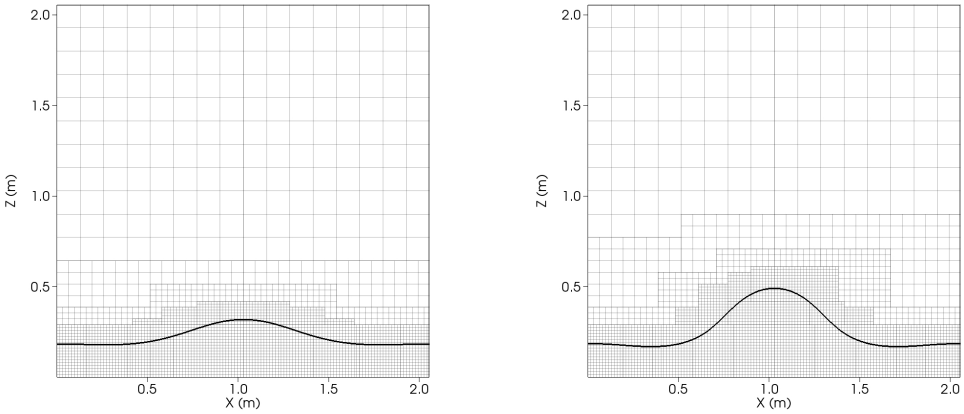

(a) (b)

Figure 5.16: Interface evolution with adaptive mesh at times 27.14s (a), 36.19s (b) for $A = 0.33$.

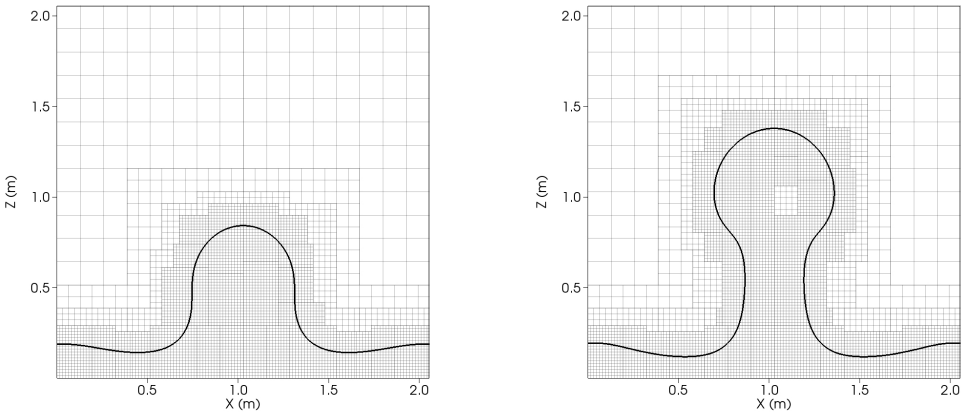

(a) (b)

Figure 5.17: Interface evolution with adaptive mesh at times 45.24s (a) and 54.29s (b) for $A = 0.33$.

(colored by velocity vector magnitude). According to the figure 5.18, the isotherms and the velocity vectors presented similar characteristics of the previous simulation with higher Atwood number. Nevertheless, a less pronounced mushroom shape is observed in the simulation of lower Atwood number. Andrews e Dalziel (2010) corroborate this result mentioning that lower specific mass differences between the two fluids reduces this mushroom aspect.

The spatial mean Nusselt number calculated at the bottom wall also presented a constant value after vapor jet is developed and no bubble break-off was observed. The spatial mean Nusselt number found at this stage was 1.51, which is about 8% smaller than the previous simulation with higher Atwood number. As the specific mass differences are the main force in this type of

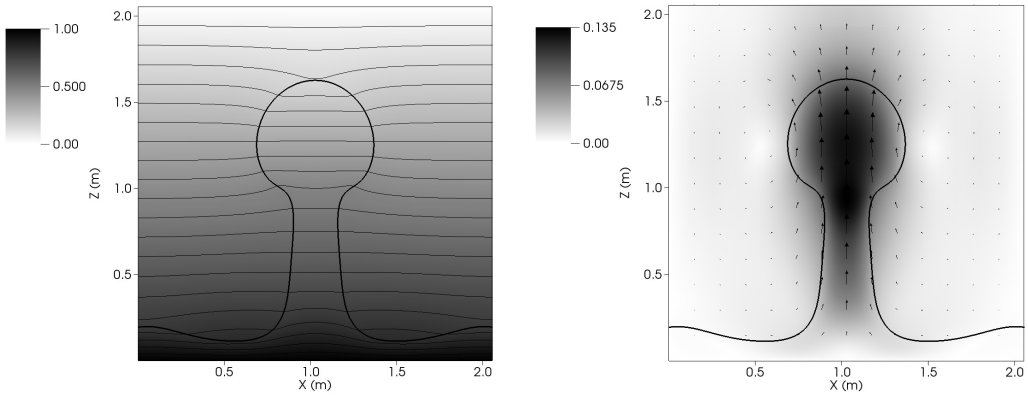

(a) (b)

Figure 5.18: Isotherms (a), velocity vectors (b) at time 54.29s.

flow, if specific mass gradient is less pronounced, it should be expected that thermal transfer may be less significant by the reduction of flow advection. Therefore, the result found corroborates the physical behavior expected.

The figure 5.19 shows the Rayleigh-Taylor instability with Atwood number of 0.33. The

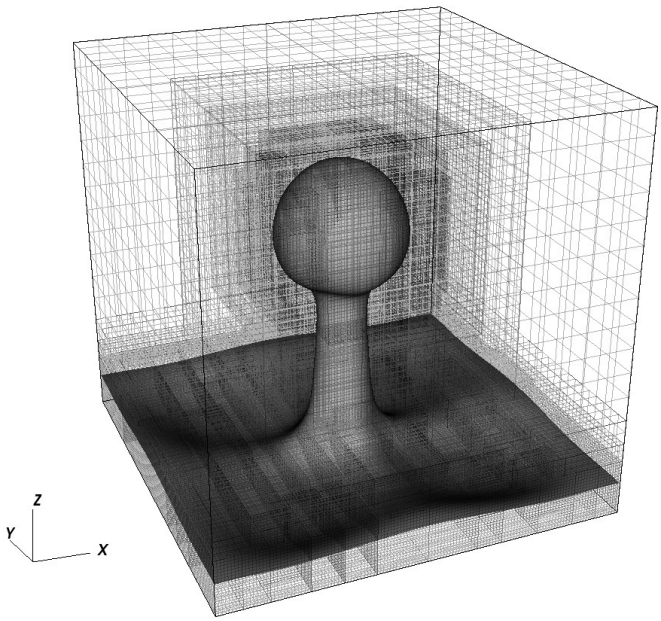

Figure 5.19: Rayleigh-Taylor instability at 54.29s considering Atwood number of 0.33.

figure 5.19 shows the coherent structures that compose Rayleigh-Taylor instability for Atwood number of 0.33. As the previous simulation with higher Atwood, there are four noticeable spikes and one bubble that evolves in a mushroom shape.

This fourth validation case reported good agreement in the thermal transfer rate measurements considering two-phase flows.

The computational model was subjected to a rigourous validation procedure and, according to the results found in these last four validation cases, the thermal energy equation from the MFSim code provides the possibility to model accurately non-isothemal flows for even complex cases, in laminar or turbulent regime and in single-phase and two-phse flows.

5.3 Benchmark between Oberbeck-Boussinesq approximation (OB) and a new temperature-dependent specific mass approach (NOB)

In this subsection, the results of the traditional Oberbeck-Boussinesq approximation (OB) and the new temperature-dependent specific mass approach (NOB) proposed by the present work were analyzed. A benchmark between OB and NOB is conducted and the qualitative and quantitative results are presented.

In the present work, the results of natural convection simulations for single-phase flows were presented for a large range of Rayleigh numbers, namely, from the laminar to the turbulent regime, and the numerical results are quantitatively and qualitatively analyzed. The flow pattern is illustrated using velocity, vorticity and temperature fields even for high Rayleigh numbers (up to $Ra = 10^{10}$), which is notably scarce in the literature.

Natural convection simulations in a cubic cavity for Rayleigh numbers from 10^4 up to 10^{10} were performed in order to evaluate NOB. Simulations using OB were also performed in order to examine the differences between the results of OB and NOB.

A uniform temperature field was imposed on the east (T_{high}) and west (T_{low}) walls. A linear temperature profile given by $T(x, y, 0) = T(x, y, L) = T(x, 0, z) = T(x, L, z) = T_{high} - (T_{high} - T_{low})\frac{x}{L}$ was imposed on the bottom, top, south and north walls for simulations with Rayleigh numbers up to 10^8. The simulation with $Ra = 10^{10}$ was performed using a different thermal boundary condition, in which the bottom, top, south and north walls were considered adiabatic. The velocity, vorticity, and isotherm fields were analyzed in the central xz-plane.

All the simulations were performed with the same mesh resolution. Since the simulation of $Ra = 10^{10}$ represents the condition where the mesh resolution is the most critical, a grid quality study was performed in order to define the mesh configuration most suitable for all the simulations. The mean thermal transfer rate at the east wall from the simulations with $Ra = 10^{10}$

Table 5.8: Mean Nusselt number (Nu), differences between different mesh configurations (ψ) and between the computed values using NOB and the experimental correlation of Cowan, Lovegrove e Quarini (1982) (ε) for $Ra = 10^{10}$.

Mesh configuration	Nu	$\psi(\%)$	$\varepsilon(\%)$
$32 \times 32 \times 32$	79.15	-	14.57
$64 \times 64 \times 64$	88.97	11.03	3.96
$128 \times 128 \times 128$	92.21	3.51	0.47

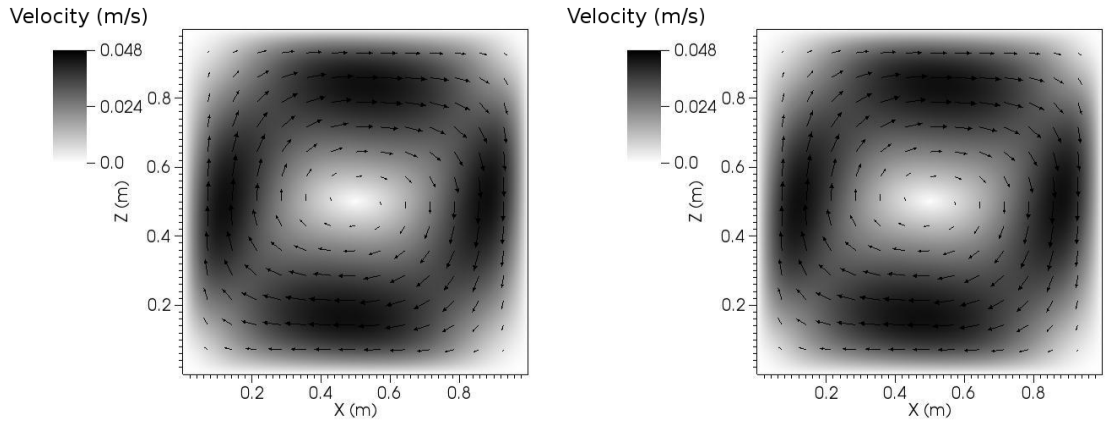

Figure 5.20: Velocity in central xz-plane for $Ra = 10^4$ with OB (left) and NOB (right)

were compared with an experimental correlation available in Cowan, Lovegrove e Quarini (1982). According to Cowan, Lovegrove e Quarini (1982), the mean Nusselt number at the east wall can be found to be $\bar{Nu} = 0.043 Ra^{\frac{1}{3}}$. Table 5.8 presents the difference between the computed values using NOB and the experimental correlation of Cowan, Lovegrove e Quarini (1982) for $Ra = 10^{10}$ using the mesh configurations of 32^3, 64^3, 128^3 cells. The relative difference between two sucessive grid configurations (ψ) is also presented in the table 5.8. According to the numerical results in Table 5.8, the mesh configuration of $128 \times 128 \times 128$ cells provided results with low enough differences from the literature. In order to guarantee the numerical accuracy of the results from the present paper, all the simulations were performed using the mesh configuration of $128 \times 128 \times 128$ cells, since this mesh resolution was considered adequate for even the most demanding flow condition.

Figure 5.20 shows the instantaneous velocity magnitude in grayscale and the velocity vectors using OB and NOB for the Rayleigh number of 10^4.

No qualitative differences between OB and NOB related to the velocity field were noticed in

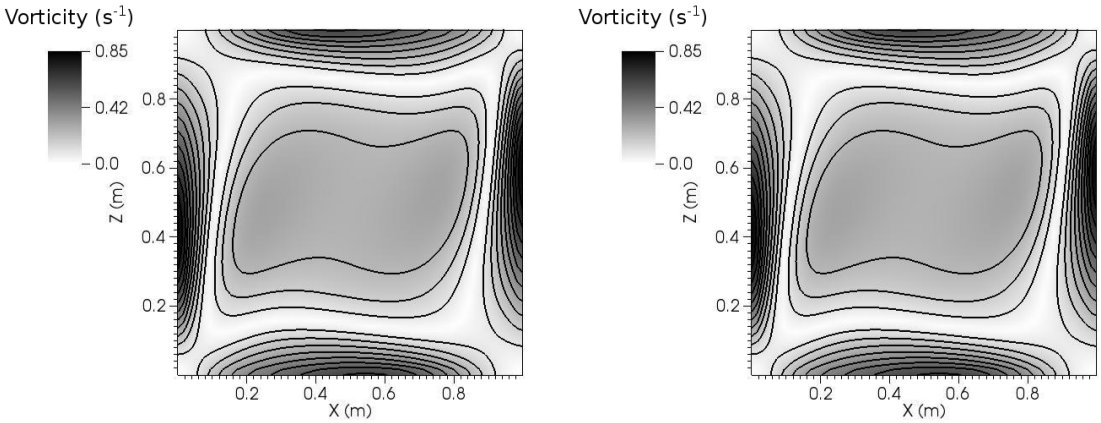

Figure 5.21: Vorticity in central xz-plane for $Ra = 10^4$ with OB (left) and NOB (right)

Fig. 5.20. The magnitudes of the velocities for both approaches were similar, and the maximum and minimum values were visibly the same in the central xz-plane. The velocity vectors presented in Fig. 5.20 show the rotational characteristics of this flow, represented by a large clockwise recirculation. Both approaches present lower velocity regions (brighter areas) in the corners and at the center of the cavity as well as higher velocity regions (darker areas) alongside the walls. A high mixture potential for the $Ra = 10^4$ simulations is observed, since the flow is greatly boosted by the velocity field in a large area of the domain.

Figure 5.21 illustrates the instantaneous magnitude of the vorticity in grayscale and the vorticity isovalue lines for $Ra = 10^4$ using OB and NOB. No qualitative differences between OB and NOB were noticed related to the vorticity in Fig. 5.21. The magnitude of the vorticity presented identical maximum and minimum values for OB and NOB. There are high values of the magnitude of the vorticity (darker areas) close to the walls and medium values (middle areas) in the center of Fig. 5.21. The corners and other regions have low values of vorticity (brighter areas). A large magnitude of the vorticity is expected at the walls due to the high values of the shear stresses. Vorticity is mainly produced where high velocity magnitude areas are close to low velocity regions (near walls), as previously shown in Fig. 5.21. The vorticity has a clockwise rotation, as pointed out by Markatos e Pericleous (1984).

Figure 5.22 shows the instantaneous temperature field for OB and NOB simulations considering $Ra = 10^4$. No qualitative differences between OB and NOB were noticed related to the temperature in Fig. 5.22. The isotherms seen in Fig. 5.22 have the same behavior for OB and NOB, as well as the temperature field in grayscale.

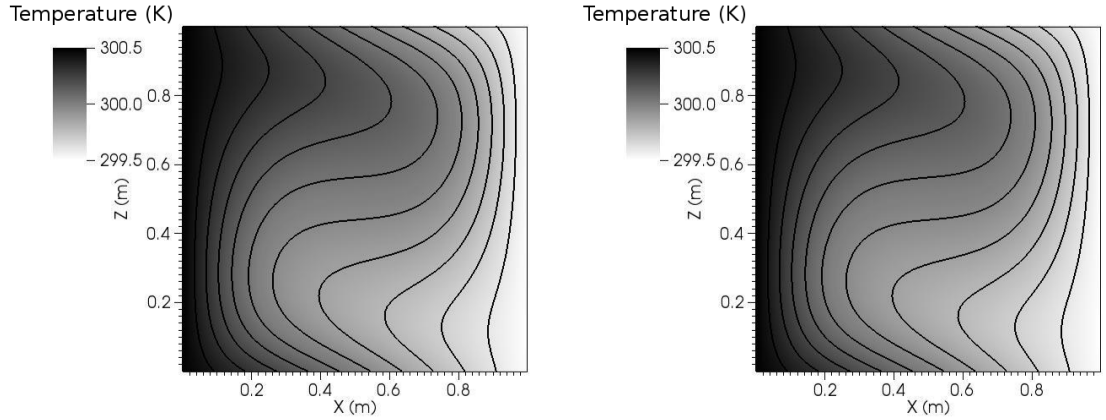

Figure 5.22: Temperature in central xz-plane for $Ra = 10^4$ with OB (left) and NOB (right)

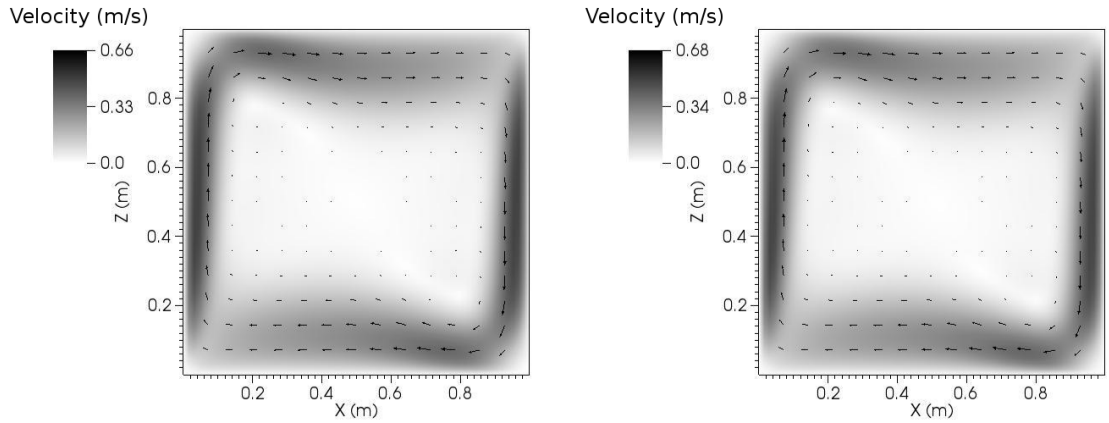

Figure 5.23: Velocity in central xz-plane for $Ra = 10^6$ with OB (left) and NOB (right)

Based on the previous numerical results presented considering $Ra = 10^4$, the simulations using OB and NOB were qualitatively very similar. Therefore, no differences were observed in the results from OB and NOB for the laminar regime. Transition to turbulent flow takes place at approximately $Ra = 10^6$ (MARKATOS; PERICLEOUS, 1984); therefore, when increasing the Rayleigh number to 10^6, the flow is no longer laminar and three dimensional effects become significant. The instantaneous velocity magnitude in grayscale and the velocity vectors are shown in Fig. 5.23 using OB and NOB for $Ra = 10^6$ simulations.

Small differences between OB and NOB were noticed in the velocity field in Fig. 5.23. The maximum velocity from the simulation using OB was a somewhat lower than the simulation using NOB. The velocity vectors from OB and NOB presented similar directions and magnitudes. Figure 5.23 shows the magnitude of the velocity tending to become comparatively small (brighter areas) away from the walls, and virtually zero over the cavity center. Areas with mixture potential are now less pronounced than for $Ra = 10^4$, since they are confined to the areas close to the

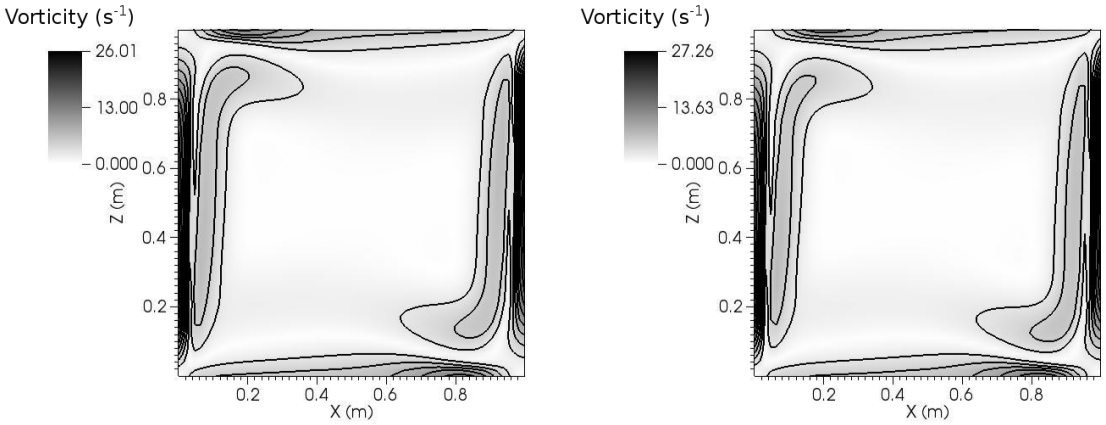

Figure 5.24: Vorticity in central xz-plane for $Ra = 10^6$ with OB (left) and NOB (right)

walls. The flow is severely concentrated near the walls (darker areas) and, clearly, the velocity component in the z-direction is higher than the x-component. Velocity vectors close to walls have a clockwise circulation, although there is no preferential direction in the cavity center.

Figure 5.24 illustrates the instantaneous magnitude of the vorticity in grayscale and the vorticity isovalue lines for $Ra = 10^6$ using OB and NOB. A slight difference between OB and NOB was noticed in the vorticity field in Fig. 5.24. The maximum value of the vorticity was higher for the simulation using NOB than for OB. The occurrence of higher velocities in the NOB simulations may have promoted higher velocity gradients, enhancing the vorticity. Figure 5.24 exhibits higher magnitudes of the vorticity next to the walls than in the cavity center, especially close to the west and east walls. The shear stresses next to the top and bottom walls are less significant than those next to the west and east walls, due to the high velocities in the z-direction, as shown in Fig. 5.24. The vorticity is negligible at the center of the cavity.

Figure 5.25 shows the instantaneous temperature in grayscale and the isotherms for $Ra = 10^6$ with OB and NOB. According to Fig. 5.25, no qualitative differences between OB and NOB were noticed in the temperature field or the isotherms. Figure 5.25 illustrates that the heat transfer is mainly by advection in the moving fluid near the walls. The thermal boundary layer become thinner when compared to $Ra = 10^4$ (shown in Fig. 5.22). On the other hand, away from the walls, the fluid remains almost isothermic because the diffusion process is less effective due to the lack of turbulence in regions far from the walls. In the central region, thermal stratification prevents any vertical motion, as described by Markatos e Pericleous (1984). Turbulent mixing is reduced in stable stratification because buoyancy enhances turbulence only

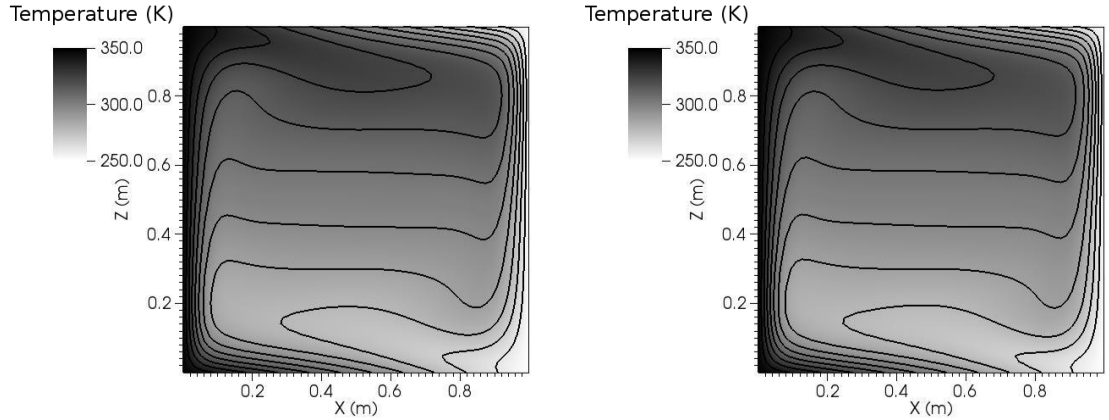

Figure 5.25: Temperature in central xz-plane for $Ra = 10^6$ with OB (left) and NOB (right)

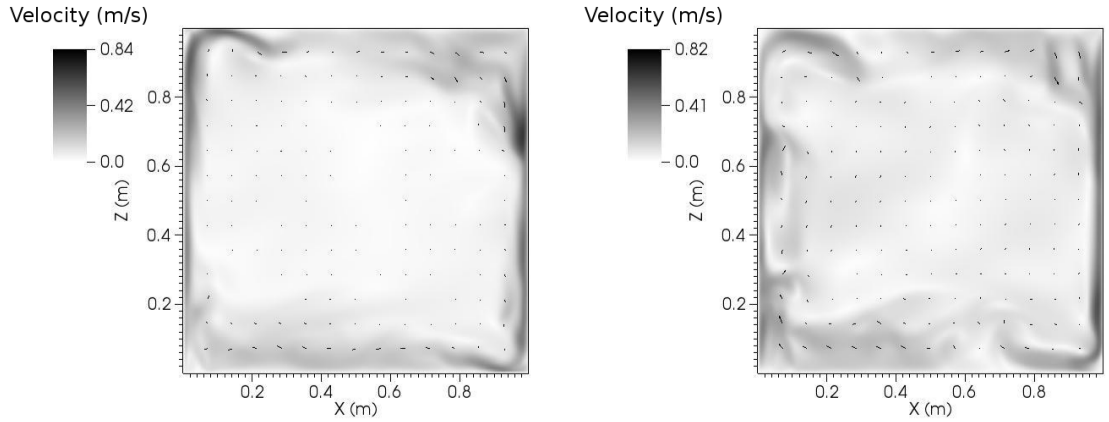

Figure 5.26: Velocity in central xz-plane for $Ra = 10^8$ with OB (left) and NOB (right)

in unstable stratification. Therefore, one may observe that the influence of the temperature on the flow characteristics is remarkable in this particular condition.

Increasing the Rayleigh number to 10^8, the turbulent regime is developed. Three-dimensional effects become evident and the flow is now completely non-uniform; therefore, it is expected that differences between OB and NOB become more evident since the variations of specific mass are more intensified than in the previous simulations with lower Rayleigh numbers. Figure 5.26 shows the instantaneous velocity magnitude in grayscale and velocity vectors for $Ra = 10^8$ using OB and NOB.

Small differences between OB and NOB in the velocity field are noticeable in Fig. 5.26. The maximum velocity from the simulations using OB were higher than NOB. The differences between the velocity field shown in Fig. 5.26 represents evidence that the flow evolution in time for each formulation was different. Figure 5.26 presents high velocity magnitude alongside the walls, particularly in the west and top walls' corners as well as in the east and bottom walls' corner

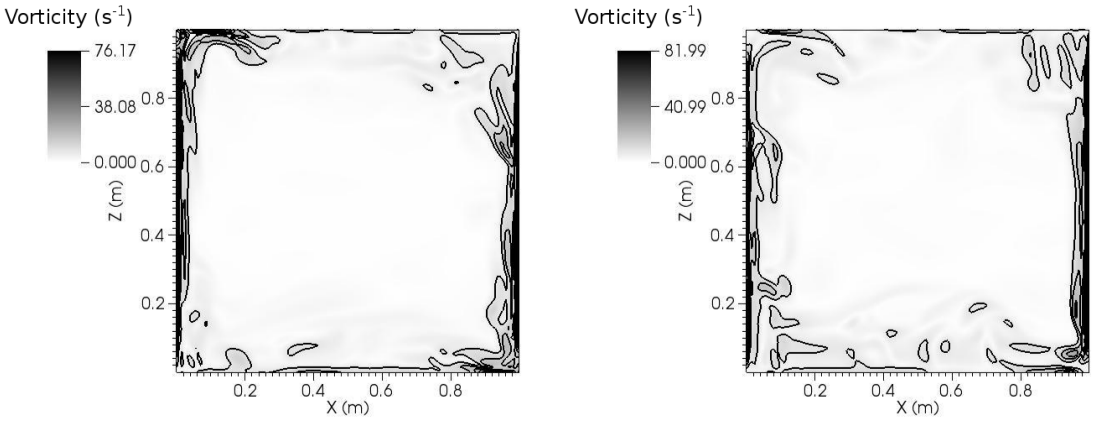

Figure 5.27: Vorticity in central xz-plane for $Ra = 10^8$ with OB (left) and NOB (right)

for the $Ra = 10^8$ simulations. The viscous boundary layer is thinner than it was for $Ra = 10^6$ and the velocity vectors at the cavity center do not follow a preferential direction. As the Rayleigh number increases, the temperature and velocity boundary layers become thinner, as previously seen in Wang, Zhang e Guo (2017). It is possible to identify a counterclockwise vortex close to the cavity center in Fig. 5.26.

Figure 5.27 shows the instantaneous vorticity magnitude in grayscale and vorticity isovalue lines for $Ra = 10^8$ using OB and NOB. Small differences between OB and NOB can be seen in the vorticity field in Fig. 5.27. The maximum value of the vorticity for the simulation using NOB was higher than OB. In addition, the lines of vorticity isovalues for OB and NOB presented small differences next to the walls in the central xz-plane. The magnitude of the vorticity was higher for the simulation with NOB due to the existence of higher velocity gradients close to the east and west walls. Figure 5.27 illustrates that the vorticity is even more concentrated at the walls than it was for $Ra = 10^6$ (shown in Fig. 5.24). The maximum values of the vorticity (darker areas) were next to the west and east walls. In addition, the regions close to the top and bottom walls presented medium values of vorticity. Other regions showed no significant vorticity.

Figure 5.28 exhibits the instantaneous temperature in grayscale and the isotherms for $Ra = 10^8$ using OB and NOB. Small differences between OB and NOB can be observed in the temperature field seen in Fig. 5.28. The evolution of the temperature field in time is clearly different in OB than in NOB, since the velocity field also changes differently in time for OB than for NOB. The isotherms of OB and NOB are qualitatively similar, however temporal effects specific to each approach are seen in Fig. 5.28. Figure 5.28 indicates that the thermal boundary

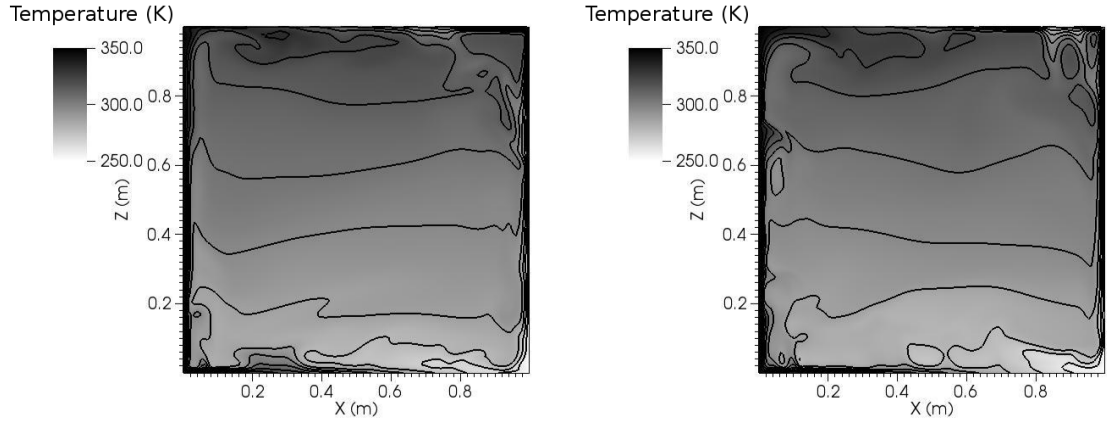

Figure 5.28: Temperature in central xz-plane for $Ra = 10^8$ with OB (left) and NOB (right)

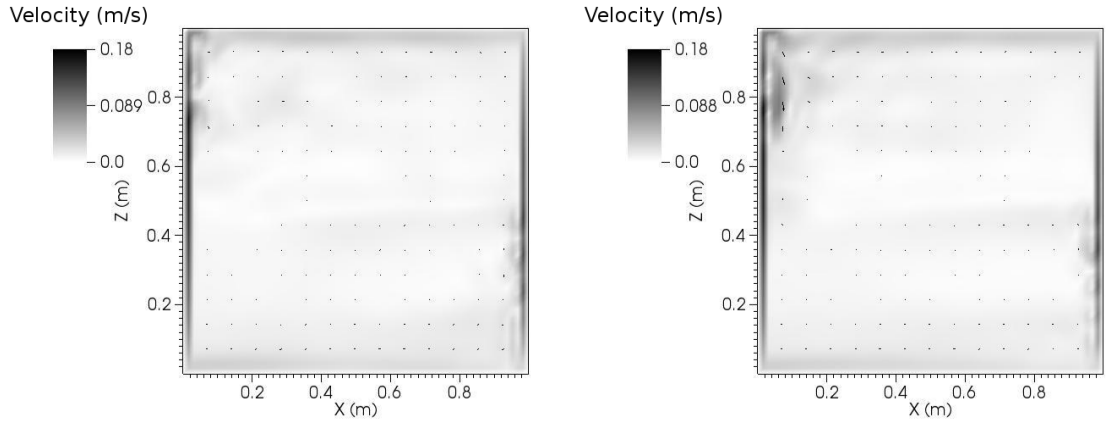

Figure 5.29: Velocity in central xz-plane for $Ra = 10^{10}$ with OB (left) and NOB (right)

layer is even thinner than it was for $Ra = 10^6$, as shown in Fig. 5.25. The cavity center presents thermal stratification, but not so evident as it was for $Ra = 10^6$ (shown in Fig. 5.25).

Increasing the Rayleigh number to $Ra = 10^{10}$, Fig. 5.29 shows the instantaneous velocity magnitude in grayscale and the velocity vectors for $Ra = 10^{10}$ using OB and NOB. The velocity fields for OB and NOB seen in Fig. 5.29 have the same behavior as the flow field and velocity vectors. No differences were seen in the velocity field between the simulations using OB and NOB for $Ra = 10^{10}$. In addition, the maximum values of the velocity for OB and NOB were identical. According to Fig. 5.29, the velocity field had its maximum values (darker areas) alongside the west and east walls. At the other regions, the velocity magnitude was irrelevant (brighter areas). The velocity vectors had a preferential direction and presented a rotational behavior. In addition, mixture was restricted to a small area close to the walls due to the concentrated velocity.

Figure 5.30 shows the instantaneous vorticity magnitude in grayscale and the vorticity isovalues lines for $Ra = 10^{10}$ using OB and NOB. No qualitative differences between OB and

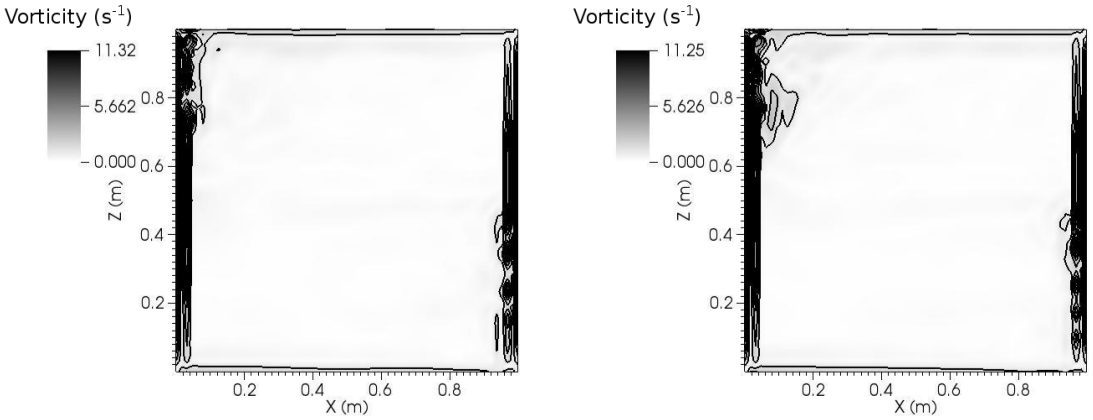

Figure 5.30: Vorticity in central xz-plane for $Ra = 10^{10}$ with OB (left) and NOB (right)

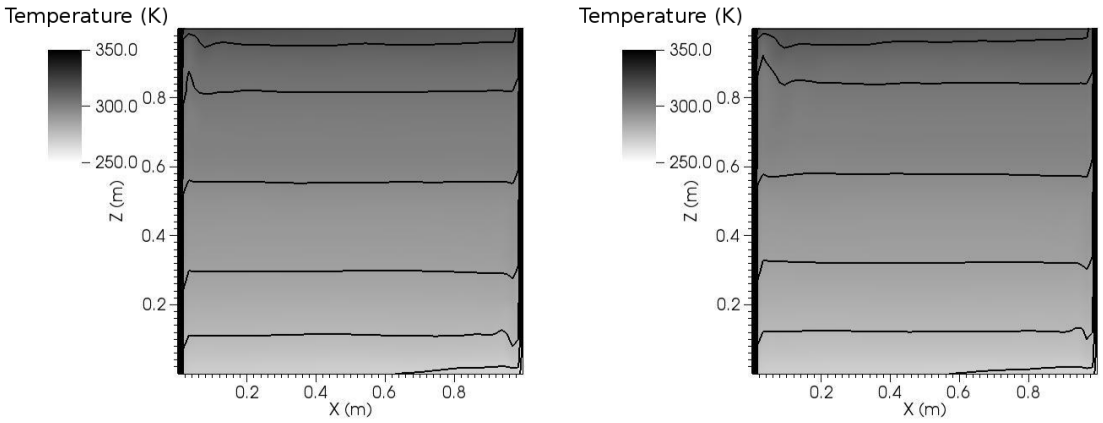

Figure 5.31: Temperature in central xz-plane for $Ra = 10^{10}$ with OB (left) and NOB (right)

NOB are to be seen in Fig. 5.30 for the vorticity field. The maximum values of the vorticity are very similar, and the lines of vorticity isovalues have the same behavior. According to Fig. 5.30, the vorticity was restricted to the proximities of the east and west walls. No significant vorticity (brighter areas) was expected at the cavity center, since the majority of shear stresses are located at the walls.

Figure 5.31 presents the instantaneous temperature in grayscale and the isotherms for $Ra = 10^{10}$ using OB and NOB. No qualitative differences between OB and NOB are seen in the temperature field in Fig. 5.31. In addition, the isotherms of OB and NOB are quite similar. It can be seen that the thermal boundary layer is now thinner than it was for $Ra = 10^{8}$ and temperature is completely stratified in the domain, except at the walls. Again, thermal stratification prevented any vertical motion, as described by Markatos e Pericleous (1984). The behavior of the isotherms was similar to that found by Wang, Zhang e Guo (2017), where thermal stratification reduced the areas with mixture potential.

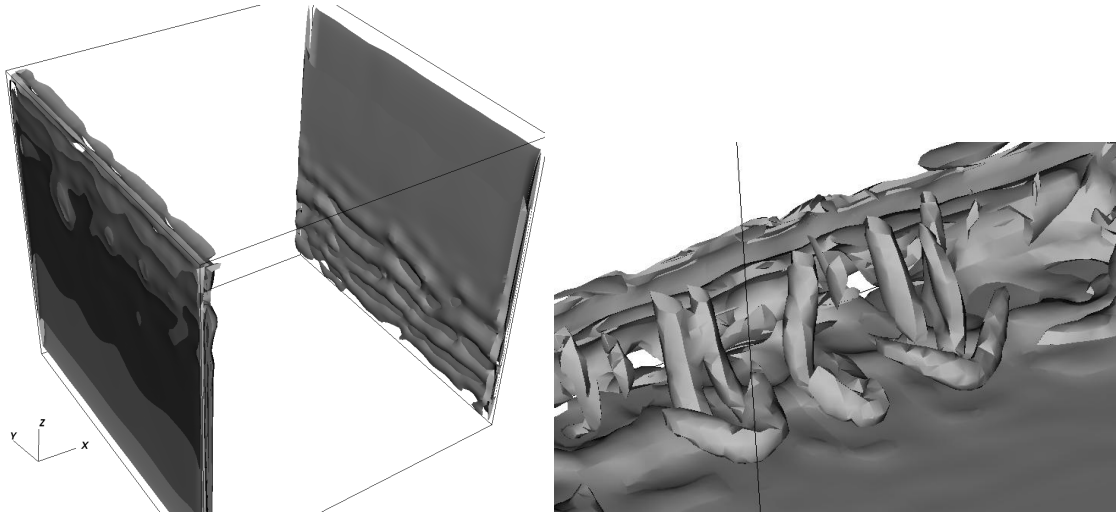

Figure 5.32: Tollmien–Schlichting instabilities (left) and hairpin instabilities (right)

Although the study of high Rayleigh numbers is usually limited to 2D configurations in the literature (WANG; ZHANG; GUO, 2017), there is a need to model three-dimensional effects of the flows, since turbulence only occurs in 3D configurations. In the research presented here, turbulent coherent structures were identified close to the walls using vorticity isovalues for $Ra = 10^{10}$. First, fine filaments developed close to the east and west walls. These filaments are shown in Fig. 5.32 (left) and may be identified as Tollmien–Schlichting waves. Later, hairpin structures appeared next to these filaments, which are also visible in Fig. 5.32 (right).

Tollmien–Schlichting waves are typically found in boundary layer flow transitions. In initial stage of the transition, small disturbances transform a stable laminar flow into an unstable, but still laminar flow which takes the form of a two-dimensional Tollmien–Schlichting wave. These waves may be slowly amplified and they may eventually grow nonlinearly until the flow transitions to the turbulent regime. These waves were originally identified by Tollmien and Schlichting, for whom the phenomenon is named. At the walls, the initial instability that may occur is the two-dimensional Tollmien–Schlichting waves, travelling in the mean flow direction. Tollmien–Schlichting waves undergo linear amplification and non-linear interactions, which eventually lead to turbulence (MANUILOVICH, 1994; LESIEUR, 2008). Wang, Zhang e Guo (2017) studied the natural convection flow in a differentially heated cubical cavity in 3D simulations considering $Ra = 10^{10}$. However, they have not reported the visualization of Tollmien–Schlichting waves.

In order to present a quantitative analysis for the range of Rayleigh numbers tested, the mean Nusselt number was evaluated at the east wall. Experimental data available in the literature

Table 5.9: Mean Nusselt number at the east wall and difference between the computed values and literature.

	$Ra = 10^4$		$Ra = 10^6$		$Ra = 10^8$		$Ra = 10^{10}$	
	Nu	diff. (%)	Nu	diff. (%)	Nu	diff. (%)	Nu	diff. (%)
Experimental data	1.521	-	6.389	-	26.830	-	92.641	-
Present work - OB	1.555	2.24	6.559	2.66	25.411	-5.29	88.850	-4.09
Present work - NOB	1.554	2.24	6.505	1.82	26.342	-1.82	92.210	-0.47

and the mean Nusselt number computed at the east wall are presented in Table 5.9. Numerical results for Rayleigh numbers up to $Ra = 10^8$ were compared to the experimental data available in Leong, Hollands e Brunger (1999), and results for $Ra = 10^{10}$ were compared to an experimental correlation available in Cowan, Lovegrove e Quarini (1982). The difference between the numerical results and the literature were calculated and are also presented in Table 5.9 for NOB and OB.

NOB and OB accurately predicted the heat transfer from the laminar to turbulent regime, as shown in Table 5.9. Nonetheless, as the Rayleigh number increases, OB presented larger differences than the NOB from the literature. NOB predicted an adequate thermal transfer rate compared to the experimental results for all the cases simulated, confirming the NOB's potential to model flows with variable specific mass due to temperature field variations.

The mean Nusselt numbers computed in the simulations using OB and NOB were similar for $Ra = 10^4$ and $Ra = 10^6$. On the other hand, the mean Nusselt number computed with NOB was approximately 4.0% higher than that obtained with OB for $Ra = 10^8$ and $Ra = 10^{10}$. Montiel-Gonzalez *et al.* (2015) also found numerical results using an approach with variable properties with approximately 4% of error lower than OB, however their work investigated natural convection in the laminar regime. In addition, Wang, Zhang e Guo (2017), who used OB, found a mean thermal transfer rate similar to that from the OB results of the present paper for the simulation with $Ra = 10^{10}$. Therefore, simulations using NOB provided more accurate results for the heat transfer rate compared to OB. The consequences of modeling variable specific mass in all the terms of the momentum and energy equations revealed numerical results with higher accuracy with NOB in comparison to OB, where only the combined gravity–buoyancy term accounted for the effects of specific mass variations due to the temperature field.

The velocity field was investigated in OB and NOB simulations in order to evaluate quantitatively its differences. The minimum and maximum velocity components from the simulations

Table 5.10: Minimum and maximum u, v and w velocity components.

	$Ra = 10^4$		$Ra = 10^6$		$Ra = 10^8$		$Ra = 10^{10}$	
	OB	NOB	OB	NOB	OB	NOB	OB	NOB
u_{min}	-0.0453	-0.0453	-0.4482	-0.4697	-0.5132	-0.4914	-0.0367	-0.0417
u_{max}	0.0453	0.0452	0.4482	0.4294	0.4665	0.4078	0.0746	0.0686
v_{min}	-0.0071	-0.0071	-0.1733	-0.1903	-0.2952	-0.3106	-0.0424	-0.0419
v_{max}	0.0071	0.0071	0.1733	0.1903	0.3727	0.3148	0.0485	0.0609
w_{min}	-0.0478	-0.0478	-0.6584	-0.6446	-0.8017	-0.8154	-0.1456	-0.1509
w_{max}	0.0478	0.0478	0.6584	0.6446	0.7835	0.7719	0.1768	0.1800

using NOB and OB are presented in Table 5.10.

The u, v and w velocity components in Table 5.10 are, in general, similar for the simulations using OB and NOB. However, a few significant differences can be observed, especially for high Rayleigh numbers, when the differences in the velocity components of OB and NOB varied by up to 20%. The data from Table 5.10 shows no significant velocity variations in the simulation in the laminar regime ($Ra = 10^4$) between OB and NOB, although small differences can be observed in the simulations in the turbulent regime ($Ra = 10^6$ to $Ra = 10^{10}$). The differences between OB and NOB in the velocity field in the turbulent regime are evidence of the noticeable contrast between the two approaches in terms of the evolution of the flow over time. In addition, the differences between OB and NOB in their velocity fields were progressively higher as the Rayleigh number increased, since the turbulence was enhanced and the effects of a variable specific mass were intensified. The proposed NOB method shows that some significant flow effects are captured when specific mass variations are considered in all the terms of the momentum and energy equations than they are in the OB method, where only the combined gravity–buoyancy term models the specific mass variations.

Finally, three velocity profiles were investigated in the simulations using OB and NOB in order to examine the local variations of each velocity component for the range of Rayleigh numbers tested. The instantaneous u, v and w velocity components were investigated along the line segments AB, CD and EF, respectively, which are shown in Fig. 5.33. The u velocity component was evaluated along the line segment AB, the v velocity component along the line segment CD, and EF was used for the assesment of the w velocity component.

Figure 5.34 shows the instantaneous u velocity component along the line segment AB for the entire range of Rayleigh numbers tested. According to Fig. 5.34, the u velocity component

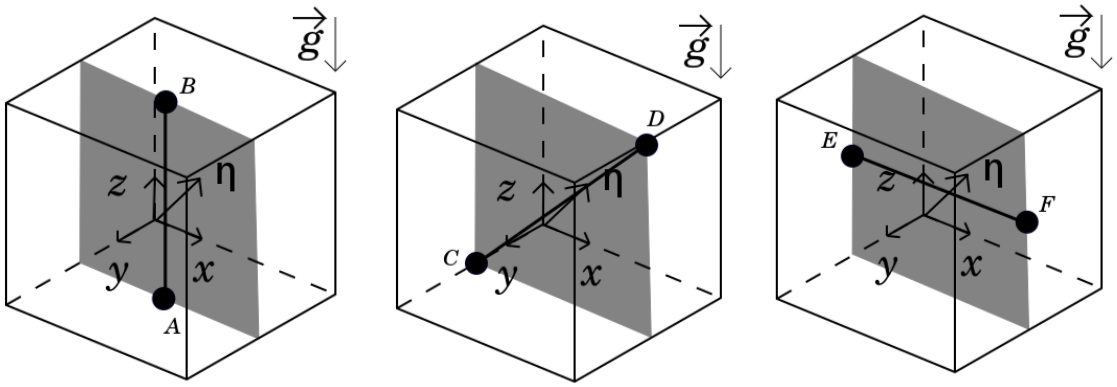

Figure 5.33: Line segments used to evaluate the u, v and w velocity components

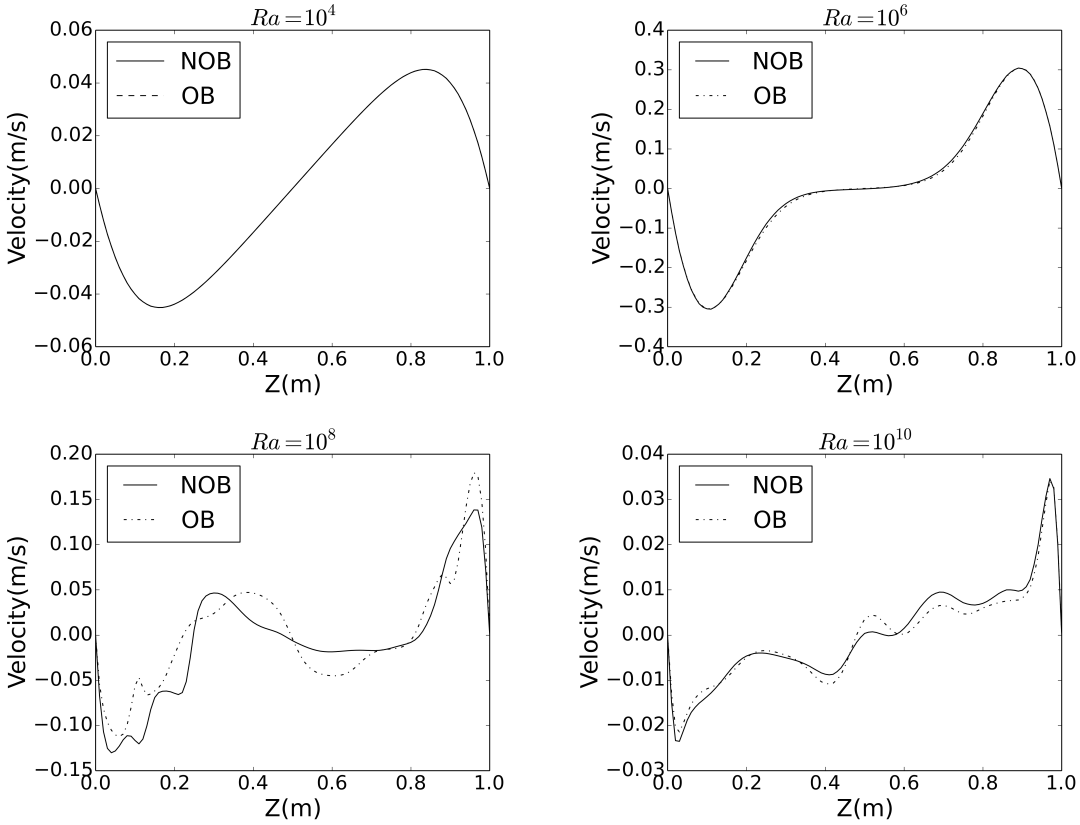

Figure 5.34: u velocity component for the line segment AB in the central xz-plane with OB and NOB for $Ra = 10^4$ (upper left), $Ra = 10^6$ (upper right), $Ra = 10^8$ (lower left) and $Ra = 10^{10}$ (lower right).

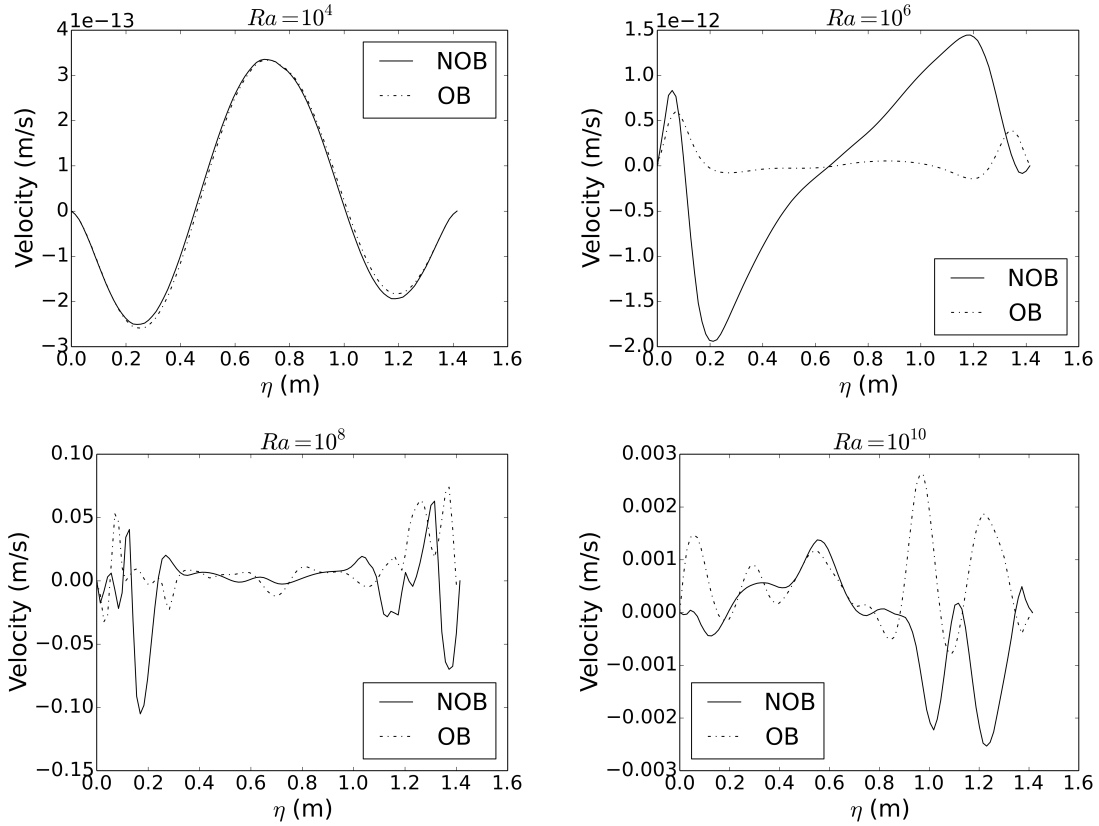

Figure 5.35: v velocity component along the line segment CD in the central xz-plane with OB and NOB for $Ra = 10^4$ (upper left), $Ra = 10^6$ (upper right), $Ra = 10^8$ (lower left) and $Ra = 10^{10}$ (lower right).

was not significantly different for the OB and NOB simulations. Differences in the u velocity component were more pronounced for the Rayleigh numbers of 10^8 and 10^{10} since the effects of the specific mass variations increased as the Rayleigh number increased.

Figure 5.35 shows the instantaneous v velocity component along the line segment CD for the entire range of Rayleigh numbers tested. According to Fig. 5.35, the differences between OB and NOB are appreciable for the v velocity component. The three-dimensional effects of the flow were more pronounced for high Rayleigh numbers since the magnitude from the v velocity component was only visibly observed for $Ra = 10^8$ and $Ra = 10^{10}$.

Figure 5.36 shows the instantaneous w velocity component along the line segment EF for the entire range of Rayleigh numbers tested. Figure 5.36 shows the small differences between OB and NOB in the w velocity component for the simulations using high Rayleigh numbers. Only the simulations with Rayleigh numbers of 10^8 and 10^{10} present visible variations in the w velocity component for OB and NOB. In addition, the w velocity component exhibited the same profile

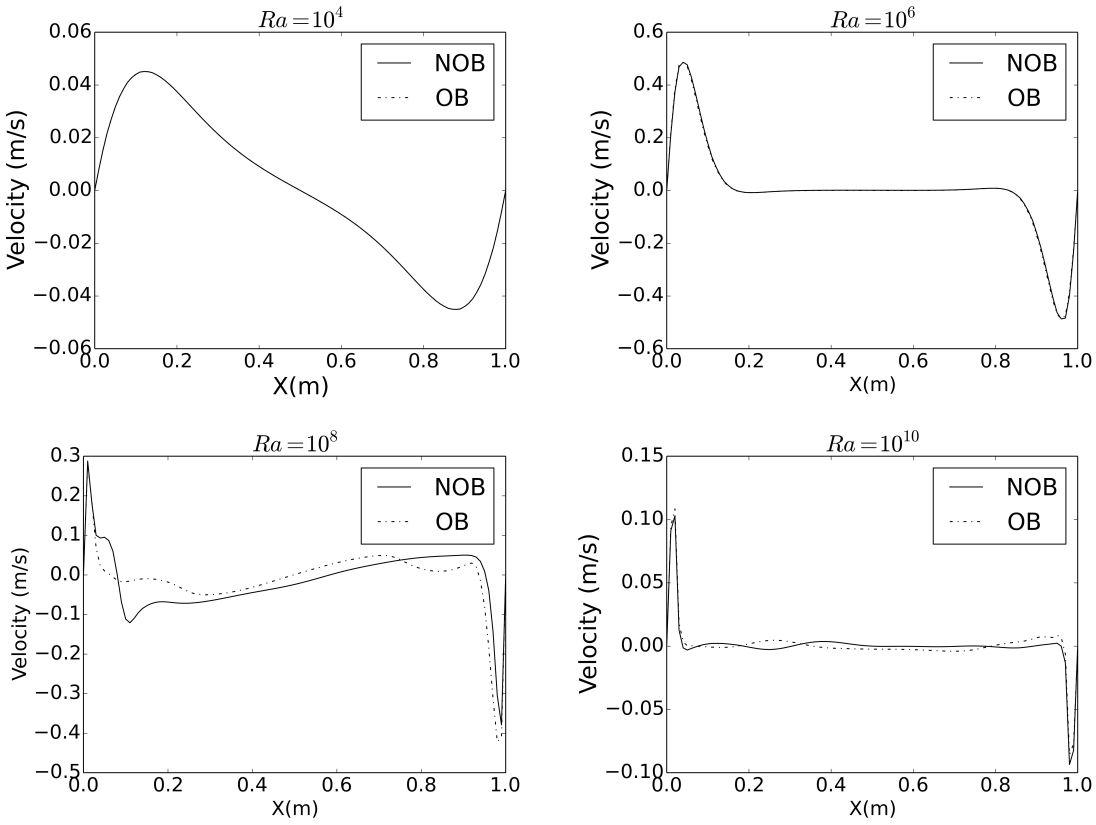

Figure 5.36: w velocity component along the line segment EF in the central xz-plane with OB and NOB for $Ra = 10^4$ (upper left), $Ra = 10^6$ (upper right), $Ra = 10^8$ (lower left) and $Ra = 10^{10}$ (lower right).

for both approaches in the simulations of $Ra = 10^4$ and $Ra = 10^6$.

According to Figs. 5.34, 5.35 and 5.36, each velocity component presented small variations for the Rayleigh numbers of 10^8 and 10^{10}, which were the simulations where the differences in heat transfer rates computed from NOB were more accurate than those obtained from OB (seen in Table 5.9). In addition, the velocity field variations between OB and NOB, observed in Table 5.10, also revealed significant differences in the velocity fields for the simulations with the Rayleigh numbers of 10^8 and 10^{10}. Enhancing the ability to capture the changes of the specific mass variations in the flows, NOB provided relevant effects in the velocity fields; for that reason, NOB presents an extension of OB allowing tackling a wider range of incompressible problems with higher gradients of specific mass in the domain than does OB. Therefore, the mathematical formulation proposed in the NOB method improves the quality of the calculations of the thermal transfer rate compared to OB by increasing the effects of a variable specific mass in the momentum and energy equations, and is suggested for application to single-phase. In addition, NOB is preferable since it removes the uncertainty of constant fluid properties imposed by OB (KANG; IACCARINO; HAM, 2009).

5.4 Influence of dimensionless parameters on non-isothermal single-phase flows without phase change

In natural convection problems, the most relevant dimensionless parameters are the Grashof and Prandtl numbers, which combined results in the Rayleigh number. In the next subsections, the influence of the Grashof and Prandtl numbers are evaluated qualitatively according to the isotherms pattern and quantified using the Nusselt number calculation for single-phase flows.

5.4.1 Influence of the Grashof number on single-phase flows

Simulations were conducted considering the Prandtl number of 0.71 and a range of the Grashof number from 1.4×10^3 to 1.4×10^6.

Natural convection in single-phase flow was examined using the Oberbeck-Boussinesq approximation. Null velocities and null pressure gradient were imposed to all the domain faces. The east and west walls have, respectively, a uniform high and low temperature. The south, north,

bottom and top walls are adiabatic.

The figure 5.37 shows the isotherms from the present paper considering the Prandtl number of 0.71 and the Grashof number range from 1.4×10^3 to 1.4×10^6.

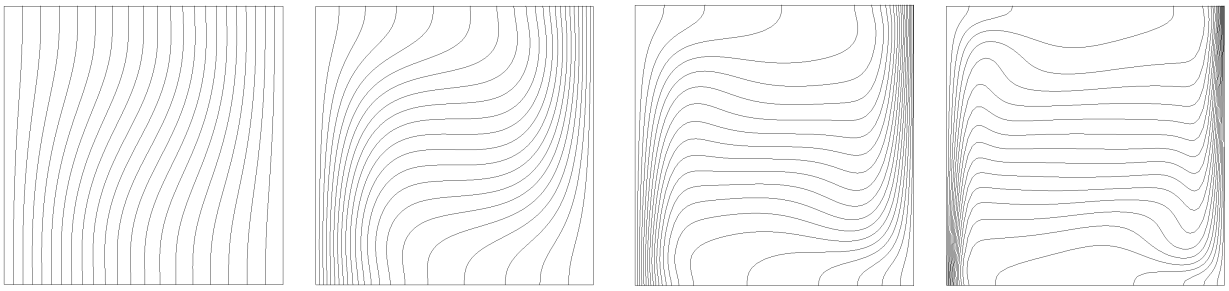

(a) (b) (c) (d)

Figure 5.37: Isotherms at central xz-plane from the present paper for $Pr = 0.71$ and Gr=1.4×10^3 (a), Gr=1.4×10^4 (b), Gr=1.4×10^5(c), Gr=1.4×10^6 (d)

According to the figure 5.37, the isotherms topology became more complex as the Grashof number increased, as previously reported by Padilla, Lourenco e Silveira-Neto (2013). The temperature field becomes more stratified in the cavity center and the rotational characteristic of flow is progressively more evident as the Grashof number increases, as previously described by Wang, Zhang e Guo (2017). In addition, the spatial mean Nusselt number computed at the east wall was progressively higher as the Grashof number increased.

Therefore, according to the results obtanied, the augmentation of the Grashof number causes the increasement of the thermal transfer rate in single-phase flows.

5.4.2 Influence of the Prandtl number on single-phase flows

Simulations were conducted considering the Grashof number of 1.4×10^3 and two values of the Prandtl number were tested, namely $Pr = 0.71$ and $Pr = 7.10$.

Natural convection in single-phase flow was examined using the Oberbeck-Boussinesq approximation. Null velocities and null pressure gradient were imposed to all the domain faces. The east and west walls have, respectively, a uniform high and low temperature. The south, north, bottom and top walls are adiabatic.

The figure 5.38 shows the temperature field and the isotherms configuration for the simulations with Grashof number and different Prandtl number.

As previously seen for the Grashof number, the Prandtl number affects the thermal transfer

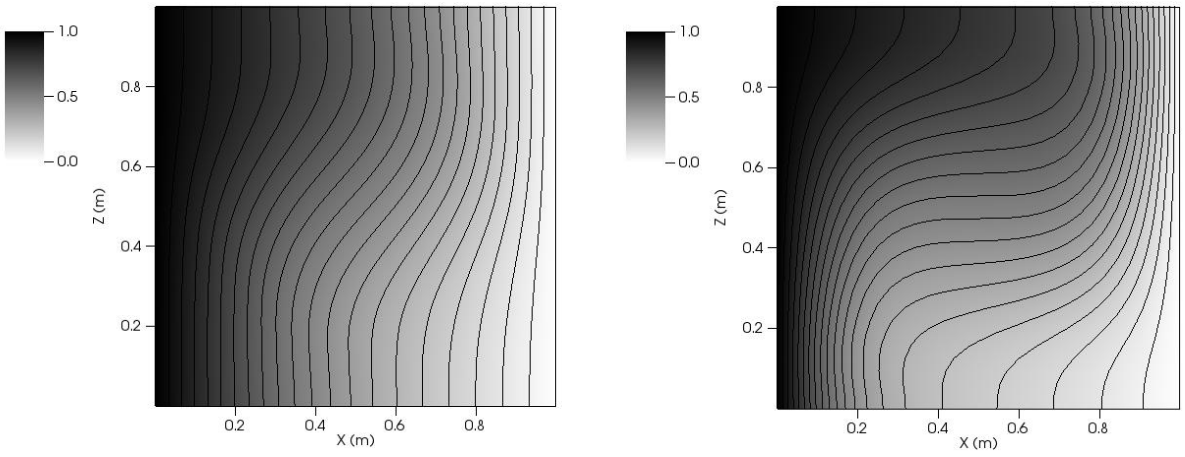

(a) (b)

Figure 5.38: Temperature field and isotherms for $Gr = 1.4 \times 10^3$ and $Pr = 0.71$ (a) as well as for $Pr = 7.1$ (b).

rate intensity. The highest thermal transfer rate was associated to the highest value of Prandtl number. The isotherms pattern was deeply modified as the Prandtl number changed from 0.71 to 7.1 since the isovalues of temperature became more horizontal compared to the bottom and top walls. In addition the spatial mean Nusselt number computed at the east wall were also increased as the Prandtl number increased.

Therefore, the Prandtl number is also responsable for afectting the thermal transfer rate as well as the isotherms pattern in single phase flows.

5.5 Influence of the Prandtl number on non-isothermal two-phase flows without phase change

In this section, analysis about the influence of the Prandtl number were performed for two-phase flows simulations. The following investigations were conducted:

1. The Prandtl number from the dispersed phase was higher than the Prandtl number from the continuos phase

2. The Prandtl number from the dispersed phase was lower than the Prandtl number from the continuos phase

3. The Prandtl number from the dispersed phase was equal to the Prandtl number from the continuos phase

The next subsections describe in details the results obtained from the computational simulations performed. The isotherms and the thermal transfer rate were considered the main parameters to the investigations conducted.

5.5.1 Simulations where the Prandtl number from the dispersed phase was higher than the Prandtl number from the continuos phase

In this section, two-phase flows are investigated in the situation where the Prandtl number from the dispersed phase was higher than the Prandtl number from the continuos phase. Three different analysis were performed in this section, namely:

- $Pr_{dis} > Pr_{con}$ and the effects of the overall Prandtl number variation was computed
- $Pr_{dis} > Pr_{con}$ and the effects of the bubble size variation was evaluated
- $Pr_{dis} > Pr_{con}$ and the effects of the bubble size and overall Prandtl number variation were simultaneously analyzed

In the subsection 5.5.1.1, two-phase flow simulations were performed with an initial bubble radius of $0.31L$ and the overall Prandtl numbers analyzed were 1.06 and 1.51. In the subsection 5.5.1.2, two-phase flows simulations were performed with overall Prandtl number of 1.06 and two bubble radius were tested, namely: $r = 0.31L$ and $r = 0.40L$. Finally, in the subsection 5.5.1.3, two-phase flow simulations were performed with overall Prandtl number of 1.51 and 2.30 considering a bubble with $r = 0.31L$ and $r = 0.39L$, respectively.

5.5.1.1 $Pr_{dis} > Pr_{con}$ and the effects of the overall Prandtl number variation was computed

Two-phase flows simulations were performed with a dispersed phase with a bubble radius of $0.31L$. The Grashof number was considered equal to Gr$=1.4 \times 10^3$ and the continuos phase presented Prandtl number of 0.71.

First, the Prandtl number from the dispersed phase was 5 times higher than the continuos phase ($Pr_{dis} = 3.55$ and $Pr_{con} = 0.71$, leading to an overall Prandtl number of 1.06). Then, a simulation was performed considering a dispersed phase with the Prandtl number 10 times higher than the continuos phase ($Pr_{dis} = 7.10$ and $Pr_{con} = 0.71$, leading to an overall Prandtl number of 1.51).

Table 5.11: Summary of the thermal transfer rate results to compute the effects of the overall Prandtl number variation.

	$\bar{Nu}_{mean}$	$\bar{Nu}_{min}$	$\bar{Nu}_{max}$
Single-phase flow with $Pr = 0.71$	1.07	1.07	1.07
Two-phase flow with $Pr_{ove} = 1.06$	1.16	0.97	1.44
Two-phase flow with $Pr_{ove} = 1.51$	1.23	0.95	1.67

The figure 5.39 shows the temperature field and the isotherms configuration in the single phase flow with Gr=1.4×10^3 and $Pr = 0.71$ (a) and two-phase flow cases with Gr=1.4×10^3 and $Pr_{ove} = 1.06$ (b) and $Pr_{ove} = 1.51$ (c).

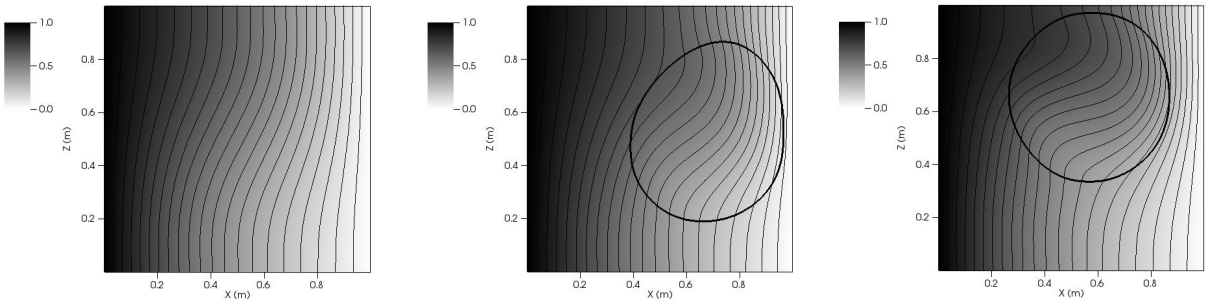

(a) (b) (c)

Figure 5.39: Temperature field and isotherms at central xz-plane considering Gr=1.4×10^3 and $Pr = 0.71$ (a), $Pr_{ove} = 1.06$ (b) and $Pr_{ove} = 1.51$ (c). The isotherms are represented in 20 thin isovalue contours, the thick contour represents the interface position and temperature field is presented in grayscale.

According to the figure 5.39, the isotherms configuration was deeply modified in comparison to the isotherms from the single-phase case. The isotherms in the figure 5.39 were not primarily vertical since the isotherms were more horizontal inside the dispersed phase.

Figure 5.40 shows the spatial mean Nusselt number evolution in time for the single-phase case ($Pr = 0.71$), the two-phase flow case with $Pr_{ove} = 1.06$ and the two-phase case with $Pr_{ove} = 1.51$. The figure 5.40 indicates the severe influence of the overall Prandtl number on the spatial mean thermal transfer rate. As the overall Prandtl number increases, the spatial mean Nusselt number increases. In comparison to the single-phase case, the two-phase cases demonstrated a relevant increasement on the mean thermal transfer rate due to the variation of the overall Prandtl number.

Table 5.11 summarizes the data related to the simulations performed in this subsection.

According to the table 5.11, the spatial mean Nusselt number increased as the overall

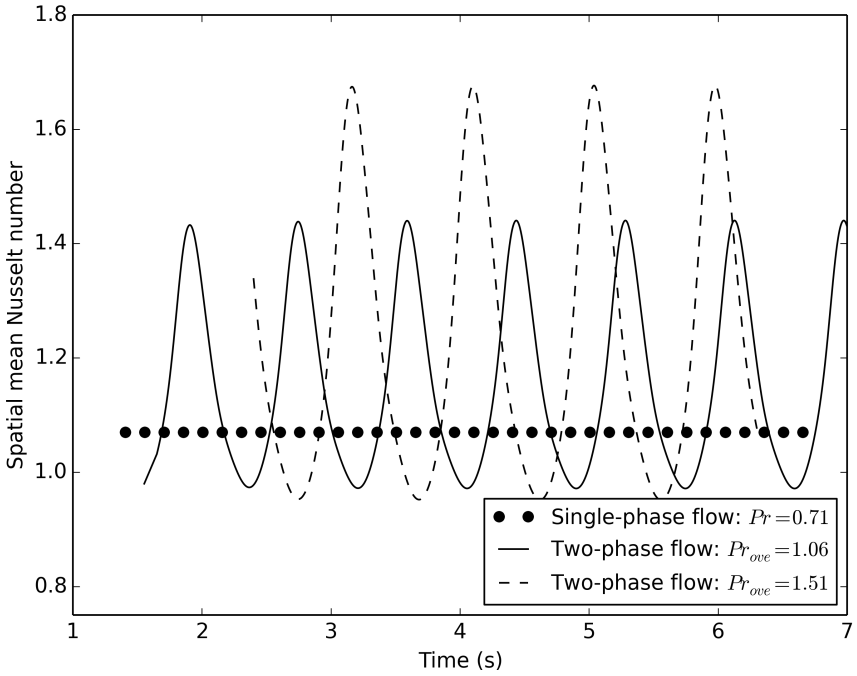

Figure 5.40: Spatial mean Nusselt number evolution in time for the single-phase case ($Pr = 0.71$) and two-phase flows cases with $Pr_{ove} = 1.06$ and $Pr_{ove} = 1.51$.

Prandtl number was increased. The minimum values of the thermal transfer rate ($\bar{Nu}_{min}$ seen in the table 5.11) were associated to the moment when the dispersed phase was the farest from the east wall. In addition, the maximum values of the thermal transfer rate ($\bar{Nu}_{max}$ seen in the table 5.11) were related to the moment when the dispersed phase was the nearest from the east wall. Therefore, the proximity of the dispersed phase from the east wall was a relevant factor impacting on the Nusselt number calculations in the situation where $Pr_{dis} > Pr_{con}$; however, none influence was observed in the situation of $Pr_{dis} > Pr_{con}$ (seen in the section 6).

5.5.1.2 $Pr_{dis} > Pr_{con}$ and the effects of the bubble size variation was evaluated

Two-phase flows simulations were performed with a dispersed phase with a bubble radius of $0.31L$ and $0.40L$. The Grashof number was considered equal to Gr=1.4×10^3 and the continuos phase presented Prandtl number of 0.71. The overall Prandtl number was 1.06 for both the simulations ($r = 0.31L$ and $r = 0.40L$).

The figure 5.41 shows the temperature field and the isotherms configuration in the single-phase case with Gr=1.4×10^3 and $Pr = 0.71$ (a) and the two-phase flow cases with Gr=1.4×10^3 and $Pr_{ove} = 1.06$ with $r = 0.31L$ (b) and $r = 0.4L$ (c).

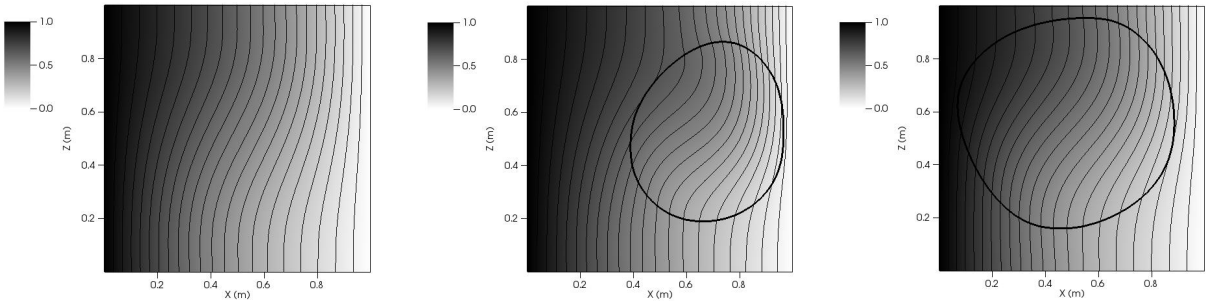

(a) (b) (c)

Figure 5.41: Temperature field and isotherms at central xz-plane considering the single-phase case with Gr=1.4×10^3 and $Pr = 0.71$ (a) and the two-phase flow cases with Gr=1.4×10^3 and $Pr_{ove} = 1.06$ with $r = 0.31L$ (b) and $r = 0.4L$ (c) The isotherms are represented in 20 thin isovalue contours, the thick contour represents the interface position and temperature field is presented in grayscale.

The figure 5.42 shows the spatial mean Nusselt number evolution in time for the single-phase case ($Pr = 0.71$), two-phase flow with $r = 0.31L$ ($Pr_{ove} = 1.06$) and two-phase flow with $r = 0.39L$ ($Pr_{ove} = 1.06$).

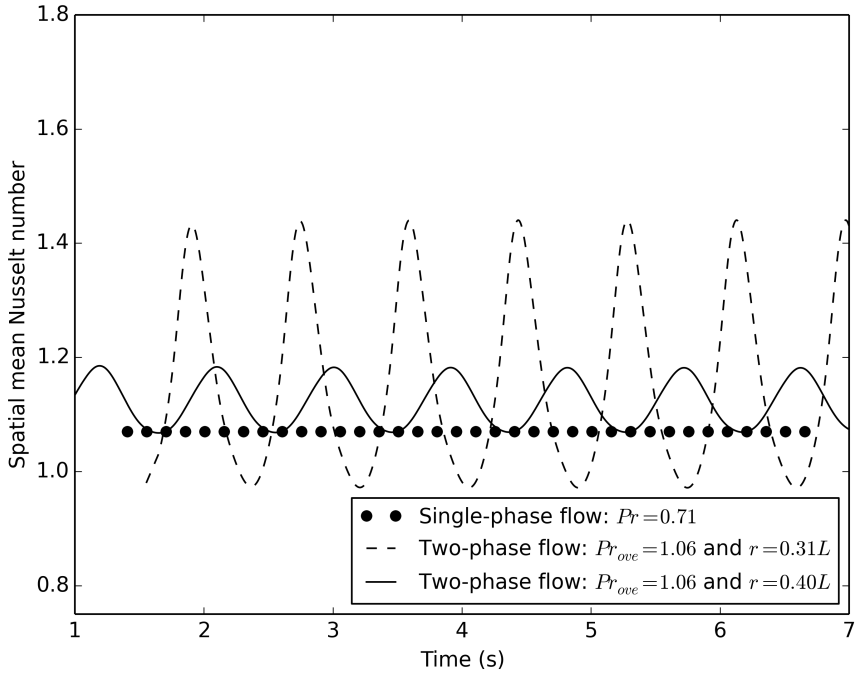

Figure 5.42: Spatial mean Nusselt number evolution for the single-phase case ($Pr = 0.71$), two-phase flow with $r = 0.31L$ ($Pr_{ove} = 1.06$) and two-phase flow with $r = 0.40L$ ($Pr_{ove} = 1.06$)

According to the figure 5.42, the spatial mean Nusselt number varied in time for both cases ($r = 0.31L$ and $r = 0.40L$). The variations of the spatial mean Nusselt number were more

Table 5.12: Summary of the thermal transfer rate results to compute the effects of the bubble size variation.

	$\bar{N}u_{mean}$	$\bar{N}u_{min}$	$\bar{N}u_{max}$
Two-phase flow with $r = 0.31L$	1.16	0.97	1.44
Two-phase flow with $r = 0.40L$	1.12	1.07	1.18

proeminent in the case for the bubble radius of $0.31L$ compared to the case with $r = 0.40L$.

The table 5.12 summarizes the data related to the simulations performed in this subsection.

According to the table 5.12, the bubble radius directly affected the thermal transfer rate in time. The smaller bubble radius was associated to the higher maximum and mean value of thermal transfer rate compared to the case with larger bubble radius. According to visual observations during the simulation time, the proximity between the wall and the bubbles was higher for the case with $r = 0.31L$ in comparison to $r = 0.40L$. Therefore, the size of the bubble radius brought consequences to the bubble moviment inside the cavity and probably the distance effect may promoted the difference in the Nusselt number calculations.

5.5.1.3 $Pr_{dis} > Pr_{con}$ and the effects of the bubble size and overall Prandtl number variation were simultaneously analyzed

Two-phase flows simulations were performed with a dispersed phase with a bubble radius of $0.31L$ and $0.39L$ and an overall Prandtl number of 1.51 and 2.30, respectively. Here, the effect of the bubble radius size were taken into account as well as the influence of the overall Prandtl number variations.

Simulations of natural convection were performed considering $Gr = 1.4\times10^3$ and $Pr = 7.1$ for the dispersed phase and $Pr = 0.71$ for the continuos phase. The simulations were performed for two different initial bubble radius, namely $r = 0.31L$ and $r = 0.39L$. The overall Prandtl number was 0.71 for the single-phase flow, 1.51 for the two-phase flow with dispersed phase with radius of $0.31L$ and 2.30 for the simulation of two-phase flow with an spherical dispersed phase with radius of $0.39L$.

The figure 5.43 shows the temperature field and the isotherms configuration in the single-phase case with Gr=1.4×10^3 and $Pr = 0.71$(a) and the two-phase flow cases with Gr=1.4×10^3

and $Pr_{ove} = 1.51$ (b) and $Pr_{ove} = 2.30$ (c).

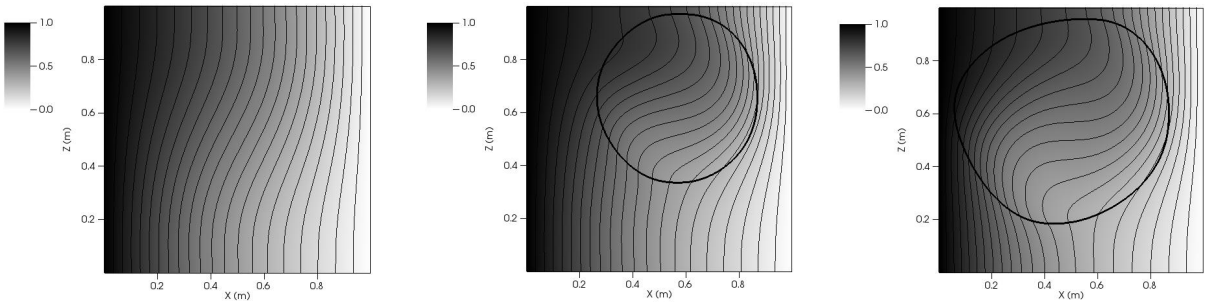

(a) (b) (c)

Figure 5.43: Temperature field and isotherms at central xz-plane for the single-phase case with Gr=1.4×10^3 and $Pr = 0.71$(a) and the two-phase flow cases with Gr=1.4×10^3 and $Pr_{ove} = 1.51$ (b) and $Pr_{ove} = 2.30$ (c). The isotherms are represented in 20 thin isovalue contours, the thick contour represents the interface position and temperature field is presented in grayscale.

The figure 5.43 illustrated the consequences of the overall Prandtl number variation on the temperature field since the isotherms behavior was modified compared to the single-phase case. As seen in the figure 5.43, inside the dispersed phase, the isotherms exhibited a deeply modified aspect since the isotherms were mainly horizontal inside the dispersed phase. In addition, the larger size of the dispersed phase in the figure 5.43(b) compared to the figure 5.43(a) intensified the impact of the Prandtl number on the temperature field. In general, the closer the dispersed phase was from the east wall, higher was the spatial mean Nusselt number at the east wall.

The figure 5.44 shows the spatial mean Nusselt number evolution in time for the single-phase case ($Pr = 0.71$), two-phase flow with $r = 0.31L$ ($Pr_{ove} = 1.51$) and two-phase flow with $r = 0.39L$ ($Pr_{ove} = 2.30$). According to the figure 5.44, the spatial mean Nusselt number was intensified as the overall Prandtl number increased. Since the enlargement of the bubble radius increases the overall Prandtl number indirectly, it was expected that the simulation with the larger bubble would yield a larger thermal transfer rate compared to the simulation with the smaller radius. According to the figure 5.44, the mean Nusselt number from the two-phase flows cases were severely altered from about -10.0% to almost $+60.0\%$ compared to the single-phase case. The thermal transfer rate was more enhanced in the simulation with radius of $0.39L$ compared to the simulation performed with radius of $0.31L$.

The table 5.13 summarizes the data related to the simulations performed in this subsection.

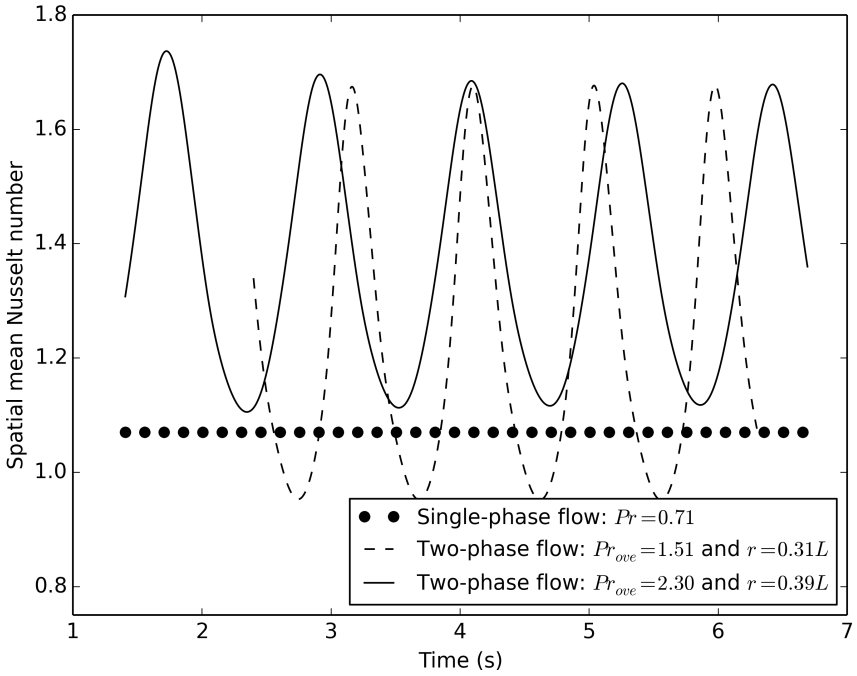

Figure 5.44: Spatial mean Nusselt number evolution for the single-phase case ($Pr = 0.71$), two-phase flow with $r = 0.31L$ ($Pr_{ove} = 1.51$) and two-phase flow with $r = 0.39L$ ($Pr_{ove} = 2.30$).

Table 5.13: Summary of the thermal transfer rate results to compute the effects of the overall Prandtl number and bubble radius variation.

	$\bar{Nu}_{mean}$	$\bar{Nu}_{min}$	$\bar{Nu}_{max}$
Single-phase flow with $Pr = 0.71$	1.07	1.07	1.07
Two-phase flow with $Pr_{ove} = 1.51$ and $r = 0.31L$	1.23	0.95	1.67
Two-phase flow with $Pr_{ove} = 2.30$ and $r = 0.39L$	1.39	1.11	1.68

The table 5.13 presented a quantitative confirmation of the influence of the Prandtl number on the thermal transfer rate according to the calculated spatial mean Nusselt number. The spatial mean Nusselt number increased almost 30 % and 15 % by the addition of the dispersed phase with an initial radius of $0.39L$ and $0.31L$, respectively. Therefore, the table 5.13 confirms that the thermal transfer rate was enhanced as the overall Prandtl number of the flow mixture increased.

The influence of the overall Prandtl number may explain the reason why the literature have been reporting the increasement of the thermal transfer rate at surfaces by the introduction of bubbles. Dabiri e Tryggvason (2015) found that the bubbles's presence rised the Nusselt number at the heated wall, specially in the case with higher Prandtl number. The present paper is in acordance with Dabiri e Tryggvason (2015) since the Prandtl number presented a great impact

in the thermal transfer mechanisms.

In the present work, the closer the dispersed phase was from the heated wall, higher was the spatial mean Nusselt number compared to the single-phase flow case. Similarly, the spatial mean Nusselt number increased in the simulations in which the distance between bubbles and the wall were lower in Dabiri e Tryggvason (2015).

Finally, as found by Dabiri e Tryggvason (2015), when the dispersed phase was in the vinicity of the heated wall, the void fraction stir up the viscous layer and reduced the size of the conduction region near the wall improving the thermal transfer rate. In addition, when the dispersed phase was far from the heated wall, its influence was not relevant and no improvement in the thermal transfer rate was observed.

5.5.2 The Prandtl number from the dispersed phase was lower than the Prandtl number from the continuos phase

Two-phase flows were investigated in the situation where the Prandtl number from the dispersed phase was lower than the Prandtl number from the continuos phase. Three different analysis were performed in this section, namely:

- $Pr_{dis} < Pr_{con}$ and the effects of the overall Prandtl number variation was computed
- $Pr_{dis} < Pr_{con}$ and the effects of the bubble size variation was evaluated
- $Pr_{dis} < Pr_{con}$ and the effects of the bubble size and overall Prandtl number variation were simultaneously analyzed

In the subsection 5.5.2.1, two-phase flow simulations were performed with an initial bubble radius of $0.31L$ and the overall Prandtl numbers analyzed were 6.3 and 6.22. in the subsection 5.5.2.2, two-phase flows simulations were performed with an overall Prandtl number of 6.22 and two bubble radius were tested, namely: $0.31L$ and $0.40L$. in the subsection 5.5.2.3, two-phase flows simulations were performed with an overall Prandtl number of 6.3 and 5.5 considering an initial bubble radius of $0.31L$ and $0.39L$, respectively.

5.5.2.1 $Pr_{dis} < Pr_{con}$ and the effects of the overall Prandtl number variation was computed

Two-phase flow simulations were performed with an initial bubble radius of 0.31L. The Grashof number was considered equal to Gr=1.4×10^4 and the continuos phase presented the Prandtl number of 7.10. First, the Prandtl number from the dispersed phase was 10 times lower than the continuos phase ($Pr_{dis} = 0.71$ and $Pr_{con} = 7.10$ leading to an overal Prandtl number of 6.30). Then, a simulation was performed considering a dispersed phase with Prandtl number 100 times lower than the continuos phase ($Pr_{dis} = 0.071$ and $Pr_{con} = 7.10$ leading to an overal Prandtl number of 6.22).

The figure 5.45 shows the temperature field and the isotherms configuration for the single-phase case with Gr=1.4×10^4 and $Pr = 7.10$ (a) and for the two-phase flow cases with Gr=1.4×10^4 and $Pr_{ove} = 6.30$ (b) and $Pr_{ove} = 6.22$ (c). The figure 5.45 shows the isotherms

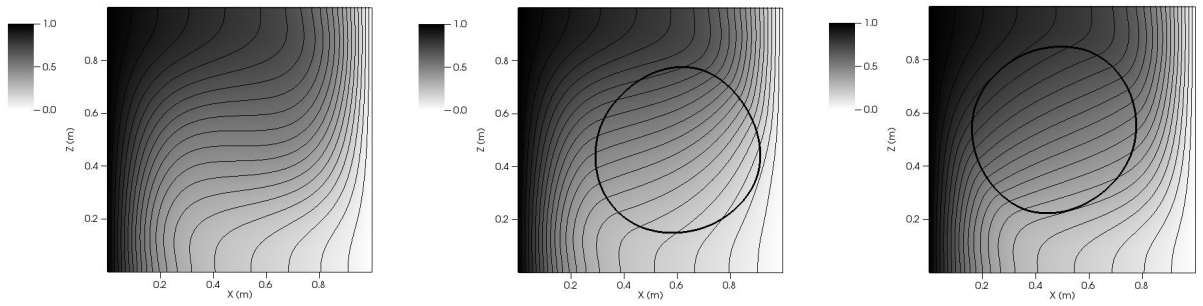

(a) (b) (c)

Figure 5.45: Temperature field and isotherms at central xz-plane for the single-phase case with Gr=1.4×10^4 and $Pr = 7.10$ (a) and for the two-phase flow cases with Gr=1.4×10^4 and $Pr_{ove} = 6.30$ (b) and $Pr_{ove} = 6.22$ (c). The isotherms are represented in 20 thin isovalue contours, the thick contour represents the interface position and temperature field is presented in grayscale.

configuration modified inside the dispersed phase. The isotherms inside the dispersed phase were more vertical than the isotherms seen in the figure for the single-phase case with $Pr = 7.1$. The tendency of the isotherms more vertical were acentuaded in the case with lower overall Prandtl number.

Figure 5.46 shows the spatial mean Nusselt number evolution in time for the single-phase case ($Pr = 7.1$), the two-phase flow cases with $Pr_{ove} = 6.3$ and $Pr_{ove} = 6.22$. According to the figure 5.46, the mean thermal transfer rate was reduced by the introduction of a bubble with lower Prandtl than the continuos phase. The case with higher overall Prandtl number was associated

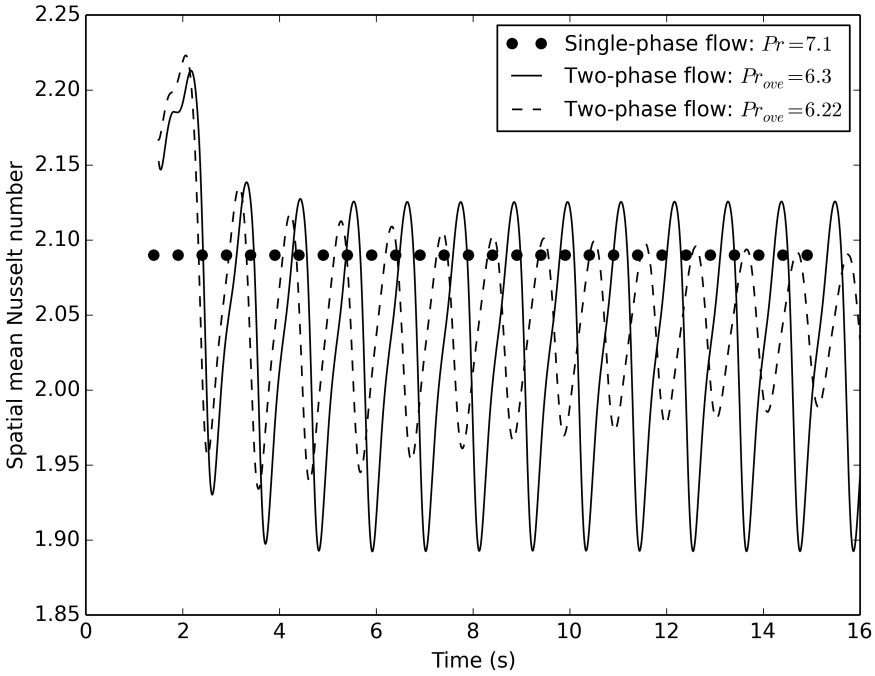

Figure 5.46: Spatial mean Nusselt number evolution for the single-phase case ($Pr = 7.1$) and two-phase flows cases with $Pr_{ove} = 6.3$ and $Pr_{ove} = 6.22$.

Table 5.14: Summary of the thermal transfer rate results to compute the effects of the overall Prandtl number variation.

	$\bar{Nu}_{mean}$	$\bar{Nu}_{min}$	$\bar{Nu}_{max}$
Single-phase flow with $Pr = 7.1$	2.09	2.09	2.09
Two-phase flow with $Pr_{ove} = 6.3$	2.03	1.89	2.12
Two-phase flow with $Pr_{ove} = 6.22$	2.03	1.98	2.09

to higher peaks of spatial mean Nusselt number in comparison to the case with a lower overall Prandtl number.

Table 5.14 summarizes the results obtanied in the present subsection.

According to the table 5.14, the reduction of the thermal transfer rate was accompannied by the reduction of the overall Prandtl number. Since the overall Prandtl numbers from the two-phase flow cases were very similar, the thermal transfer rates between them were not significantly different. However, between the single-phase and two-phase cases, the influence of the overall Prandtl number is evident on the thermal transfer rate calculated.

Table 5.15: Summary of the thermal transfer rate results to compute the effects of the bubble size variation.

	$\bar{N}u_{mean}$	$\bar{N}u_{min}$	$\bar{N}u_{max}$
Two-phase flow with $r = 0.31L$	2.03	1.98	2.09
Two-phase flow with $r = 0.40L$	1.96	1.84	2.01

5.5.2.2 $Pr_{dis} < Pr_{con}$ and the effects of the bubble size variation was evaluated

Two-phase flow simulations were performed with an initial bubble radius of $0.31L$ and $0.40L$. The Grashof number was considered equal to Gr=1.4×10^4 and the continuos phase presented Prandtl number of 7.10. The overall Prandtl number was 6.22.

The figure 5.47 shows the temperature field and the configuration for the single-phase case with Gr=1.4×10^4 and $Pr = 7.10$ (a) and for the two-phase flow cases with Gr=1.4×10^4 and $Pr_{ove} = 6.22$ with $r = 0.31L$ (b) and $Pr_{ove} = 6.22$ with $r = 0.40L$ (c).

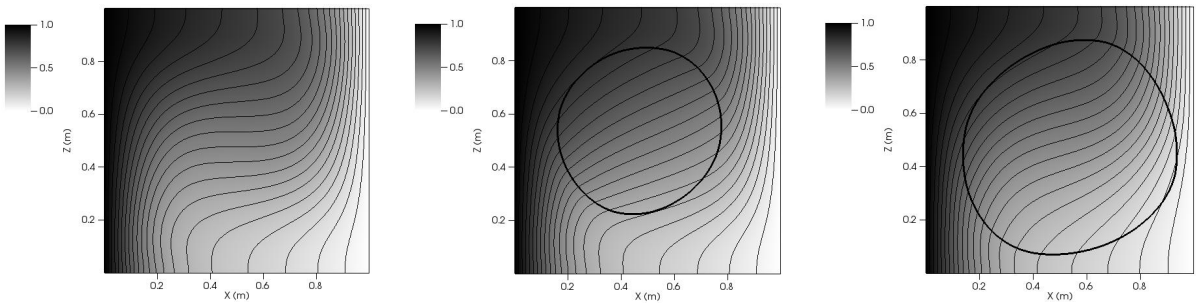

(a) (b) (c)

Figure 5.47: Temperature field and isothers at central xz-plane for the single-phase case with Gr=1.4×10^4 and $Pr = 7.10$ (a) and for the two-phase flow cases with Gr=1.4×10^4 and $Pr_{ove} = 6.22$ with $r = 0.31L$ (b) and $Pr_{ove} = 6.22$ with $r = 0.40L$ (c). The isotherms are represented in 20 thin isovalue contours, the thick contour represents the interface position and temperature field is presented in grayscale.

Figure 5.48 shows the spatial mean Nusselt number evolution in time for the single-phase case ($Pr = 7.1$), the two-phase flow cases with $r = 0.31L$ and $r = 0.40L$.

According to the figure 5.48, the spatial mean Nusselt number varied in time for both cases ($r = 0.31L$ and $r = 0.40L$). The simulation with the bubble radius of $0.40L$ presented a more visible reducement of the thermal transfer rate compared to the case with a smaller bubble radius ($r = 0.31L$).

Table 5.15 shows the main results found in this subsection.

According to the table 5.15, the bubble radius influenced the thermal transfer rate. The

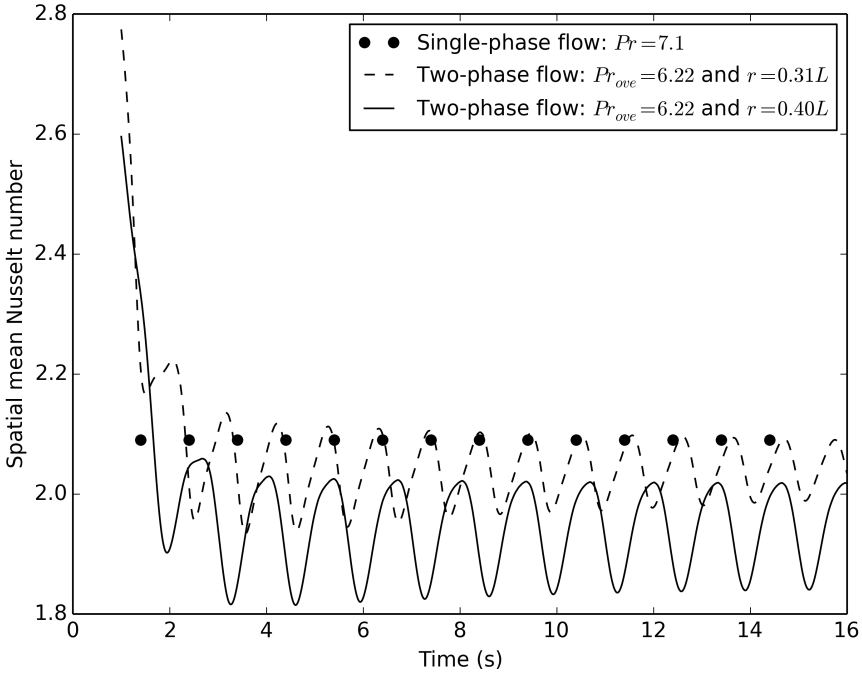

Figure 5.48: Spatial mean Nusselt number evolution for the single-phase case ($Pr = 7.1$) and two-phase flows cases with $Pr_{ove} = 6.22$ considering $r = 0.31L$ and $r = 0.40L$.

larger bubble radius presented the lower mean, minimum and maximum thermal transfer rates in time. In the visual observations during the simulations, it was confirmed that, in general, the distance between the dispersed phase and the wall was lower, affecting the Nusselt calculation, similarly seen in the previous section. therefore, the influence of the bubble radius was related to the proximity of the bubble to the wall during the bubble movimentation inside the domain.

5.5.2.3 $Pr_{dis} < Pr_{con}$ and the effects of the bubble size and overall Prandtl number variation were simultaneously analyzed

Two-phase flow simulations of natural convection were performed considering $Gr = 1.4 \times 10^4$ and a bubble initial radius of $0.31L$ and $0.39L$. The dispersed phase presented $Pr_{dis} = 0.71$ and the continuos phase $Pr_{con} = 7.1$. In addition, a simulation of single-phase flow was performed considering $Pr = 7.1$.

The overall Prandtl number of the two-phase flow simulation using an initial bubble radius of $r = 0.31L$ was 6.3 and the overall Prandtl number for the case with $r = 0.39L$ was 5.5.

Figure 5.49 shows the temperature field and the isotherms configuration for the single-phase case with Gr=1.4×10^4 and $Pr = 7.10$ (a) and for the two-phase flow cases with Gr=1.4×10^4

and $Pr_{ove} = 6.3$ with $r = 0.31L$ (b) and $Pr_{ove} = 5.5$ with $r = 0.39L$ (c).

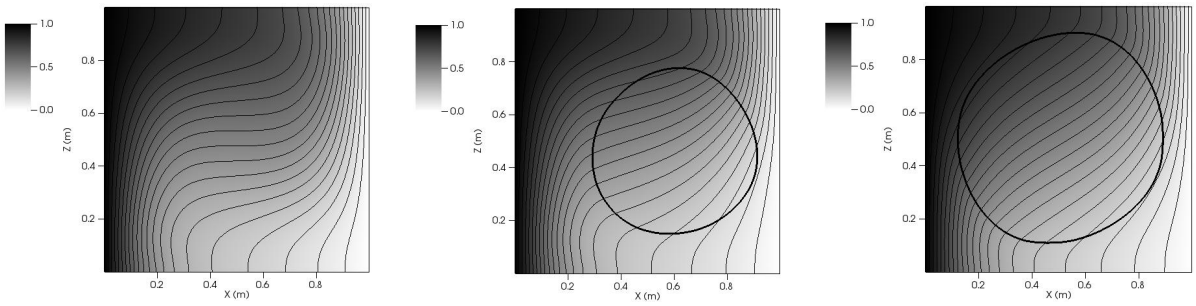

(a) (b) (c)

Figure 5.49: Temperature field and isotherms at central xz-plane for the single-phase case with Gr=1.4×10^4 and $Pr = 7.10$ (a) and for the two-phase flow cases with Gr=1.4×10^4 and $Pr_{ove} = 6.3$ with $r = 0.31L$ (b) and $Pr_{ove} = 5.5$ with $r = 0.39L$ (c). The isotherms are represented in 20 thin isovalue contours, the thick contour represents the interface position and temperature field is presented in grayscale.

According to the figure 5.49, the isotherms presented a different pattern inside the dispersed phase compared to the single-phase flow. The isotherms inside the dispersed phase in the figure 5.49 were less horizontal than the isotherms in the single-phase case, indicating the severe impact on the temperature field by the presence of the dispersed phase. The isotherms behavior inside the dispersed phase of the present paper were in accordance to Qiu, Wang e Jiang (2014) results, in which the isotherms inside the dispersed phase tended to be more vertical rather than horizontal.

The figure 5.49(c) illustrated the intensified effect previously seen in figure 5.49(b) due to the larger radius of the dispersed phase. The effect of the radius size on the thermal transfer variation was also reported by Qiu, Wang e Jiang (2014) which indicated the reduction of the mean Nusselt number as the radius of the dispersed phase was increased. Therefore, the thermal transfer rate and the overall Prandtl number of flow mixture presented a straight connection, as demonstrated in the former sections.

Figure 5.50 shows the spatial mean Nusselt number evolution in time for the single-phase case ($Pr = 7.1$), the two-phase case with $Pr_{ove} = 6.3$ and the two-phase case with $Pr_{ove} = 5.5$. According to the figure 5.50, the spatial mean Nusselt number was directly affected by the overall Prandtl number variation. The increasement of the bubble radius have intensified the importance of the Prandtl number from the dispersed phase, reducing even more the spatial mean Nusselt number.

According to the figure 5.50, the spatial mean Nusselt number at the east wall presented

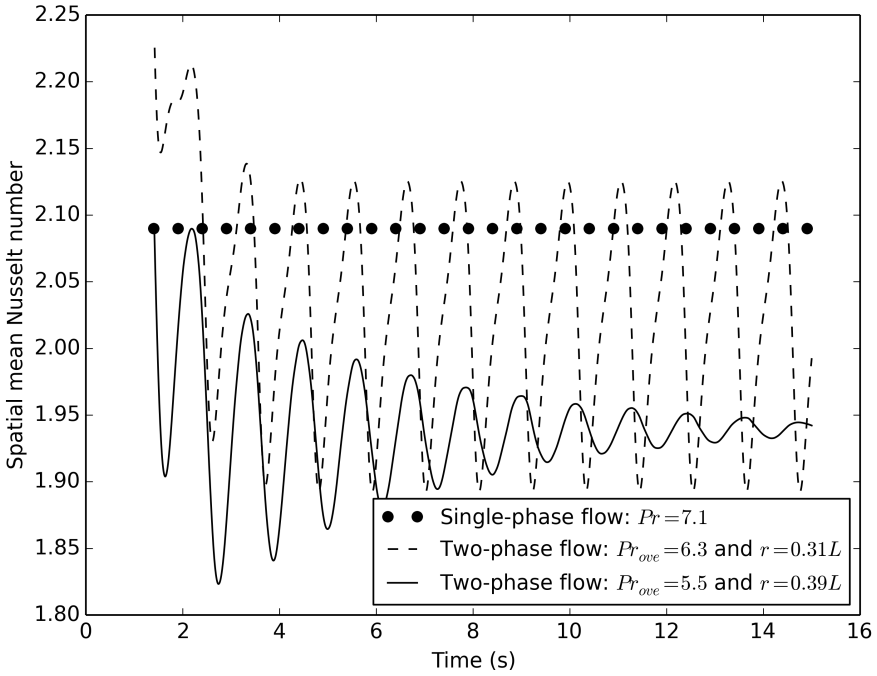

Figure 5.50: Spatial mean Nusselt number evolution for the single-phase case ($Pr = 7.1$) and two-phase flows cases with a dispersed phase with radius of $0.31L$ ($Pr_{ove} = 6.3$) and $0.39L$ ($Pr_{ove} = 5.5$).

values from about $+2\%$ to almost -12% compared to the single-phase case. The results reported in the figure 5.50 demonstrated the spatial mean Nusselt number decreasement when the dispersed phase was in the vinicity of the heated wall and the thermal transfer rate augmentation when the dispersed phase moved far away the heated wall. The maximum value of the Nusselt number was approximately the value from the single-phase case, since the dispersed phase has low influence on the thermal transfer rate when it was away from the heated wall.

The figure 5.50 exibited an example of the case where the addition of a dispersed phase did not enhanced thermal transfer rate at a surface in contact to the two-phase flow. In fact, the results presented in the figure 5.50 showed the severe reduction of the spatial mean Nusselt number in the two-phase flow cases compared to the single-phase case. In addition, the figure 5.50 illustrated the intensification of the overall Prandtl number influence in the thermal transfer rate in the case where the radius of the dispersed phase was larger. Therefore, the overall Prandtl number of the flow mixture and the bubble radius controled the reduction of the thermal transfer rate in the figure **??** since the tendency observed for the case with the bubble initial radius of $0.31L$ was more evident for the case where the initial bubble radius was $0.39L$.

Table 5.16: Summary of the thermal transfer rate results to compute the effects of the overall Prandtl number and the bubble radius variation.

	$\bar{Nu}$	$\bar{Nu}_{min}$	$\bar{Nu}_{max}$
Single-phase flow with $Pr = 7.1$	2.09	2.09	2.09
Two-phase flow with $Pr_{ove} = 6.3$ and $r = 0.31L$	2.03	1.89	2.12
Two-phase flow with $Pr_{ove} = 5.5$ and $r = 0.39L$	1.94	1.93	1.95

The table 5.16 presents the influence of the overall Prandtl number and the bubble radius on the thermal transfer rate using the spatial mean Nusselt number at the east wall.

The table 5.16 exibited the implications of the overall Prandtl number of the flow mixture on the spatial mean Nusselt number calculated at the heated wall. As the overall Prandtl number of the flow mixture reduced, the mean Nusselt number decreased. In accordance to a similar simulation performed, Qiu, Wang e Jiang (2014) found the reduction of the thermal transfer rate as the bubble radius increased. The spatial mean Nusselt number variation compared to the single-phase flow case presented in the table 5.16 drops the general accepted hypothesis of the Nusselt number increasement by the introduction of bubbles in single-phase flows.

Based on the results from Dabiri e Tryggvason (2015), the authors of the present papper believe in the intensification of the reduction of Nusselt number presented in the table 5.16 if the distance between the walls and the dispersed phase was lower. Finally, this last section provided several results refuting the argument generally seen in the literature that the introduction of bubbles necessarly increases the wall-to-fluid thermal transfer rate. Future works are neeeded to be conducted next in order to analyze new factors related to the topic, such as the influence of the bubble shape on the thermal transfer rates.

5.5.3 Simulations where the Prandtl number from the dispersed phase was the same from the continuos phase

In this section, simulations were performed to evaluate the thermal transfer rate in the situation where there the Prandtl number from the continuos phase was equal to the Prandtl number from the dispersed phase. Although the Prandtl number between the continuos and dispersed phases were similar, the Eckert and Brinkman numbers were different between the dispersed and continuos phases. The initial bubble radius was $0.31L$ and Gr=1.4×10^3.

The figure 5.51 shows the temperature and the isotherms for the two-phase flow cases with Gr=1.4×10^3 and Pr=0.71 with $Ec_{dis} = 5Ec_{con}$ and $Br_{dis} = 5Br_{con}$ (a) and $Ec_{con} = 2Ec_{dis}$ and $Br_{con} = 2Br_{dis}$ (b).

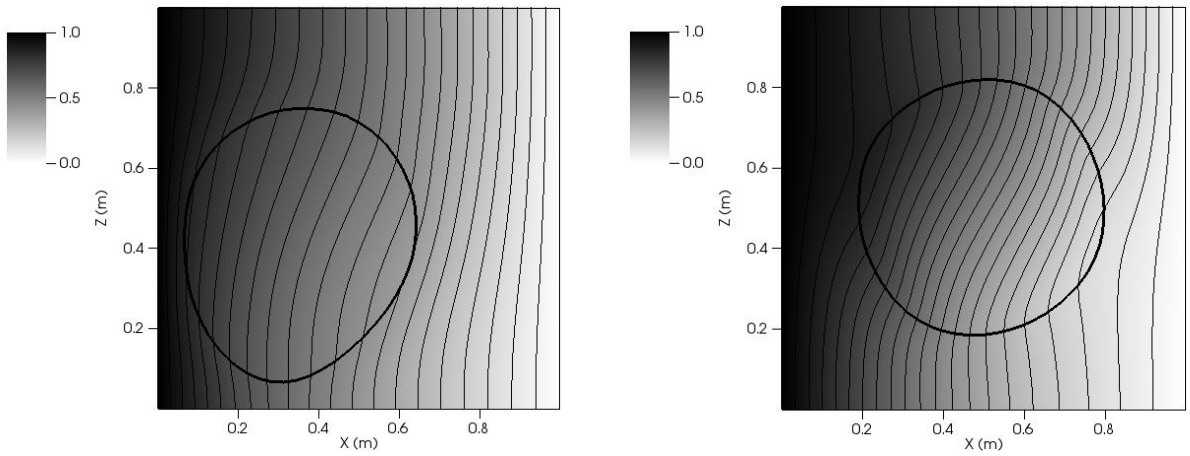

(a) (b)

Figure 5.51: Temperature field and isotherms at central xz-plane considering Gr=1.4×10^3 and Pr=0.71 for the two-phase flow cases with Gr=1.4×10^3 and Pr=0.71 with $Ec_{dis} = 5Ec_{con}$ and $Br_{dis} = 5Br_{con}$ (a) and $Ec_{con} = 2Ec_{dis}$ and $Br_{con} = 2Br_{dis}$ (b). The isotherms are represented in 20 thin isovalue contours, the thick contour represents the interface position and temperature field is presented in grayscale.

The influence of the Eckert number and Brinkman numbers difference between the phases are shown in the figure 5.51 According to the figure 5.51, not only the Prandtl number is relevant to the thermal transfer rates variations in two-phase flows. But, also the Eckert and Brinkman numbers.

The figure 5.52 shows the spatial mean Nusselt number evolution in time for the cases with similar Prandtl and Grashof numbers.

According to the figure 5.52, the spatial mean Nusselt number did present visible variations in time between the single-phase and two-phase cases with similar Prandtls between the phases but different Eckert and Brinkman numbers. Next, the influence of the Eckert and Brinkman numbers are separately investigated.

5.5.3.1 Influence of the Brinkman number in two-phase flows without phase-change

Simulations of two-phase flows with different Brinkman number between the phases although considering similar Prandtl numbers between the continuos and dispersed phases were performed. Three simulations were perfomed: a single-phase flow simulation and two two-phase

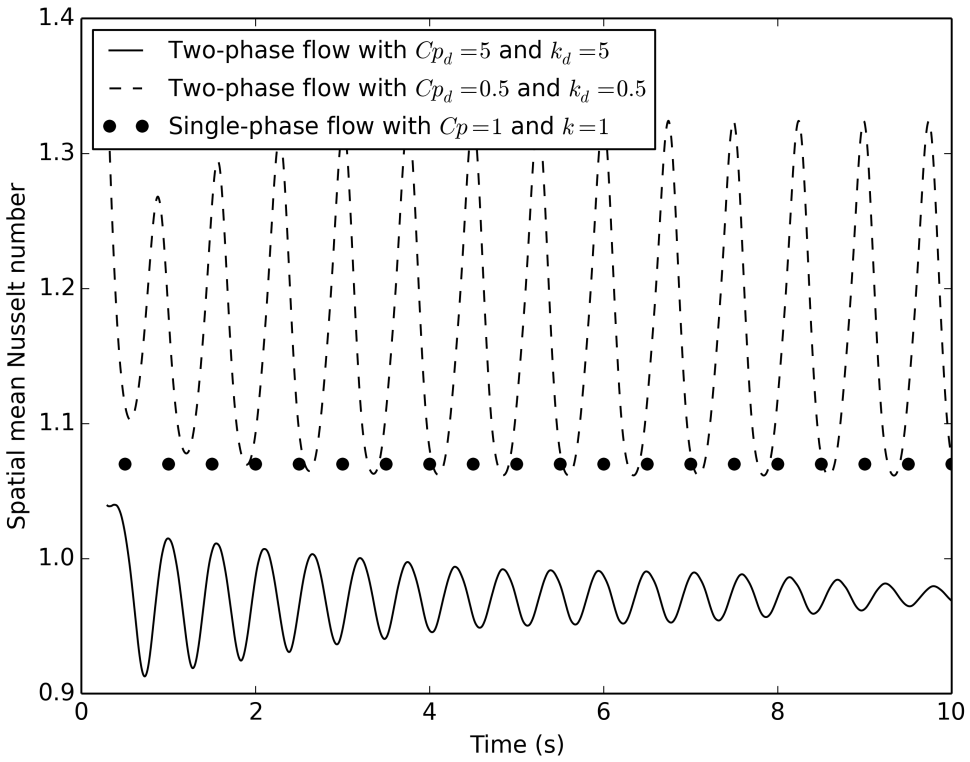

Figure 5.52: Temporal spatial mean Nusselt number variation for the cases with similar Prandtl and Grashof numbers.

flows simulations. All them were conducted considering for Gr=1.4×10^3, $Pr_{ove} = 0.71$. However, the two-phase flows simulations were performed considering the dispersed phase with Brinkman number 2 times lower or higher compared to the continuos phase.

The figure 5.53 shows the temperature and the isotherms configuration for the cases with Gr=1.4×10^3 and Pr=0.71 with $Br_{dis} = 5Br_{con}$ (a) and $Br_{con} = 2Br_{dis}$ (b).

The figure 5.54 shows the temporal evolution of the spatial mean Nusselt number for the two-phase flows cases and for the single-phase flows.

5.5.3.2 Influence of the Eckert number in two-phase flows without phase change

Two-phase flows simulations with different Eckert number were performed. The Eckert number was modified according to the diference with the specific thermal energy between the dispersed and continuos phase.

Three simulations were perfomed: a single-phase flow simulation and two two-phase flows simulations. All them were conducted considering for Gr=1.4×10^3, $Pr_{ove} = 0.71$. However,

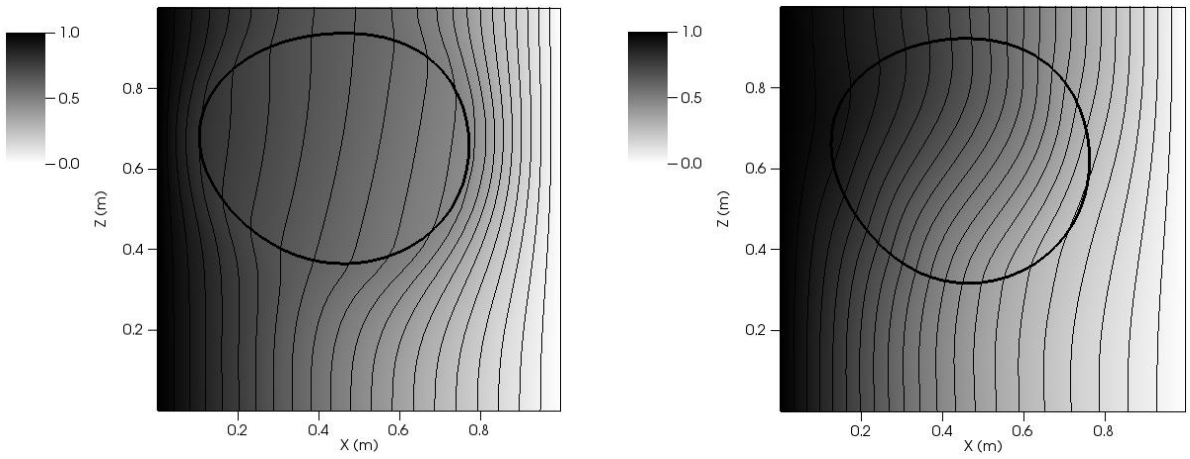

(a) (b)

Figure 5.53: Temperature and isotherms at central xz-plane for the cases with Gr=1.4×10^3 and Pr=0.71 with $Br_{dis} = 5Br_{con}$ (a) and $Br_{con} = 2Br_{dis}$ (b). The isotherms are represented in 20 thin isovalue contours, the thick contour represents the interface position and temperature field is presented in grayscale.

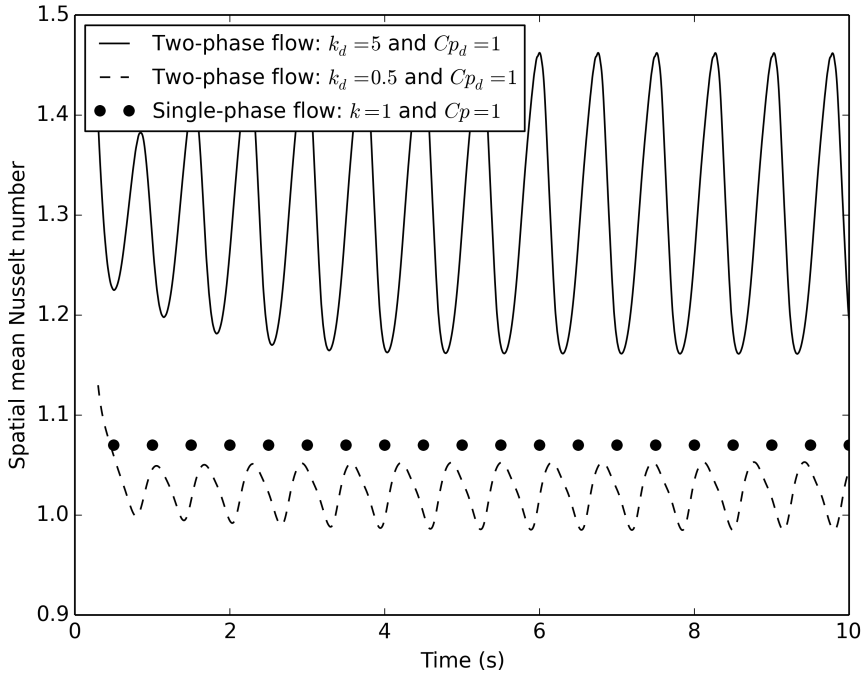

Figure 5.54: Spatial mean Nusselt number evolution for the single-phase case ($Pr = 0.71$) and two-phase flows cases with Gr=1.4×10^3, $Pr_{ove} = 0.71$.

the two-phase flows simulations were performed considering different Eckert number between the phases.

The figure 5.55 shows the temperature field and the isotherms configuration for the cases with Gr=1.4×10^3 and Pr=0.71 with $Ec_{dis} = 5Ec_{con}$ (a) and $Ec_{con} = 5Ec_{dis}$ (b).

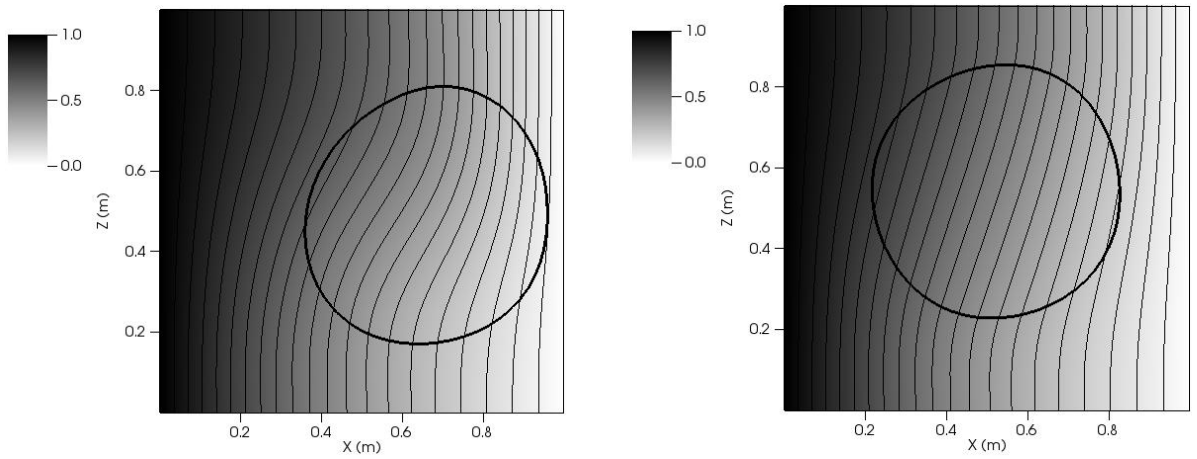

(a) (b)

Figure 5.55: Temperature field and isotherms at central xz-plane for the cases with Gr=1.4×10^3 and Pr=0.71 with $Ec_{dis} = 2Ec_{con}$ (a) and $Ec_{con} = 5Ec_{dis}$ (b). The isotherms are represented in 20 thin isovalue contours, the thick contour represents the interface position and temperature field is presented in grayscale.

The figure 5.56 shows the spatial mean Nusselt number for the single-phase flow case and for the other two-phase flows.

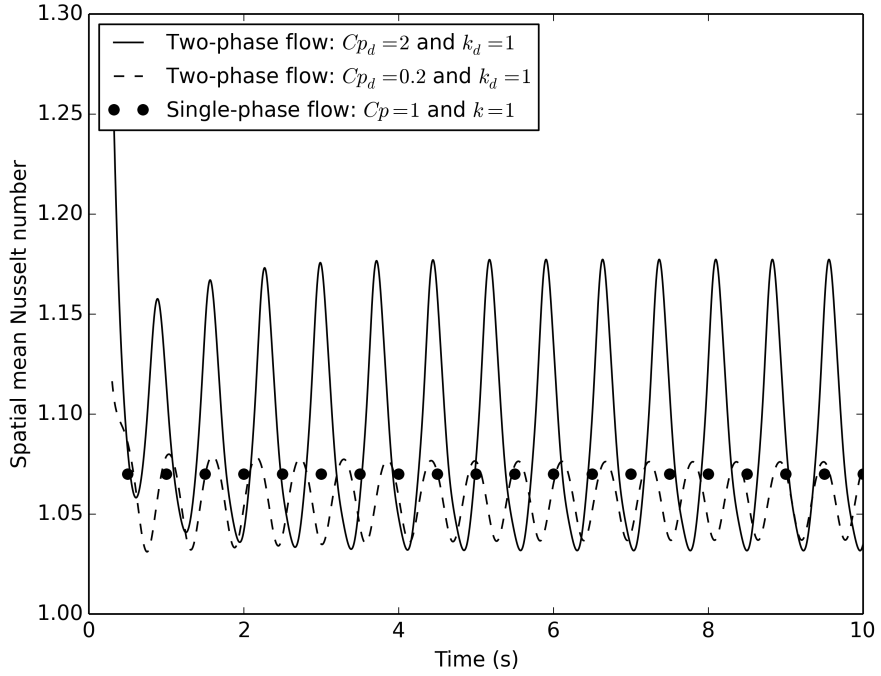

Figure 5.56: Spatial mean Nusselt number evolution for the single-phase case ($Pr = 0.71$) and two-phase flows cases with for Gr=1.4×10^3, $Pr_{ove} = 0.71$.

5.6 Validation of the phase change model in the MFSim code

In this section, four validation cases will be presented using the phase change model employed in the MFSim code. First, the subsection 1 will show the validation case of a vapor bubble inside a superheated liquid subjected to a constant rate of boiling. Then, the subsection 2 will show the case of boiling of superheated liquid where a vapor bubble is subjected to a variable rate of growth. Then, the subsection 3 will show the case of a film boiling where a Rayleigh-Taylor instability is developed. Finally, the subsection 4 will show a condensation case of an ascending vapor bubble in a subcooled environment.

5.6.1 Validation case 1: Boiling with a constant mass density flux

Simulations of bubble growth by phase change were performed imposing a constant and uniform mass flux across the interface. The initial bubble radius was equal to 0.01 m and a spatially uniform and temporally constant mass density flux of 0.10 kg/(m^{2}s) was imposed. The bubble grew until its radius was twice the initial radius. Then, the difference between the exact and the numerical radius was computed. The results obtained in the present work were compared to Tanguy *et al.* (2014), and with the exact solution from Eq. 18.

The boiling simulations at constant rate were performed using the following physical properties: $\rho_{liq} = 1000$ kg/m^3, $\rho_{vap} = 1$ kg/m^3, $\sigma = 0.07$ N/m, $\mu_{liq} = 0.001$ kg/(ms), and $\mu_{vap} = 1.78 \times 10^{-5}$ kg/(ms). Since the mass density flux was assumed constant, the flow was considered isothermal. An outflow boundary condition was imposed on all the domain faces and the flow was not subjected to gravity. The mesh consisted of a structured uniform three-dimensional Cartesian grid with configurations of $32 \times 32 \times 32$, $64 \times 64 \times 64$, and $128 \times 128 \times 128$ cells.

The figure 5.57 shows the interface contour at the simulation using the Delta and GFM methods, respectively.

It can be shown that the bubble radius will evolve linearly with time according to the following expression:

$$R_{exa}(t) = R_0 + \left[\frac{1}{\rho}\right] \dot{m}'' t, \tag{5.18}$$

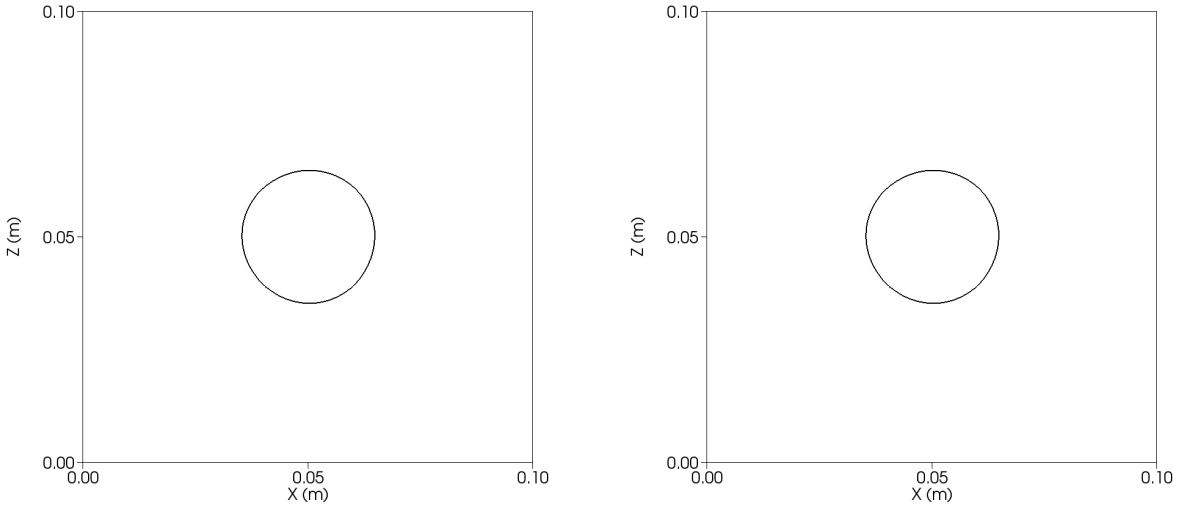

(a) (b)

Figure 5.57: Interface contour in the simulations using the Delta and GFM methods, respectively, at time t=0.5s, considering $\dot{m}'' = 0.10$ kg/(m^{2}s).

where $R_{exa}(t)$ represents the exact bubble radius, R_0 is the bubble's initial radius, and t is the time.

Fig. 5.58 shows the evolution in time of the bubble radius using the Delta and GFM methods. The error was obtained as the difference between the numerical bubble radius (R_{num})

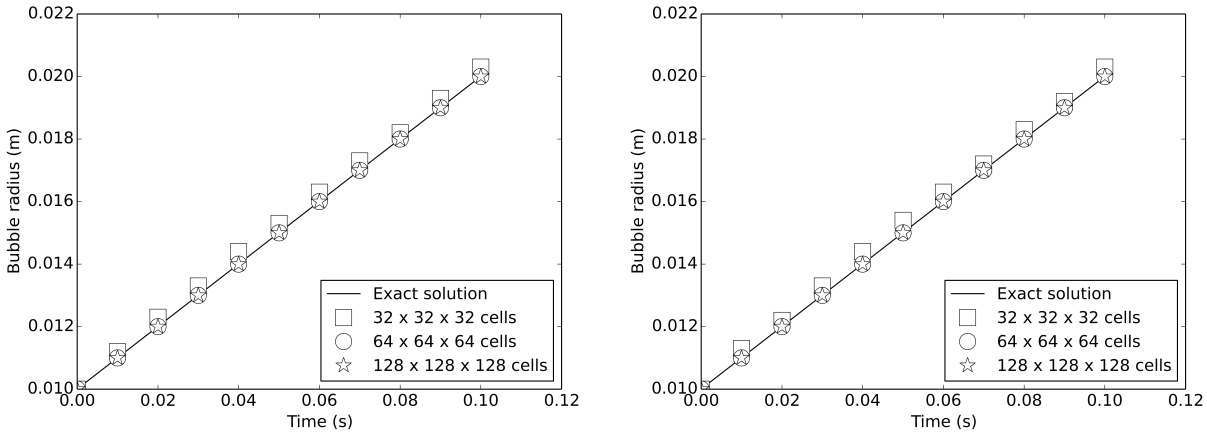

(a) (b)

Figure 5.58: Bubble radius evolution for $\dot{m}'' = 0.10$ kg/(m^{2}s) using the Delta (a) and GFM (b) methods.

and its exact value (R_{exa}), which is given by the following expression:

$$\varepsilon(\%) = \frac{|R_{num} - R_{exa}|}{R_{exa}} \times 100. \tag{5.19}$$

Table 5.17: Bubble radius error ε (%) for $\dot{m}'' = 0.10$ kg/(m^{2}s) .

	32^3	64^3	128^3
Tanguy *et al.* (2014) - GFM	0.51	0.22	0.11
Present work - GFM	1.50	0.50	0.05
Tanguy *et al.* (2014) - Delta	22.5	23.7	24.3
Present work - Delta	1.51	0.52	0.05

The bubble radius error at the simulation's final time is presented in Table 5.17 using three different mesh configurations for the Delta and GFM methods. The computed bubble radius in the present work exhibited low deviation compared to the exact solution, which can be easily seen in Table 5.17. Using the GFM method, Tanguy *et al.* (2014) and the present work exhibited no significant error compared to the exact solution. On the other hand, only the present work presents results from the Delta simulations with low deviation compared to the literature, since the error found by Tanguy *et al.* (2014) was higher than 20% for all the meshes tested.

The differences between the exact and the computated radii using the GFM and Delta methods were lower than 2.0% for all the simulations in the present work. In addition, the error from the Delta simulations was very similar to the error obtained from the GFM simulations for all mesh configurations. Therefore, according to the behavior of the interface evolution in time, both approaches of jump conditions demonstrated accurate results compared to the expected solution.

AMR simulations were also performed for this validation case in order to quantify the AMR efficiency compared to the uniform grid simulations considering a mass density flux of $0.1kg/(m^2s)$. The AMR simulations were performed using the properties and the physical model previously described and the Delta method for pressure interface treatment was employed in these simulations. The AMR simulations were performed with two, three and then four refinement mesh levels with the most refined level of $128 \times 128 \times 128$ cells.

In order to present a quantitative analysis of the AMR efficiency, the rate of efficiency was calculated using an expression from Akhtar e Kleis (2013) which uses the time and number of cells employed in the simulations. The expression of AMR efficiency is given by the following equation (AKHTAR; KLEIS, 2013):

$$\eta\,(\%) = \frac{t_{uni} n_{ada}}{t_{ada} n_{uni}} 100 \tag{5.20}$$

Table 5.18: Assessment of mesh configuration in the simulations with $\dot{m}'' = 0.1kg/(m^2s)$.

	Time (s)	Number of cells	ε (%)	η(%)
Uniform grid	1,440	884,736	0.05	-
AMR - two levels	480	157,248	0.06	53.3
AMR - three levels	300	74,304	0.07	40.3
AMR - four levels	240	66,304	0.09	45.0

where: t_{uni} is the simulation time using uniform grid, n_{uni} is the number of cells in the simulation using uniform grid, t_{ada} is the simulation time using AMR and n_{ada} is the number of cells in the simulation using AMR.

The table 5.18 presents the computational time spent in simulations, the number of cells employed, the error of the bubble radius prediction (ε) and the AMR efficiency (η). It was observed that the course grid regions represented more than half of the domain total volume, specially in the beggining of the simulation. In addition, the course grid away from the interface implied a relevant reduction of the computational cells number. Therefore, AMR is a numerical tool which can reduce computational costs for two-phase flows problems with phase change and allows more efficient simulations.

Two main advantages of using AMR instead of uniform grids was the reduction in the number of cells employed and computational time simulated. According to the results shown in table 5.18, uniform grid employed almost 900,000 cells while AMR used close to 160,000 cells with two levels and almost 75,000 cells with 3 levels. Therefore, AMR utilization reduced the number of cells in more than 10 times compared to uniform grid simulations. Moreover, computational time needed to finish the simulation was almost 5 times lower using an adaptive mesh with 3 levels compared to uniform grid. Finally, it can be noticed similar error between uniform grid and AMR simulations since error from bubble radius prediction was always bellow 1%. Therefore, according to table 5.18, AMR yielded accurate results with lower computational costs compared to uniform grids and reveled a great potential to be adopted in phase change simulations.

Concerning the AMR efficiency, the present work efficiencies were approximately 50%. On the other hand, Akhtar e Kleis (2013) found an efficiency close to 70% for similar simulations of boiling. Probably the AMR efficiency from the present work was lower than Akhtar e Kleis (2013) since the latter work used octree grids which uses a simplified algorithm, reducing time required to solve all the equations in each computational cell.

The figure 5.59 shows the mesh configuration at the simulation using AMR and the Delta method at time t=0s and t=0.05s.

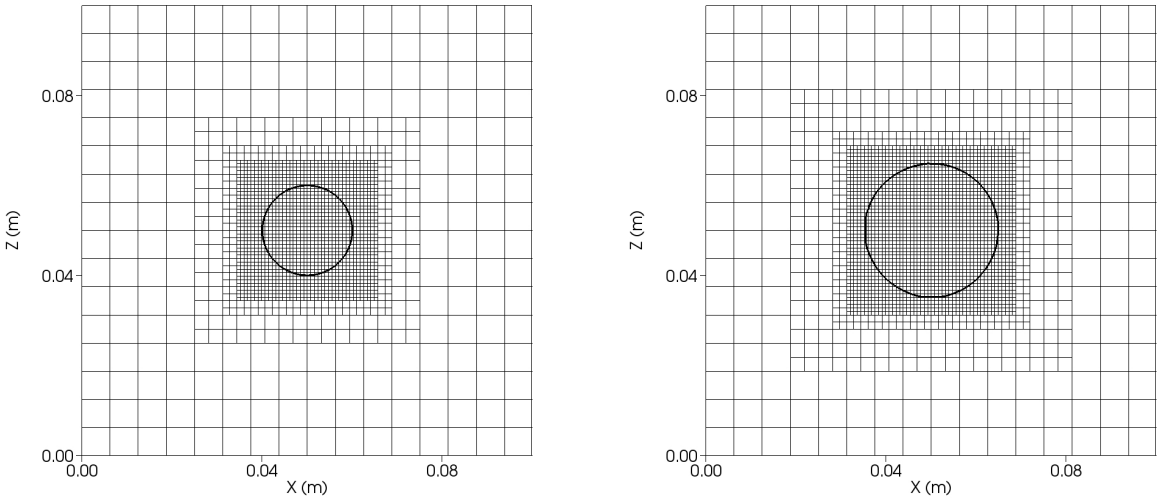

(a) (b)

Figure 5.59: Interface contour in the simulations using delta and GFM, respectively, at time t=0.5s, considering $\dot{m}'' = 0.10$ kg/(m^{2}s).

According to the figure 5.59, adaptive mesh refinement promoted great computational power spared, since a large region of the domain remained solved with a course grid.

5.6.2 Validation case 2: Boiling simulations with a variable mass density flux

Numerical simulations of a vapor bubble growth in a superheated liquid domain were conducted using the Delta and GFM methods to take into account the interface jump condition of pressure. The phase change simulations were performed using a Jakob number of 2.0. The Jakob number (Ja) is defined according to the following equation (TANGUY *et al.*, 2014):

$$Ja = \frac{\rho_{liq} Cp_{liq}(T_\infty - T_{sat})}{\rho_{vap} L}. \tag{5.21}$$

The following physical properties were adopted in the phase change simulations with a variable mass density flux: $\rho_l = 100$ kg/m^3, $\rho_v = 1$ kg/m^3, $\sigma = 0.01$ N/m, $\mu_l = 0.00062$ kg/(ms), $\mu_v = 0.000012$ kg/(ms), $k_l = 0.10$ W/(mK), $k_v = 0.01$ W/(mK), $Cp_{liq} = 20$ J/(kg K), $Cp_{vap} = 10$ J/(kg K), and a latent energy of 1000 J/kg . An outflow boundary condition was imposed on all domain faces, and the flow was not subjected to gravity. AMR simulations

were performed with three or four mesh levels and the base level presented the configuration of $16 \times 16 \times 16$ cells.

The numerical model validation was conducted according to the error of the bubble radius in comparison with an analytical solution available in Scriven (1959). The analytical solution describes the evolution of the bubble radius in time according to the following expression (SCRIVEN, 1959):

$$r(t) = 2\beta\sqrt{\alpha t}. \tag{5.22}$$

The parameter β is found by solving a transcendental equation in Scriven (1959), which is derived from the energy and continuity equations in spherical coordinates (TANGUY *et al.*, 2014). Simplified equations were proposed and presented in Scriven (1959) and the following expression was adopted to calculate β (SCRIVEN, 1959):

$$\beta = \sqrt{\frac{3}{\pi}} \left\{ \frac{\Delta T}{\left(\frac{\rho_g}{\rho_l}\right)\left[\frac{L}{Cp_l} + \left(\frac{Cp_l - Cp_g}{Cp_l}\right)\Delta T\right]} \right\}. \tag{5.23}$$

The initial radius of the bubble was 0.0287 m and the temperature difference between the saturation condition and the superheated liquid was 1.0 K. The figure 5.60 shows the temperature field and the mesh configuration at the simulation time t=3.5s.

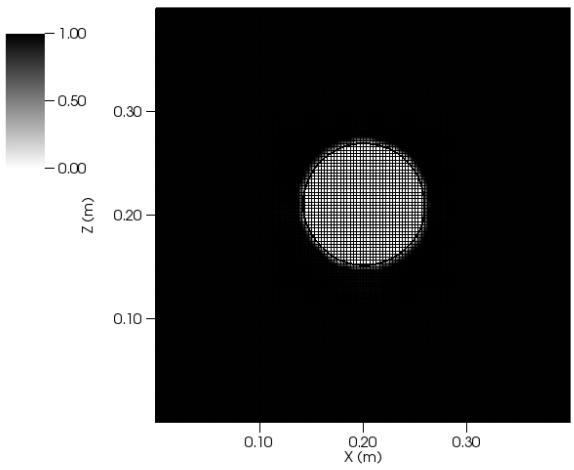

Figure 5.60: Interface, temperature field and mesh configuration at time 3.5 s at the central xz-plane.

As figure 5.60 shows, the temperature field is almost completely uniform outside the bubble (where the liquid is superheated), and next to the interface, there is a small region where the temperature gradients exist (about 3 cells of length).

Fig. 5.61 shows the interface contour using the Delta method at the initial condition and at 3.0s.

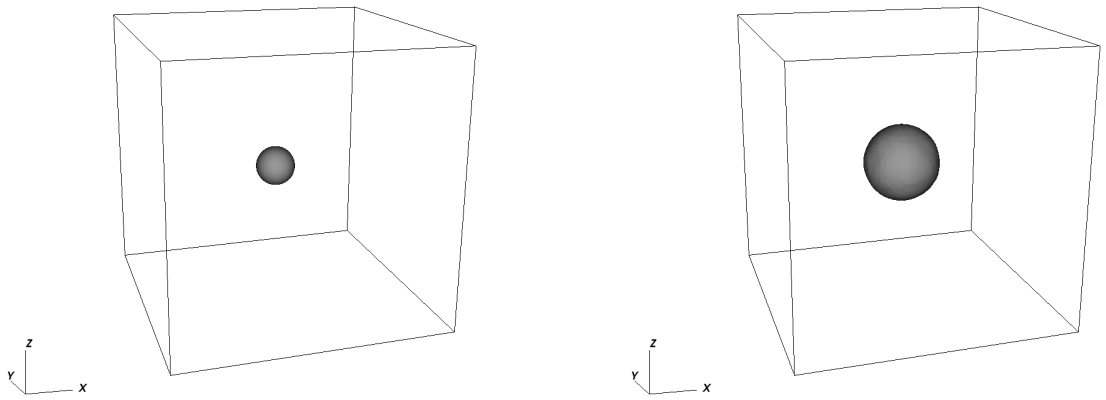

(a) (b)

Figure 5.61: Interface contour with the Delta method at initial time (a) and at 3.0s (b).

Fig. 5.62 shows the interface contour using the GFM method at the initial condition and at 3.0s.

Fig. 5.63 shows the evolution of the bubble radius in time in comparison to the analytical solution from Scriven (1959). The grid configuration with three mesh levels was sufficiently fine to provide accurate results, similarly to the mesh with four levels. Good agreement was obtained between the computed bubble radius and the bubble radius from the analytical solution. According to Fig. 5.63, the simulations using the Delta and the GFM methods for pressure only deviated slightly from the analytical solution. The evolution of the bubble radius was close to the expected solution provided by Scriven (1959) from the beginning until the end of the simulation time.

Fig. 5.64 illustrates the mesh configuration for the Delta methods at time t=0s (a) and t=3.6s (b).

According to the figure 5.64, the AMR promoted great reducement of the computational

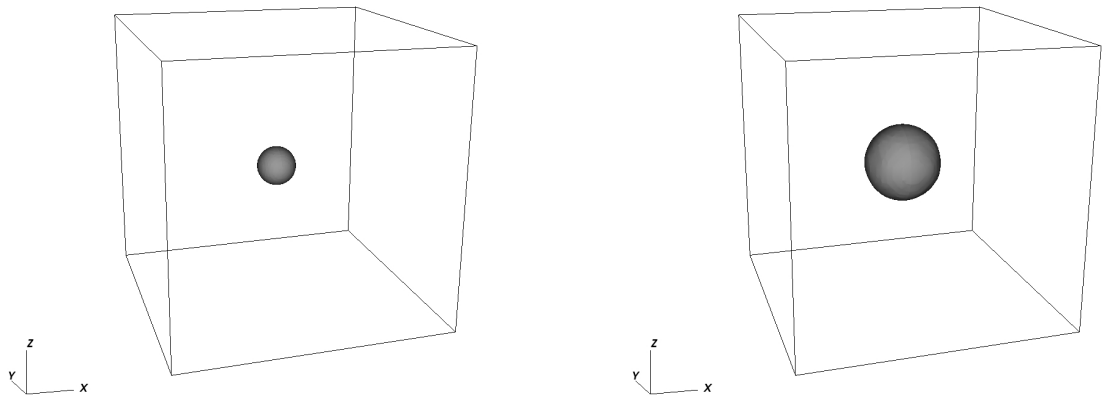

(a) (b)

Figure 5.62: Interface contour with the GFM method at initial time (a) and at 3.0s (b).

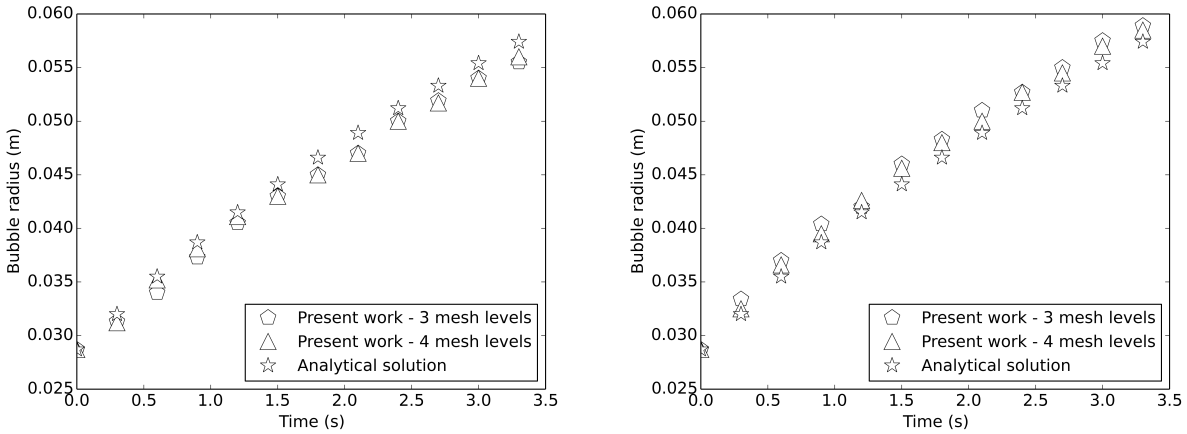

(a) (b)

Figure 5.63: Bubble radius evolution using the Delta method (a), and the GFM method (b).

power required since a large region of the domain was solved using a course grid. Next, another case of phase change is presented where AMR was employed.

5.6.3 Validation case 3: Simulation of film boiling with Rayleigh–Taylor instability

Pool boiling systems are widely encountered on the ground and in outer space applications (YANG; PAN; XU, 2014). Film boiling is an important phase change phenomenon since it is present in several applications in the engineering field (SHARP, 1984). In addition, film boiling is one of more ideal pool boiling regimes to validate a method, due to its lesser complexity (LEE; R.; AUTE, 2017). A particular case of film boiling is the development of Rayleigh–Taylor instability,

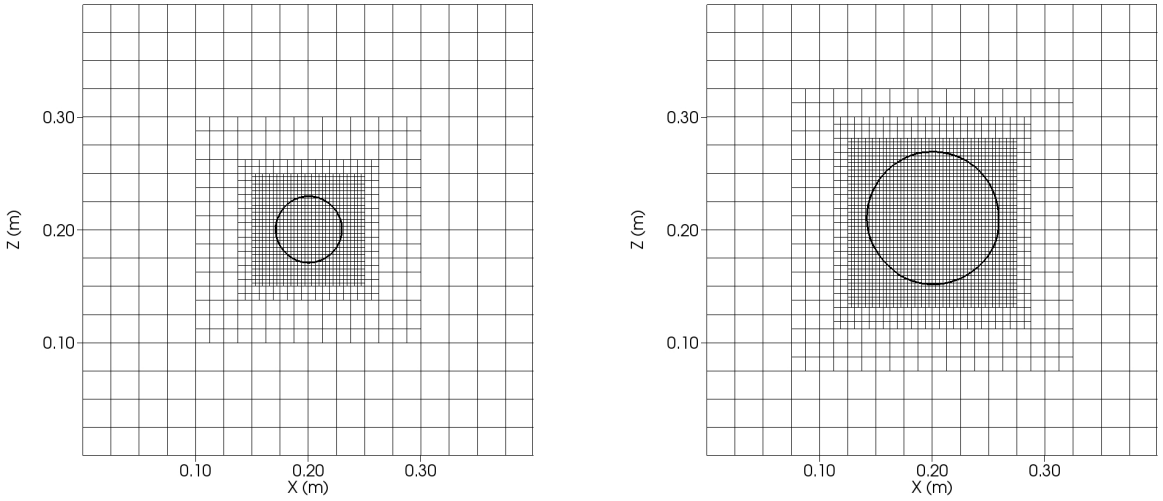

(a) (b)

Figure 5.64: Slice of the central xz-plane showing the interface and the mesh configuration for the Delta methods at time t=0s (a) and t=3.6s (b) , considering a variable mass density flux with $Ja = 2.0$.

which is widely reported in the phase change literature.

Rayleigh–Taylor instability is the result of a baroclinic torque created by the misalignment of the pressure and specific mass gradients at an interface (S.; CANDLER; DIMOTAKIS., 1991). Rayleigh–Taylor instability occurs when a heavy fluid initially lies above a lighter one in a gravitational field (SHARP, 1984), promoting a baroclinic torque. The baroclinic torque is mathematically represented in the transport equation of vorticity (ω), which can be obtained by taking the curl of the momentum equation, and is given by the following equation:

$$\frac{D\vec{\omega}}{Dt} = -(\vec{\omega}.\vec{\nabla})\vec{v} + \frac{(\vec{\nabla}\rho \times \vec{\nabla}p)}{\rho^2} + (\vec{\omega}.\vec{\nabla})\vec{v} + \frac{1}{Re}(\vec{\nabla}^2\vec{\omega}) \tag{5.24}$$

The baroclinic contribution is represented by the term $\frac{(\vec{\nabla}\rho\times\vec{\nabla}p)}{\rho^2}$ and is always perpendicular to the specific mass gradient. If the specific mass and pressure gradients are aligned, this term is zero.

This instability has a particularly important application in inertial confinement fusion (ROBERTS; JACOBS, 2016). Although Rayleigh–Taylor instability is rarely observed in its authentic form, it plays an important role in various natural and technological processes. The formation of bubbles from a vapor film beneath a liquid in film boiling is a classic example of a relatively authentic Rayleigh–Taylor instability (TRYGGVASON, 1988). Sharp (1984) enumer-

Table 5.19: Assessment of mesh configuration in the simulations of film boiling.

ρ_l/ρ_v	μ_l/μ_v	k_l/k_v	Cp_l/Cp_v
4.78	2.59	3.56	0.66

ated some examples of Rayleigh–Taylor instabilities in nature and in technological fields, such as the overturn of the outer portion of the collapsed core of a massive star, the formation of high luminosity twin-exhaust jets in rotating gas clouds in an external gravitational potential, Laser implosion of deuterium–tritium fusion targets, electromagnetic implosion of a metal liner, and several others.

The simulations were performed using AMR and uniform grids. The Delta method was employed to model the interface treatment of pressure. The thermal transfer rate will be compared to an experimental correlation from Berenson (1961), which predicts the thermal transfer rate at a heated wall where pool boiling occurrs. Berenson's (BERENSON, 1961) experimental correlation defines the mean Nusselt number at the heated wall according to the following expression:

$$Nu = 0.425 \left(\frac{GrPr}{Ja} \right)^{1/4}, \tag{5.25}$$

where the Prandtl number is 1.0, the Jakob number is 1.0, and the Grashof number is 304.3.

The thermo-physical properties of the fluid used in the simulations has the same ratio between the liquid and vapor phase as that in Akhtar e Kleis (2013), as given in Table 5.19.

In the simulation of film boiling, a vapor film completely covers the heated surface. During the entire simulation, the denser liquid above the vapor film falls, due to the action of gravity, and at the same time the interface between the liquid and vapor rises away from the heated wall. As the liquid moves closer to the heated wall, evaporation at the liquid–vapor interface prevents the liquid from getting into contact with the wall. Since the intensity of the baroclinic torque increases with time, an interface peak at the center of the domain emerges.

The physical model in the simulations consists of a three-dimensional domain subjected to gravity. The lateral boundaries are symmetric and an outflow boundary condition is used at the top surface. Moreover, a constant temperature is imposed at the bottom wall:

$$T_{wall} = T_{sat} + \Delta T. \tag{5.26}$$

The bottom wall was kept at a fixed temperature, higher than the temperature of the top and lateral walls, similarly to the procedure adopted by Akhtar e Kleis (2013). The computational domain was subjected to a grid independence study and a validation was performed using the mean Nusselt number at the bottom wall. Fig. 5.65 illustrates a slice from the central xz-plane with the interface position for three grid configurations: $32 \times 32 \times 64$, $64 \times 64 \times 128$ and $128 \times 128 \times 256$ cells.

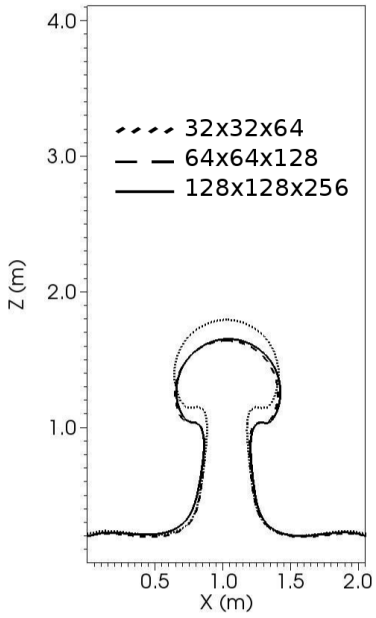

Figure 5.65: Interface at time 12.0 s where the dotted line represents the mesh of $32 \times 32 \times 64$ cells, the dashed line is the mesh configuration of $64 \times 64 \times 128$ cells, and the continuos line shows the grid with $128 \times 128 \times 256$ cells.

Fig. 5.65 shows that the two highest mesh resolutions closely match each other (dashed and dotted lines). On the other hand, the coarsest grid presented a very different profile from the other grid configurations, due to the insufficient mesh quality. Therefore, the mesh with the configuration of $64 \times 64 \times 128$ cells was considered adequate to model film boiling.

In order to validate the Nusselt number at the bottom wall using an experimental correlation from the literature, a simulation using a uniform grid was perfomed using the configuration of $64 \times 64 \times 128$ cells and an AMR simulation was performed with three mesh levels. The most refined level in the AMR simulation presented the same mesh width as the uniform grid simulation.

Fig. 5.66 shows two moments in the simulation of film boiling, namely the beginning and the end of the simulation time. The two coherent structures composing the Rayleigh–Taylor instability are evident in Fig. 5.66 at the final time of the simulation. There are four noticeable

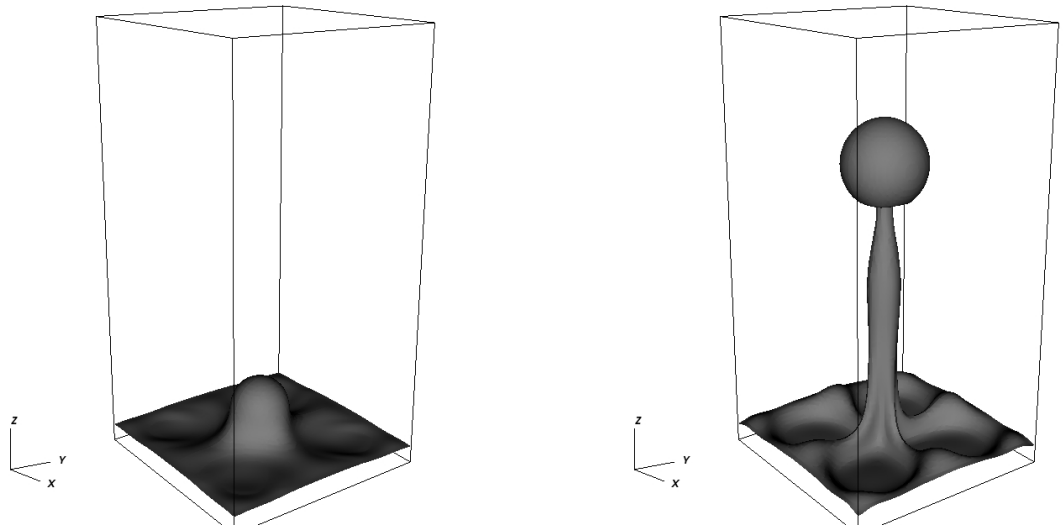

(a) (b)

Figure 5.66: Interface at the initial time of the simulation (a) and at the final time (b).

spikes (fluid structure of heavy fluid growing into light fluid) and one mushroom-shaped bubble (fluid structure of light fluid growing into heavy fluid). As Figure 5.66 shows, the stem does not pinch off.

Fig. 5.67 shows the interface contour and the grid configuration employed at the initial time of the simulation and at the final time. Adaptive mesh refinement promoted a great reduction of

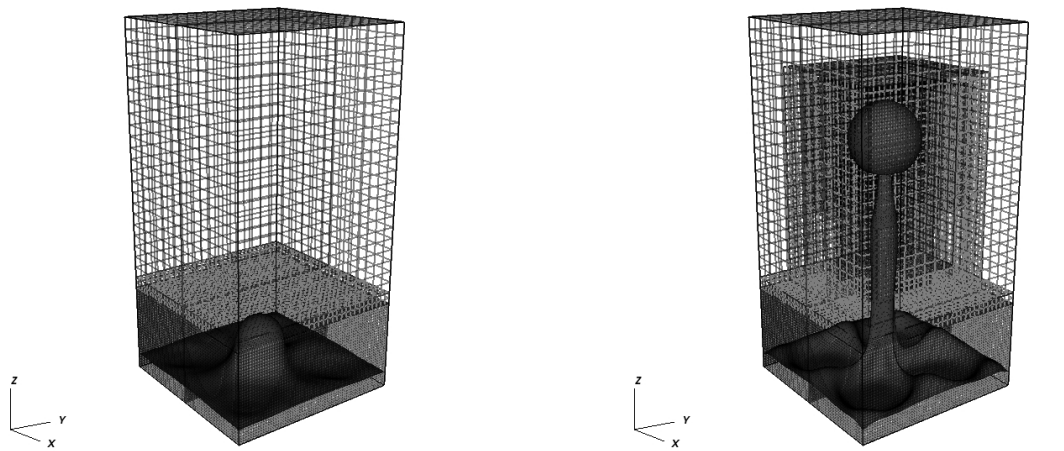

(a) (b)

Figure 5.67: Interface and mesh configuration (a) at the initial time of the simulation and (b) at the final time.

the computational costs. As Fig. 5.67 shows, the regions away from the interface used a coarse grid, which helped the simulation to run faster than with a uniform grid. Since the interface was

Table 5.20: Assessment of mesh configuration in the simulations of film boiling.

	Time (s)	Number of cells	Mean Nusselt number difference (%)
AMR	57600	172000	2.5
Uniform grid	82800	524288	2.3

the region where the phenomenon was developed, the other regions of the domain were solved with a relatively coarse grid.

Table 5.20 shows the time necessary to run the simulation using AMR and uniform grids, as well as the mean number of cells used in each simulation. According to Table 5.20, AMR promoted a reduction of approximately 30% of CPU time compared to the simulation using uniform grids. As expected, the number of cells employed in the AMR simulation was significantly lower than the uniform grid simulation. The reduction of nearly 67% from the total number of cells sharply reduced the computational power required. Thus, AMR simulations have again achieved accurate results while saving computational power and the time necessary to run the simulations.

According to expression 21, the AMR efficiency was approximately 47%, representing a great improvement of efficiency. Akhtar e Kleis (2013) evaluated the AMR efficiency using that expression and found approximately 52% at a simulation time of 1.0 s, which corroborates the efficiency obtained in the present work.

The experimental correlation of Berenson (1961) will now be used for the minimum thermal flux, which is the condition where there is a stable vapor film over the heating surface. The spatial mean Nusselt number can be computed at the bottom wall and is presented in Fig. 5.68 in comparison to the solution from Berenson (1961).

As previously seen in Akhtar e Kleis (2013), the mean Nusselt number remains approximately constant after some time, according to Fig. 5.68. A good agreement was found between the computational results obtained in the present work and the experimental correlation from Berenson (1961). Therefore, the computational results in this subsection confirmed the accuracy of the model for complex phase change problems using a diffuse interface treatment with accuracy and physical consistency.

According to the results from the simulations of film boiling with the development of Rayleigh–Taylor instability, the diffuse interface treatment for pressure demonstrated good accuracy, which was confirmed by the validation of the local thermal transfer rate and the physical

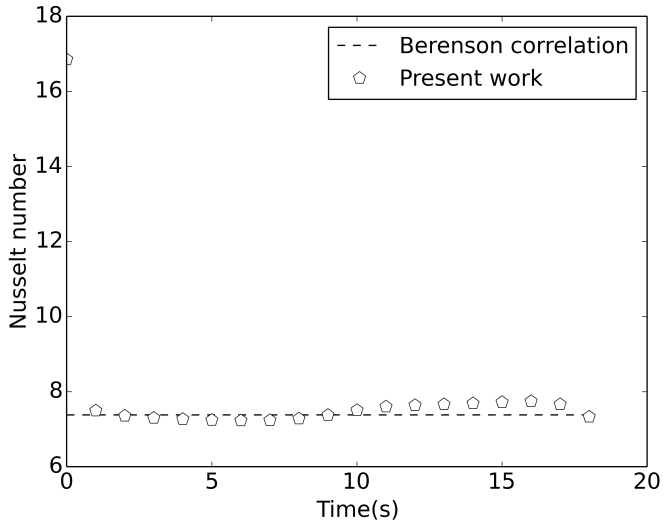

Figure 5.68: Evolution in time of the spatial mean Nusselt number in the film boiling simulation.

Table 5.21: Fluid properties employed in the simulations of a single water vapor bubble condensation.

Fluid properties	Vapor	Liquid
Specific mass (kg/m^3)	1.5	953.0
Dynamic viscosity (Pas)	0.000013	0.0021
Thermal conductivity (W/mK)	0.02	0.68
Specific thermal energy (J/kgK)	2110.0	4224.0

behavior expected from the theory of stability analysis according to the visualization of the baroclinic torque action in the simulations.

5.6.4 Validation case 4: An ascending condensing water vapor bubble in a subcooled water liquid

In order to validate the model used to study the case of the condensing vapor jet in the present thesis, simulations of a single water vapor bubble in condensation were performed and the results obtanied were compared to the previous experimental results from Kamei e Hirata (1990).

In this problem, a single water vapor bubble at saturation is subjected to a quiescient subcooled environment of liquid water at atmospheric pressure. The vapor bubble ascension occurs at the same time as the condensation process occurs. The simulation duration is 3ms and the adopted time step was 0.000001s. The fluid properties employed in the simulations are displayed at the table 5.21.

In addition to the properties shown at the table 5.21, the latent heat was 2237 KJ/kg and the surface tension coefficient was 0.057 N/m. The Jakob number was 30.

The figure 5.69 shows the temperature field and the mesh configuration at the simulation time t=30 ms.

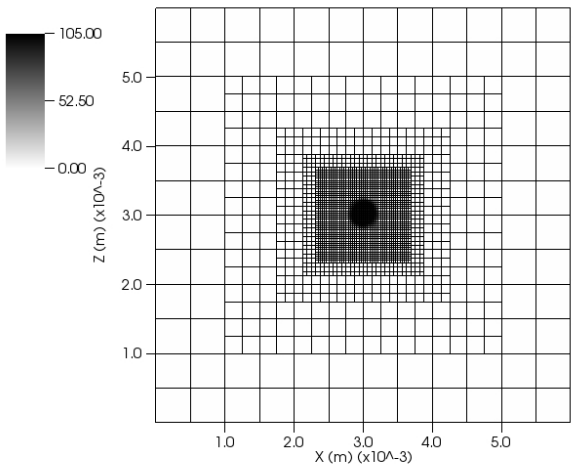

Figure 5.69: Interface, temperature field and mesh configuration at time 3.0 ms at the central xz-plane.

The figure 5.70 shows the vapor bubble at the initial (a) and final time (b), respectively, of the simulation. The vapor bubble reduced approxitemaly 5 times its initial size in 3ms in the

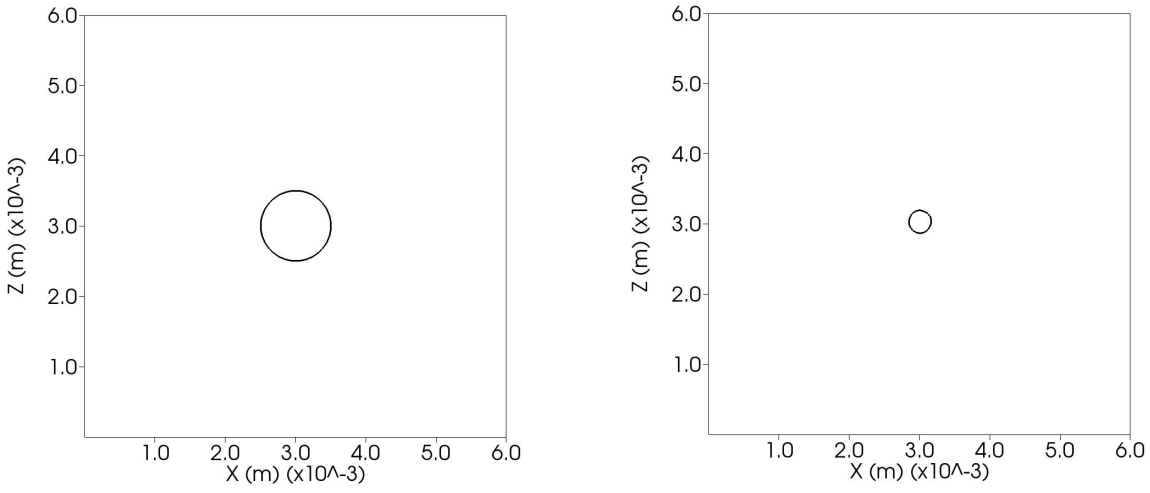

Figure 5.70: Central xz-plane with the interface contour at the beggining (a) and at the end (b) of the simulations of a single water vapor bubble condensation.

simulations performed, as shown in the figure below. The experimental data from Kamei e Hirata (1990) indicates that the bubble completely vanishes in 3ms, confirming the results obtanied in

the computational simulations.

The figure 5.71 illustrates the time history of the bubble radius from the present work and the experimental data from Kamei e Hirata (1990). The numerical results from Samkhaniani e Ansari (2016) are also presented in the figure 5.71, although its error was excessively high.

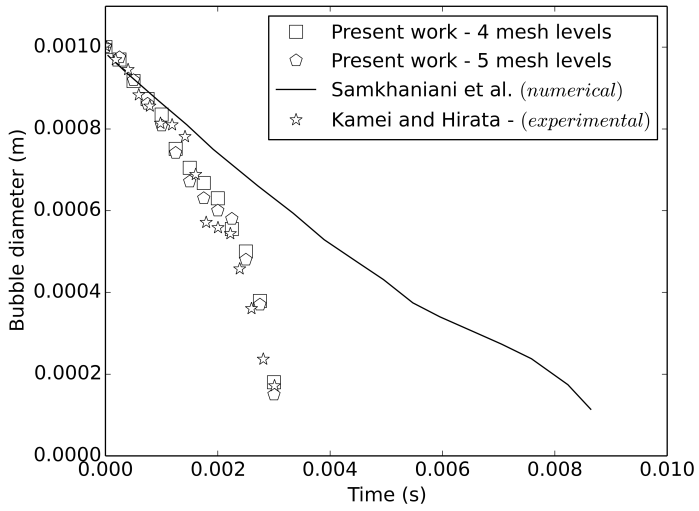

Figure 5.71: Time history of the water vapor bubble diameter from the simulations from the present paper and the results from the literature.

The vapor bubble condenses progressively faster as the volume vapor bubble is reduced in time, as previously seen in Kamei e Hirata (1990). According to the figure 5.71, the present model was considered validated since it provided accurate results for modelling phase change phenomenon.

Figure 5.72 shows the mesh configuration of the bubble condensation case at the initial time. According to the figure 5.72, the adaptive mesh refinement simulation reduced greatly the computational power required compared to the uniform grid simulation. The number of cells in the uniform grid simulation was 884,736; on the other hand, the mean number of cells in the adaptive mesh refinement simulation was 35,776, which represents a reduction of almost 25 times in the number of cells used in the simulation. The time necessary to run the adaptive mesh refinement simulation was also significantly reduced compared to the uniform grid simulation. The adaptive mesh refinement simulation required only 1800s to accomplish the physical time of 3ms; on the other hand, the uniform grid required approxitemaly 10800s. Therefore, the adaptive mesh refinement simulation was approxitemaly 6 times faster in comparison to the uniform grid

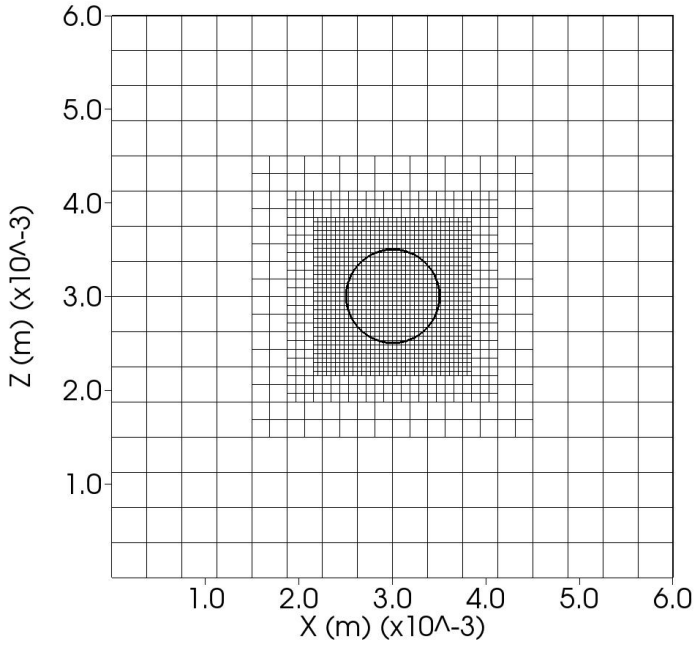

Figure 5.72: Central xz-plane with the interface contour and mesh configuration at the time $0.00005s$ of the simulation of a single water vapor bubble condensation.

simulation.

5.7 Evaluation of the spurious currents in phase change problems

In order to evaluate the spurious currents, phase change simulations were performed with a growing bubble with three different constant and uniform mass density fluxes.

The boiling simulations at constant rate were performed using the following physical properties: $\rho_{liq} = 1000$ kg/m^3, $\rho_{vap} = 1$ kg/m^3, $\sigma = 0.07$ N/m, $\mu_{liq} = 0.001$ kg/(ms), and $\mu_{vap} = 1.78 \times 10^{-5}$ kg/(ms). Since the mass density flux was assumed constant, the flow was considered isothermal. The bubble's initial radius was 0.01 m and the spatially uniform and temporally constant mass density fluxes of 0.1 kg/(m^{2}s), 1.0 kg/(m^{2}s), and 10 kg/(m^{2}s) were imposed.

The mass density flux of 0.1 kg/(m^{2}s) represents a moderate intensity of phase change, which is found in several numerical investigations in the literature, such as Tanguy *et al.* (2014). This phase change rate is also similar to that found in experimental cases, such as water bubble condensation at atmospheric pressure from Kamei e Hirata (1990). Next, the mass density flux of 1.0 kg/(m^{2}s) represents a strong phase change rate, which may refer to an extremely severe thermodynamic condition for phase change. Finally, the mass density flux of 10 kg/(m^{2}s)

represents an extreme rate of phase change intensity which may be considered even impossible to model on small scales due to the fast speed of the volume change in time. The purpose of evaluating the spurious currents using this high phase change intensity is to drawn conclusions about the two methods in the most severe conditions possible.

The time step was set as 1.0×10^{-5} s and the evaluation of the spurious currents was carried out at 0.001 s. Numerical simulations using AMR were conducted with two mesh levels and the base level presented the configuration of $32 \times 32 \times 32$ cells. The interface presence was considered the refinement criterion.

Fig. 5.73 shows the velocity fields using the Delta and GFM methods for a mass density flux of 0.1 kg/(m^{2}s) at 0.001 s. The maximum velocity observed in the simulations using the

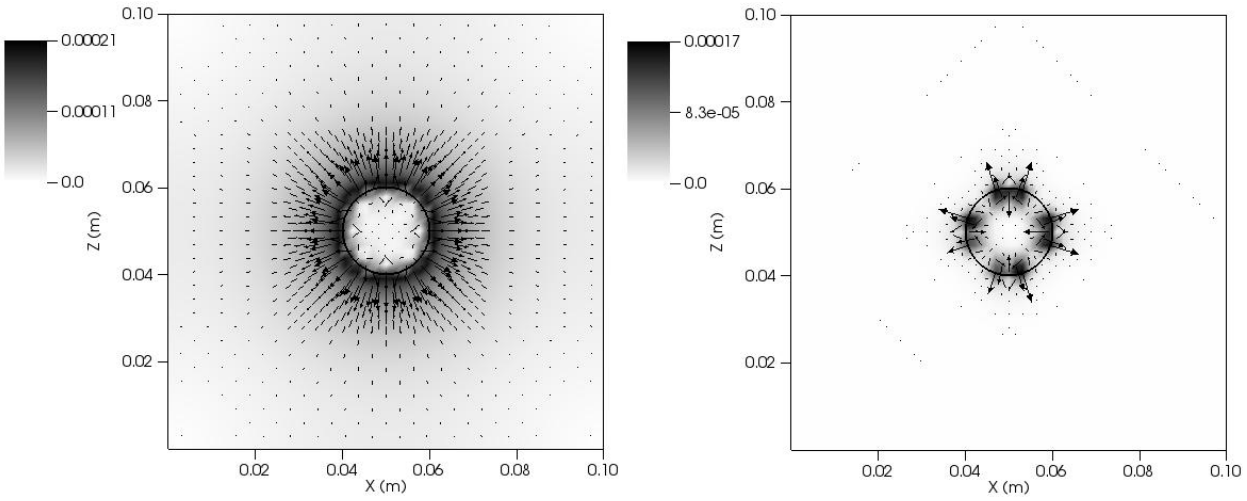

(a) (b)

Figure 5.73: Spurious currents for $\dot{m}'' = 0.1$ kg/(m^{2}s) at 0.001 s, (a) with Delta and (b) with GFM.

Delta and GFM methods in Fig. 5.73 was close to 0.0002 m/s. Inside the dispersed phase, both approaches produced some spurious currents, which exhibited similar magnitudes. The mass density flux of 0.1 kg/(m^{2}s), in the simulation using Delta, produced a visible velocity field at the interface region, which extended to the domain limits. The simulation using GFM presented a velocity field with low influence of spurious currents outside the bubble. The present paper found spurious currents one order of magnitude lower than Tanguy *et al.* (2014), who obtained spurious currents close to 0.05 m/s using the Delta method and 0.01 m/s using the GFM approach.

Fig. 5.74 shows the interface contour using the Delta and GFM methods for a mass density flux of 0.1 kg/(m^{2}s) at 0.001 s.

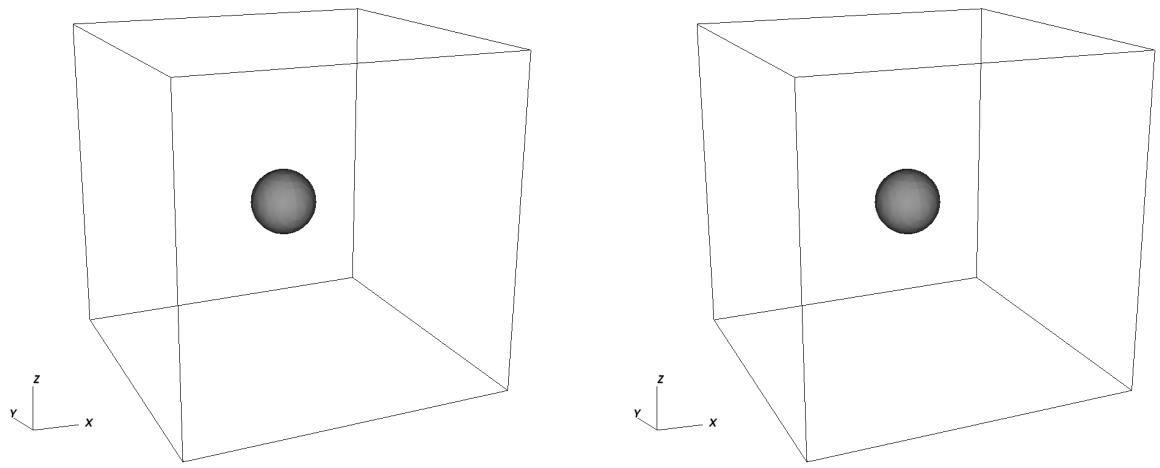

(a) (b)

Figure 5.74: Interface contour for $\dot{m}'' = 0.1$ kg/(m^{2}s) at 0.001 s, (a) with Delta and (b) with GFM at simulation's final time.

Fig. 5.75 shows the velocity fields using the Delta and GFM methods for a mass density flux of 1.0 kg/(m^{2}s) at 0.001 s.

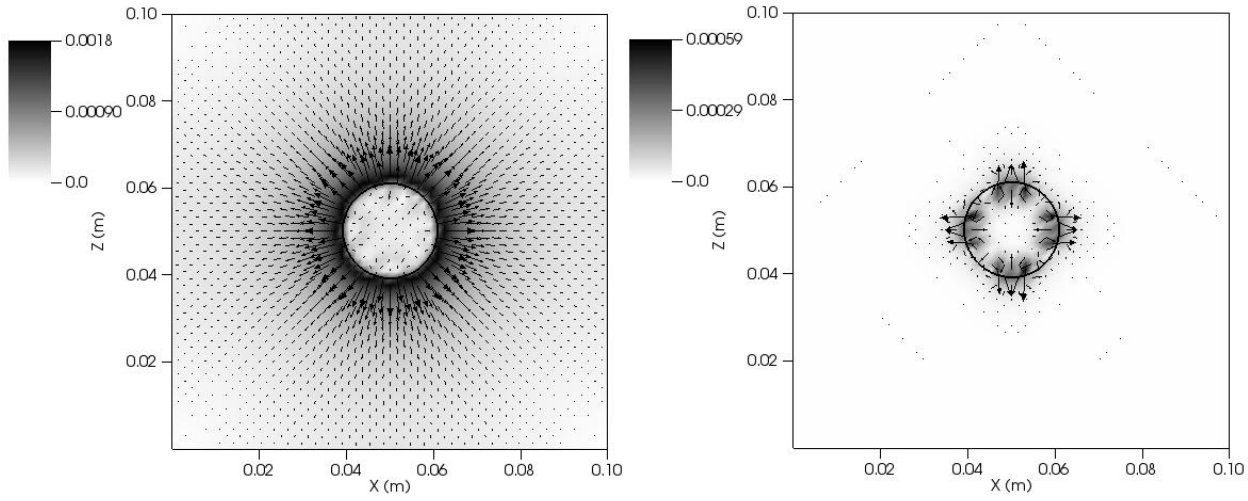

(a) (b)

Figure 5.75: Spurious currents for $\dot{m}'' = 1.0$ kg/(m^{2}s) at 0.001 s, (a) with Delta and (b) with GFM.

The velocity field obtained from the simulation using the GFM method presented smaller spurious currents compared to the Delta method. The simulation using the GFM method has only small velocities inside the dispersed phase; outside the bubble, there are no spurious currents. The magnitude of the spurious currents in the simulation using the Delta method was twice that

of the the velocities obtained in the GFM method.

Fig. 5.76 shows the interface contour using the Delta and GFM methods for a mass density flux of 0.1 kg/(m^{2}s) at 0.001 s.

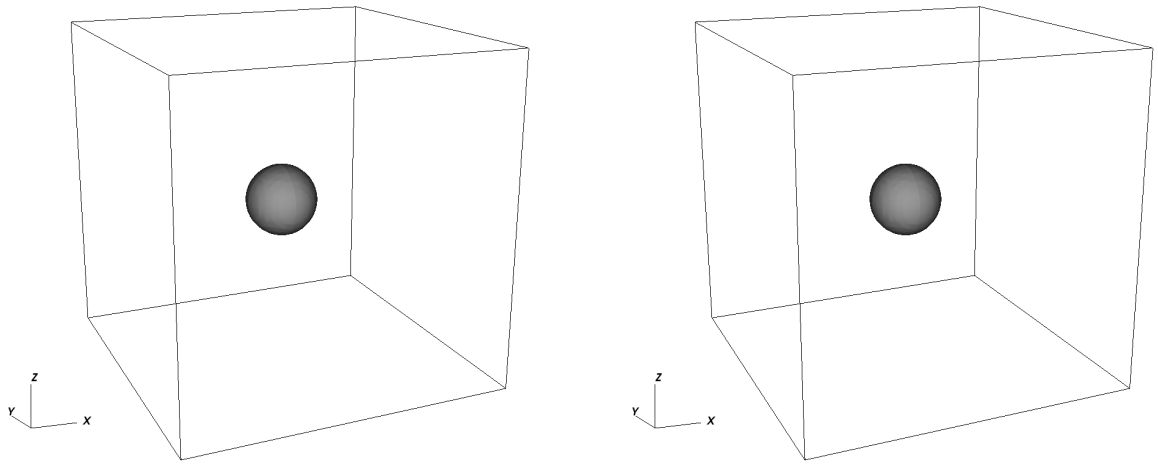

(a) (b)

Figure 5.76: Interface contour for $\dot{m}'' = 0.1$ kg/(m^{2}s) at 0.001 s, (a) with Delta and (b) with GFM at simulation's final time.

Fig. 5.77 shows the velocity fields using the Delta and GFM methods for a mass density flux of 10.0 kg/(m^{2}s) at 0.001 s. The simulation considering a mass density flux of 10.0 kg/(m^{2}s)

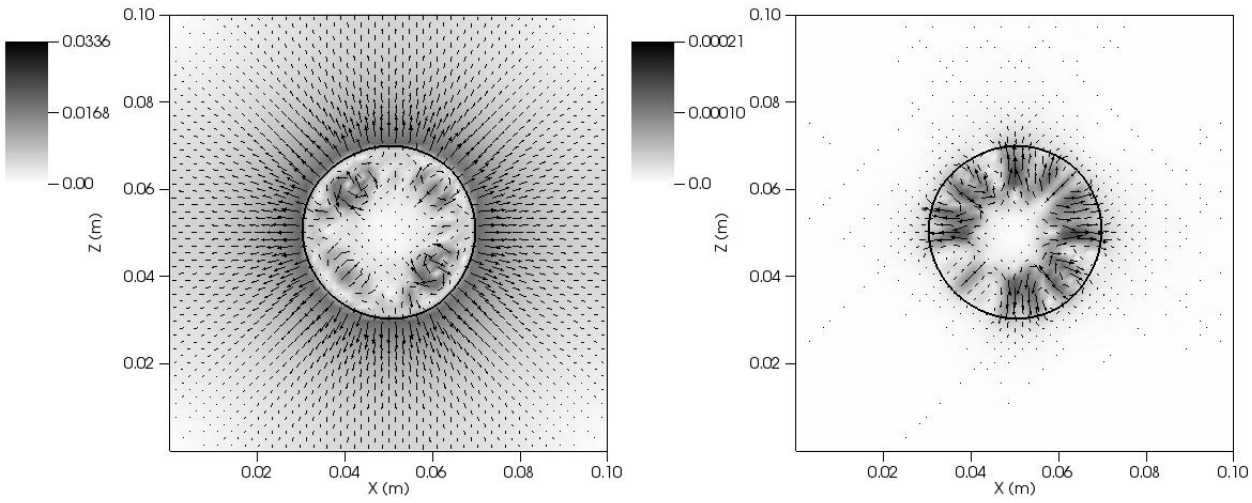

(a) (b)

Figure 5.77: Spurious currents for $\dot{m}'' = 10.0$ kg/(m^{2}s) at 0.001 s, (a) with Delta and (b) with GFM.

produced a spurious velocity field with significant magnitudes with the Delta method compared

to the GFM method. The maximum velocities were observed in the proximities of the interface and the spurious currents extended to the limits of the domain. The simulation using the GFM method presented smaller spurious currents than the Delta method, and they were two orders of magnitude lower than for Delta.

Fig. 5.78 shows the interface contour using the Delta and GFM methods for a mass density flux of 0.1 kg/(m^{2}s) at 0.001 s.

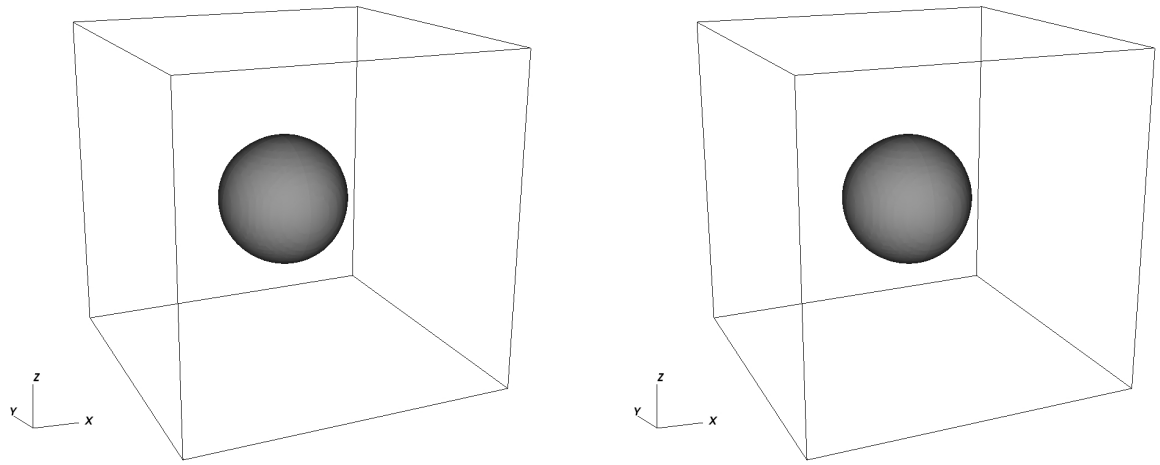

(a) (b)

Figure 5.78: Interface contour for $\dot{m}'' = 0.1$ kg/(m^{2}s) at 0.001 s, (a) with Delta and (b) with GFM at simulation's final time.

The numerical results of the magnitudes of the spurious currents in the simulations were expected, since the GFM method treats the interface as sharp by defining ghost cells, preserving a behavior that is more physically consistent with an interface. As described by Tanguy *et al.* (2014), preserving the sharpness of the velocity field allows transporting the interface with an adequate velocity, which is zero in the present case, since the bubble is stationary. Therefore, the GFM method minimized the numerical diffusion across the interface, which is particularly important in phase change problems.

According to the velocity fields obtained from the simulations using the Delta method, a mass density flux of 0.1 kg/(m^{2}s) did not produce noticeable spurious currents compared to the velocity fields from the GFM approach. On the other hand, a mass density flux of 1.0 kg/(m^{2}s) or higher did increase excessively the spurious currents in the simulations using the Delta method, in comparison to the GFM approach. Therefore, the magnitude of the mass density flux directly

Table 5.22: Spurious currents using different $\dot{m}''$ for Delta and GFM methods at 0.001 s.

Mass density flux kg/(m^{2}s)	Delta (m/s)	GFM (m/s)
0.1	0.0002	0.0001
1.0	0.0018	0.0005
10.0	0.0330	0.0002

Table 5.23: Simulation time for Delta and GFM methods.

Method	Delta (m/s)	GFM (m/s)
Time (s)	340.5	456.0
Mean number of iterations per time step	5	7

affected the intensity of the spurious currents obtained in the simulations with the Delta method.

Table 5.22 summarizes the magnitudes of the spurious currents found at the end of the simulation, using the Delta and GFM approaches, with mass density fluxes of 0.1 kg/(m^{2}s), 1.0 kg/(m^{2}s), and 10.0 kg/(m^{2}s).

It's important to mention in the present work the difference between simulations computational time between Delta and GFM methods. The Delta method is about 20 % faster than the GFM method, since the numerical condition in the GFM method takes the interface descontinuity more severely. In addition, smaller time steps were registred using GFM method compared to Delta, in order to avoid the non-convergence.

Table 5.23 summarizes the time necessary of the simulation, using the Delta and GFM approaches with mass density fluxes of 0.5 kg/(m^{2}s). Therefore, the GFM method has presented higher computational costs compared to the Delta method. The user of the code may choose which method would be better for the situation and the conditions offered.

5.8 Evaluation of particular forces in phase change problems

In this section, two forces related to phase change problems are described. The first force investigated is the recoil force, which is employed in some literature works, although is not modelled in all the works found due to its small magnnitude. The second force studied in the present thesis is an additional force discovered from the authors of the present work. This force has not being described yet by the phase change literature using CFD, however, the present thesis has quantified and analyzed its importance to phase change problems.

Table 5.24: Fluid properties of saturated water at near critical pressure.

Phase	ρ [kg/m^3]	$\mu[\mu$Pa.s]	Cp [J/kg.K]	k [W/mK]
Vapor	242.7	32.38	3520	0.538
Liquid	402.4	46.7	2128	0.545

5.8.1 Analysis of the recoil force in momentum equation

According to Nikolayev *et al.* (2016), the importance of the recoil force increases in the vinicity of the critical point of a substance since the magnitude of the surface tension force becomes closer to the magnitude of the recoil force. Therefore, numerical simulations of bubble growth by phase change were performed near the critical point. Numerical simulations of water vapor condensation near critical pressure were performed using the fluid properties presented in Table 5.24.

This simulation was previously conducted by Lee, R. e Aute (2017) using the recoil force term in the mathematical model. The diffuse interface treatment was applied to the pressure in the phase change simulations. In addition, the latent energy was 276.4 kJ/kg, the surface tension coefficient was 7.0×10^{-5} N/m, and the temperature difference between the vapor and the liquid was 1 K. Numerical simulations using AMR were conducted with three mesh levels and the base level presented the configuration of $24 \times 24 \times 24$ cells. The interface presence was considered the refinement criterion.

Since the specific mass difference between the phases is small due to the thermodyamic condition (near critical point), the effects of phase change would be deeply small. In order to test a more challenging situation, the specific mass jump between the phases was considered equal to 1; then, the effects of recoil force have been magnified to the tests performed here.

As previously seen in the last subsection, the bubble radius evolves linearly with time according to expression 18. Fig. 5.79 presents the bubble radius evolution in time from the simulations, both including and excluding the term that models the effects of the recoil force in the momentum equation. Fig. 5.79 shows good agreement between the exact solution and the results presented here for the simulation with a constant mass density flux of 0.01 kg/m^{2}s. As expected, the evolution of the bubble radius was linear in time since the mass density flux was taken to be constant.

Fig. 5.80 shows the magnitude of the surface tension force effects compared to the magni-

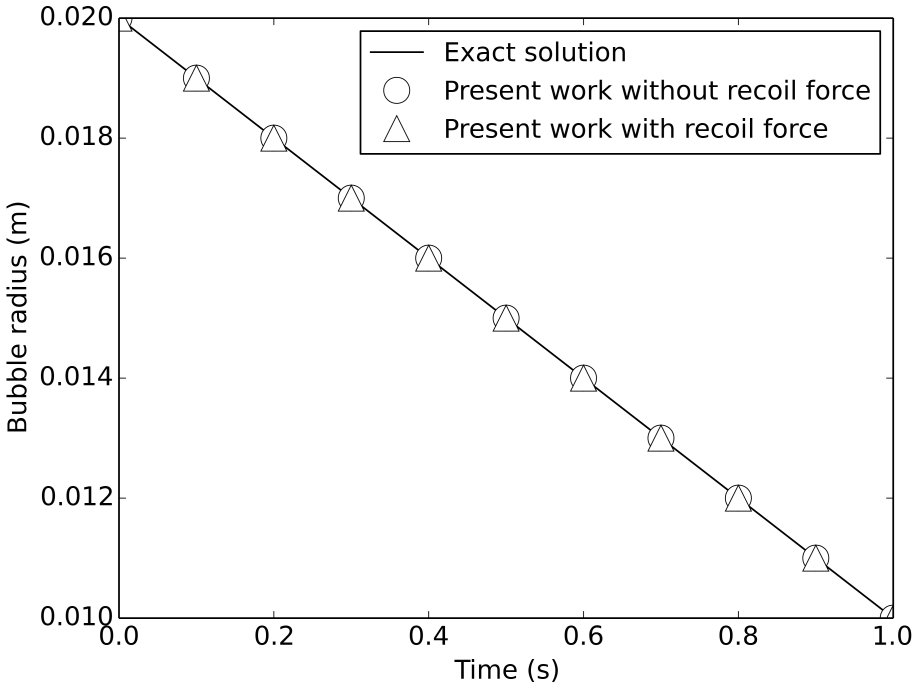

Figure 5.79: Bubble radius evolution in phase change simulations with and without the recoil force effects using the Delta method.

tude of the recoil force term. According to the data collected during the simulation, the magnitude

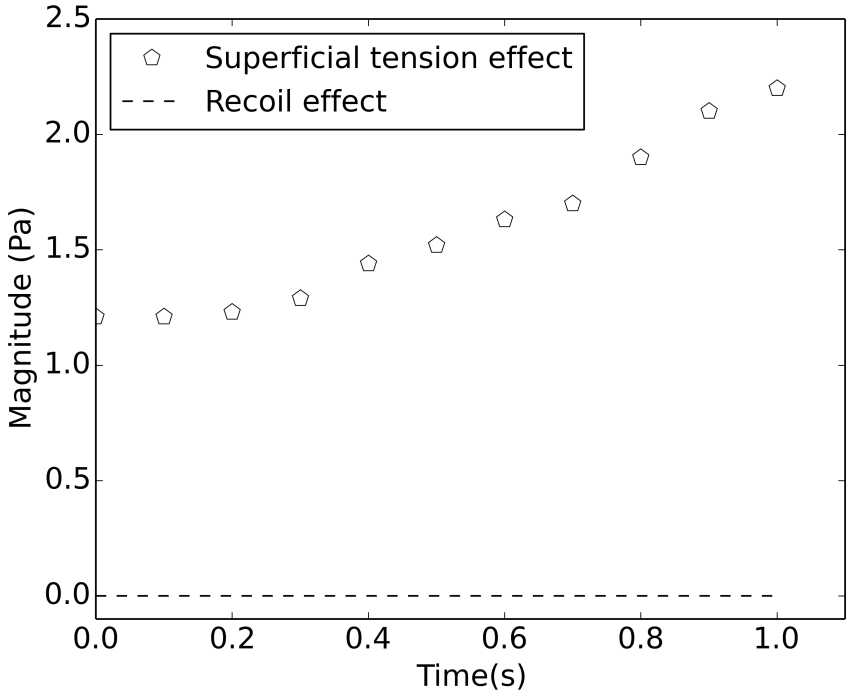

Figure 5.80: Magnitude of the effects from the surface tension force compared to the recoil force using the Delta method.

of the recoil force was approximately five orders of magnitude lower than the surface tension force. Since the inertial and surface forces were bigger than the recoil force in the momentum equation in the case investigated, the addition or not of the recoil force had only insignificant effects on the bubble rate movement. Raghupathi e Kandlikar (2016) also found only an insignificant influence of the recoil force term in similar simulations of phase change.

Until the present moment, the only numerical investigation found in the literature that revealed a significant influence of the recoil force has been Raghupathi e Kandlikar (2016) for simulations where two different regions of the interface were subjected to strong temperature differences, there occuring a visible interface motion due to the recoil force. Therefore, more studies are necessary to understand the influence of the recoil force in phase change problems, especially for engineering applications. In addition, the way the recoil force is being modeled in the literature should be better investigated since alternative approaches could provide a more realistic influence of the recoil force than the expression proposed by Nikolayev *et al.* (2016).

5.8.2 Analysis of the additional force in momentum equation

In order to quantify the influence of modeling the additional force due to phase change, which appears in the non-divergent form of the momentum equation, simulations were performed with and without the extra source term in momentum equation. A constant mass density flux was imposed at the interface and the effects of this force due to phase change on the time evolution of the interface were evaluated. Simulations of boiling were performed for a intense value of mass density flux and the influence of the extra force term was evaluated.

Simulations of bubble growth by phase change were performed by imposing a constant and uniform mass transfer rate across the interface. This case was previously investigated by Tanguy *et al.* (2014), where the bubble initial radius was equal to 0.01 m and a spatially uniform and temporally constant mass density flux of 0.1 kg/(m^{2}s) was imposed. The bubble grew until its radius was twice the initial radius; then, the difference between the exact and the computational radius was computed. The interface evolution was compared to the exact solution provided from Eq. 18.

The simulations were performed using the following physical properties: $\rho_{liq} = 1000$ kg/m^3, $\rho_{vap} = 1$ kg/m^3, $\sigma = 0.07$ N/m, $\mu_{liq} = 0.001$ kg/(ms) and $\mu_{vap} = 1.78 \times 10^{-5}$ kg/(ms).

Since the mass density flux was constant, the flow was considered isothermal. The outflow boundary condition was imposed on all the domain faces and the flow was not subjected to gravity. Numerical simulations using AMR were conducted with three mesh levels and the base level presented the configuration of $16 \times 16 \times 16$ cells. The interface presence was considered the refinement criterion.

As previously seen, the bubble radius evolves linearly with time according to expression 18. Fig. 5.81 shows the evolution in time of the bubble radius for the non-divergent form of the momentum equation, both with and without the additional source term.

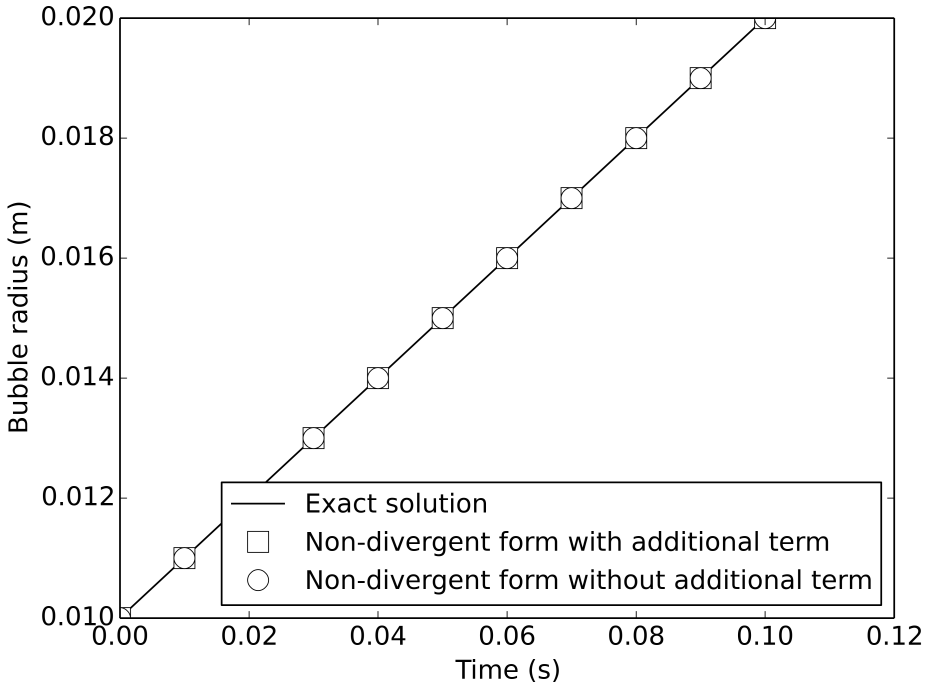

Figure 5.81: Bubble radius evolution in the phase change simulations using delta for the non-divergent form with and without the extra force term.

The interface evolution was not damaged even with a high mass density flux imposed at the interface. Then, according to the numerical results seen in Fig. 5.81, the influence of the force due to the phase change at the interface is of little importance for the interface's behavior over time.

The extra force in the momentum equation was about three orders of magnitude lower than the surface tension force effects. The quantification of the additional force demonstrated that its insignificance in the numerical results are a consequence of its magnitude's being smaller than the inertial and interfacial forces. Fig. 5.82 shows the magnitude of the surface tension force

effects compared to the magnitude of the additional force term.

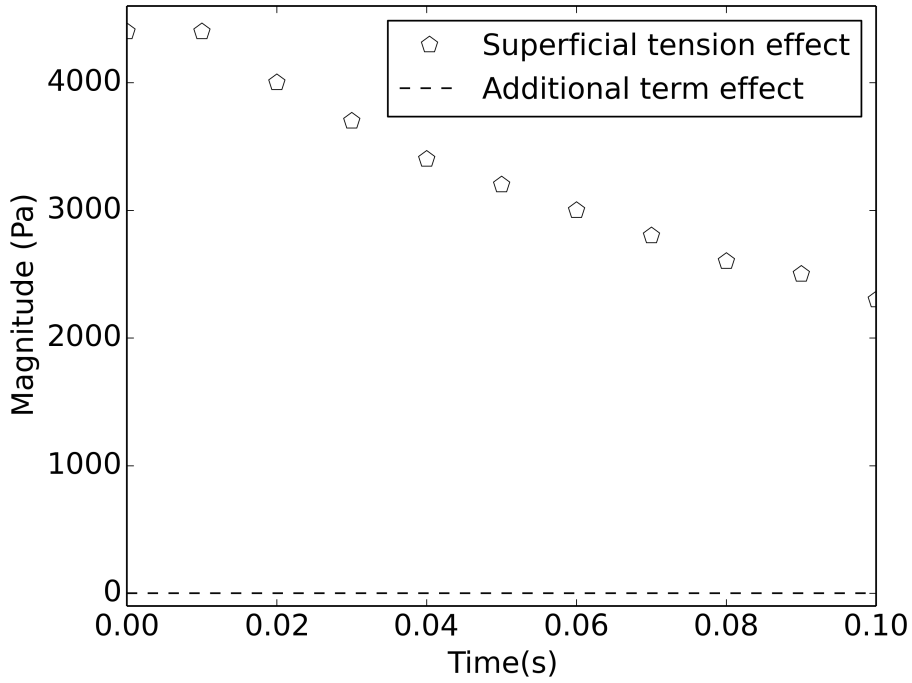

Figure 5.82: Magnitude of the effects of the surface tension force compared to the additional force using the Delta method, for $\dot{m}'' = 0.1$.

The negligible influence of this force term in the non-divergent form of the momentum equation in the simulations performed corroborates previous results in the literature, which presenting accurate validation cases while not employing this force term, namely Welch e Wilson (2000), Lee, R. e Aute (2017) and Tanguy *et al.* (2014). Therefore, the influence of this term may be considered of little importance in phase change problems when using the non-divergent form of the momentum equation, although being mathematically inconsistent.

In order to confirm the low influence of this additional term in the mathematical model, simulations using a mass density flux of 10.0 kg/(m^{2}s) were performed. The value of this mass density flux is so high that it may be considered even physicaly impossible. However, the intention is to determine whether this additional term may interfere with the numerical results for extremely high intensities of phase change. The bubble initial radius was 0.1 m and the simulation final time was 0.01 s, when the bubble radius was twice the initial radius.

According to the numerical results obtained, the bubble radius prediction was accurate even for a high mass density flux. The difference between the exact solution and the computed bubble radius at the simulation's final time was lower than 1.0%. Fig. 5.83 shows the magnitude of the

effects of the surface tension force compared to the magnitude of the additional force term from the simulation considering $\dot{m}'' = 10.0$.

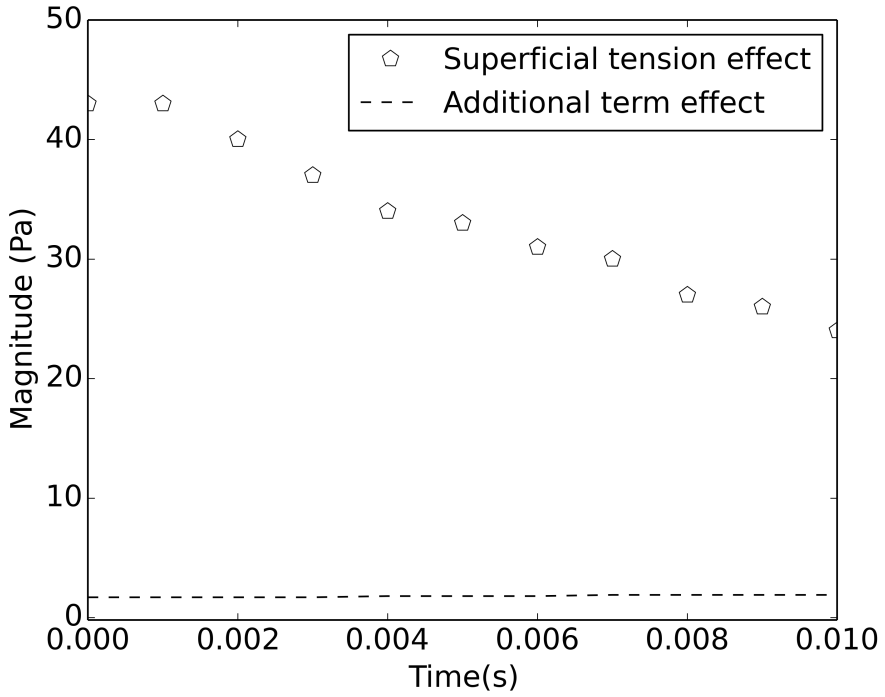

Figure 5.83: Magnitude of the effects from the surface tension force compared to the additional force using the Delta method considering $\dot{m}'' = 10.0$.

The magnitude of the effects from the additional term is about two orders of magnitude lower than the surface tension force effects. Therefore, as seen in Fig. 5.83, the additional force term here discussed may be considered irrelevant to phase change problems.

5.9 Case study of two-phase flow with phase change: Direct contact condensation jet with cross-flow

The present work models a turbulent saturated water vapor jet injected normal to a cross-flow of water liquid. This case is inherently complex due to the production of several types of turbulent and vortical structures distributed at several regions in the flow field. The case becomes even more complex due to condensation occuring at the interface since the phase change phenomenon leads to a significant change of the flow field (XU *et al.*, 2016).

Previous works on DCC of a vapor jet in liquid reported in the literature were mainly focused on jet penetration length and condensation regime diagram; on the other hand, there is

a lack of several flow field information, such as detailed velocity charcateristics of the turbulent jet (XU *et al.*, 2016).

Computational simulations were performed to investigate the flow field characteristics of the turbulent jet induced by direct contact condensation of steam jet in cross-flow of water in a vertical channel. The present work focuses on the velocity and temperature field investigation as well as the study of the jet centerline trajectory.

5.9.1 Physical model

A vertical channel was used to model the case of vapor condensing jet in cross-flow with liquid water. The physical model employed to perform the simulations of the jet in cross-flow consisted of a vertical channel with inner square cross-section of $30.0m$ and $60.0m$ long. The steam is injected through an spherical hole with diameter of $2.0m$.

Small injection Reynolds number requires lower requirement of spatial and temporal resolution compared to high injection Reynolds number (CLERX *et al.*, 2011), then the present work uses a relatively low mass flux and low injection number as the previous experimental work of Clerx *et al.* (2011), Clerx, Geld e Kuerten (2013).

A saturated water vapor jet subjected to a subcooled liquid water cross-flow in a vertical channel was modelled using the mathematical and numerical model previously described. The computational simulations were performed using non-structured grids and a time step of $0.001s$.

The steam jet velocity was 29,0 m/s and the liquid cross-flow velocity was 0.29m/s. The steam mass flux G, was defined as $44kg/m^2s$ and the momentum ratio J was fixed as 15. Reynolds number of the steam was approxitemaly 6200 and the Raynolds number of the water cross-flow was 10000. The Jakob number was 220.

The physical problem modelled here represents a complex phenomenon where the termophysical properties are subjected to strong variations between the vapour and liquid phases. The physical properties ratio between the phases are given by the following expressions:

- ρ_{liq}/ρ_{vap}=700
- μ_{liq}/μ_{vap}=165
- Cp_{liq}/Cp_{vap}=2.1

- k_{liq}/k_{vap}=25

5.9.2 Data and statistical analysis

In order to validate the jet condensing simulation, the jet's trajectory was compared to the experimental results from Clerx *et al.* (2011). The literature presents mainly two ways to define the jet centerline trajectory, namely, the temperature and velocity fields (XU *et al.*, 2016). Since Clerx *et al.* (2011) employed the temperature field to obtain the jet centerline, the present work was focused on validate the simulation using the jet temperature center lines as Clerx *et al.* (2011).

The temperature center line is defined by the location of the local highest temperature, since the vapor presents the highest values of temperature, the position of the temperature center line is related to the jet location in the domain.

In order to collect the information of velocity and temperature from the computational domain, 1800 probes were positioned at the center xz-plane which computed the local and instantaneous temperatures and velocities. The temperature field varied significantly in time according to the flow dynamics, therefore a temporal mean temperature was extracted from each probe.

In order to compute an accurate temporal mean temperature, the simulation duration was based on the stabilization of temperature field at a probe located at the channel's top (at the end of the computational domain).

The figure 5.84 shows the variations of the temperature at a probe located near the channel's top.

According to the figure 5.84, after 10 seconds, the temperature variation follows a regular pattern. Then, the data used for validation purpose was considered after 10 seconds.

5.9.3 Computational results

When steam is injected into cross-flow, steam rapidly start the condensation process near the steam injection point. Then, the jet becomes a single-phase turbulent jet. The jet never impinges the wall opposite to the injection point. The penetration is relatively low due to the small value of momentum ratio.

The figure 5.85 shows a three-dimensional view from the condensing jet interface at the

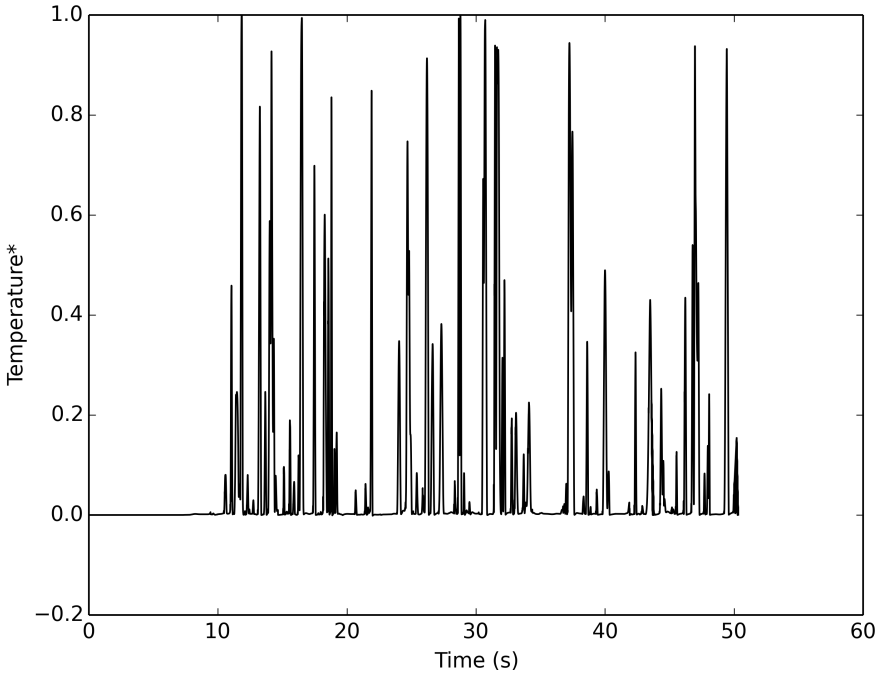

Figure 5.84: Dimensionless temperature at the probe near the computational domain exit at the channel's top.

computational domain at time 45s.

Steam is injected at a relatively low mass flux through a small hole in a lateral wall of the channel. The steam condenses intermittently in a small area close to the inlet. As expected, a high-temperature zone occurs near the center of the velocity jet which was previously reported by Clerx *et al.* (2011). As previously reported by Clerx *et al.* (2011), the steam penetration is intermittent.

As previously reported by the literature, the interface shape and trajectory is complex and intermittent. There is a great number of vapour pockets and bubbles in the computational domain moving in high speed. Three-dimensional effects are proeminent according to the figure 5.85, illustrating the need of modelling this complex physical problem using a 3D computational plataform. The figure 5.86 shows the interface contour at the beggining of the simulation time.

The three-dimensional effects are evident, as previously reported by Clerx *et al.* (2011). The topology of the steam-liquid interface during the direct contact condensation is not smooth beacuse of the waves and interface instabilities which causes an apparent interface roughening (CLERX *et al.*, 2011).

The adaptive mesh refinement (AMR) saved great computational time since it reduced the

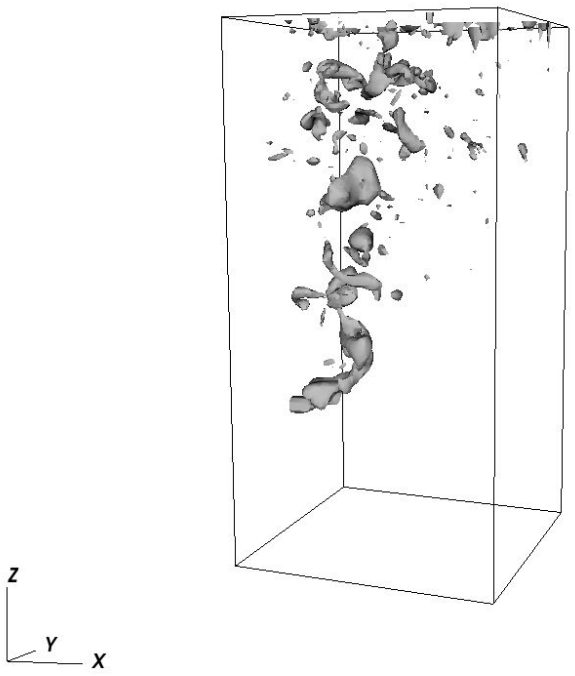

Figure 5.85: Interface of the condensing jet at simulation time of 45s.

need of a fine mesh in some regions of the computational domain. The AMR was particularly important at the simulation beggining when only a small region of the domain required a fine mesh. The figure 5.87 shows the mesh configuration at different times near the simulation beggining.

According to Clerx, Geld e Kuerten (2013), the area close to the steam injection point presents large velocity fluctuations, where the information about temperature and velocity may be innaccurate. Clerx, Geld e Kuerten (2013) named this unstable region as 'steam pocket', where the velocity collected were submitted to a special statistical treatment due to the large temporal variations.

According to Xu *et al.* (2016), for high jet Reynolds number, the jet penetration is relatively long and even hits the opposite wall. On the other hand, for relative low jet Reynolds number, the jet penetration is relatively shorter.

Clerx *et al.* (2011) presented a correlation to predict the temperature center line for a given

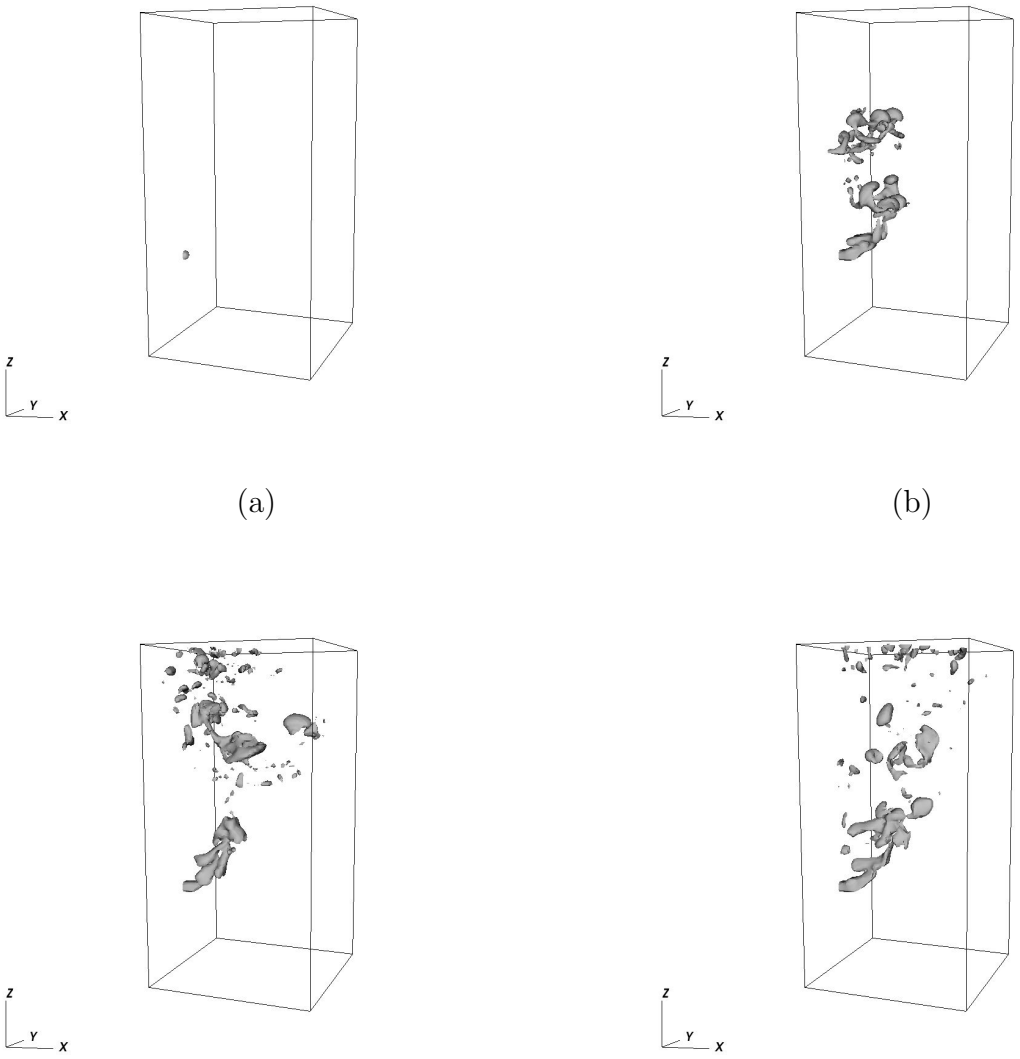

Figure 5.86: Interface contour of the jet at t=0s (a), t=0.005s (b), t=0.010s (c), t=0.015s (d).

coordinate:

$$x/rd = 1.3\,(y/rd)^{0.3} \tag{5.27}$$

The figure 5.88 shows the jet trajectory from the present work and from the experimental results from Clerx *et al.* (2011). where the value rd is given by the following expression:

$$rd = 2r\sqrt{J} \tag{5.28}$$

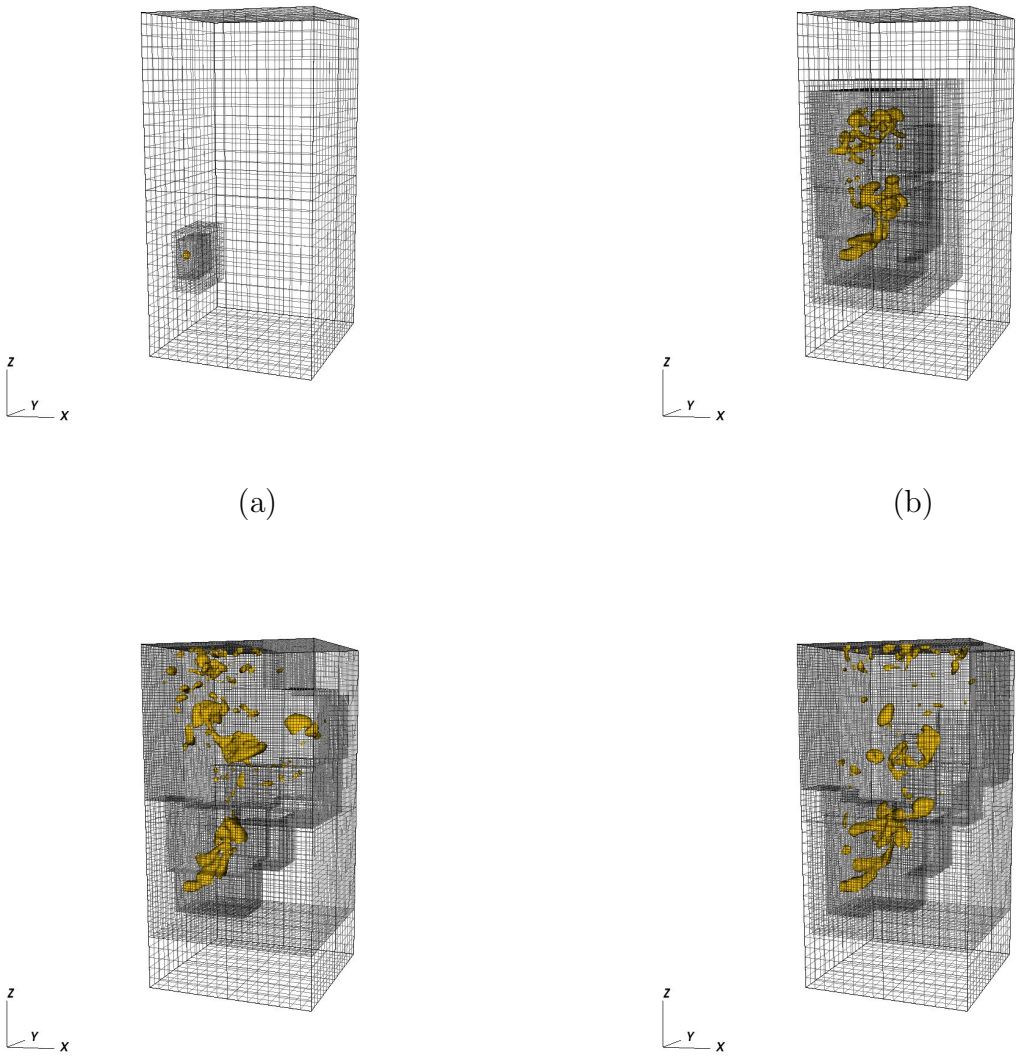

(a) (b)

(c) (d)

Figure 5.87: Mesh configuration and interface contour of the jet at t=0s (a), t=0.005s (b), t=0.010s (c), t=0.015s (d).

where J is the momentum ratio given by the expression:

$$J = \frac{\rho_v \vec{v}_v^2}{\rho_l \vec{v}_l^2} \tag{5.29}$$

According to the figure 5.88, the computational results from the jet trajectory are in good agreement with the experimental results from Clerx *et al.* (2011). The difference between the results obtanied from the present work and the literature were evaluated using the L2 norm and it was found the error of 1.5%.

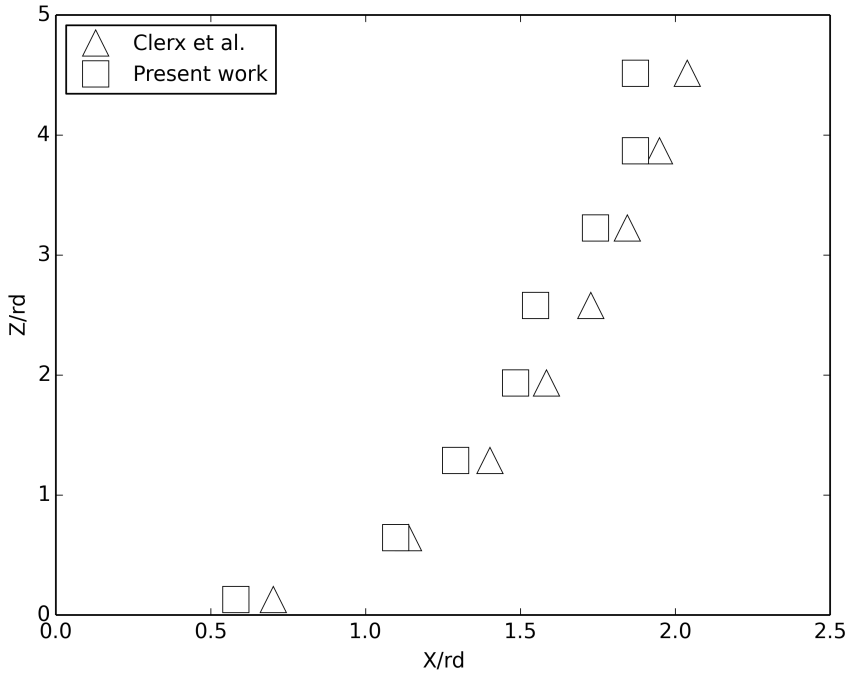

Figure 5.88: Jet centerline trajectory according to the results from the present work and from Clerx et al.

The AMR promoted great reduction at the simuation time required, especially at the beggining of the physical phenomenon. Even near at the simulation time end, AMR reduced the computational power required as figure 5.89 shows.

The figure 5.89 shows the interface and the mesh configuration at the simulation time of 45s.

The case study presented in this section llustrates the potential of the MFSim code to perform complex simulations with phase change. Therefore, the present thesis has achieved its main goals and this case study represents the beggining of new investigations to the MFLab laboratory in the research line of phase change using CFD. Future works on new analysis with this case of cross-flow are proposed later.

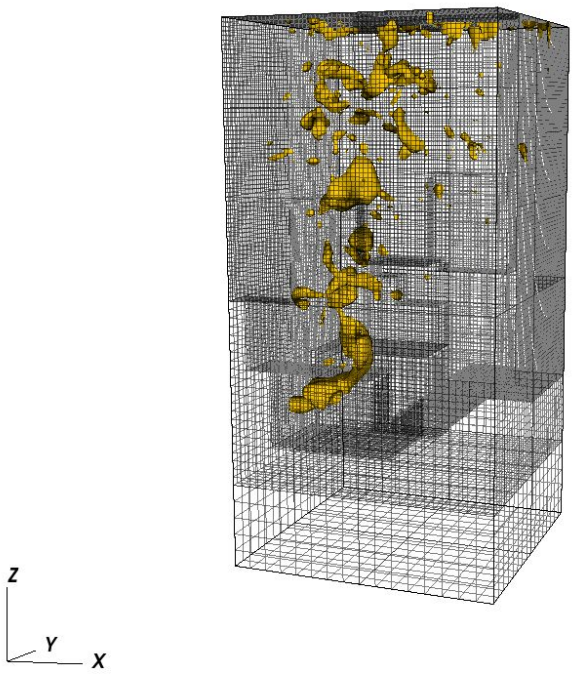

Figure 5.89: Interface of the condensing jet and the mesh configuration at the simulation time of 45s.

CHAPTER VI

CONCLUSIONS

In the present thesis, the authors have developed the first work, from the MFLab research group, focused on the study of non-isothermal two-phase flows. The main goals of this work was the study of a mathematical, numerical and computational model of two-phase flows in non-isothermal flows with and without phase change. The thesis achieved all the main and specific objetives proposed in the thesis plan proposed at the beggining of the graduation.

The main objective of the present thesis was accomplished and now the MFSim code has a phase change model for pure substances with a methodology which was validated and computationally verified. All the specific objetives were also achieved and several original contributions were obtained from the present work.

The first conclusion from the present work is the recommendation of using the non-divergent form of energy equation for two-phase flows as suggested by the literature. The divergent form of energy equation may be numerically inconsistent to model different materials close one to each other when subjected to the same temperature, which corroborates with literature previous works. The use of the non-divergent form of energy equation provided excelent results without numerical difficulties of convergence. The divergent form of energy equation provided also excelent results, however as the physical properties ratio between the two phases increases, the convergence becomes more challenging.

The investigation about the influence of Prandlt number on thermal transfer rate have

presented several numerical results demonstrating that the overall Prandlt number affects directly the local thermal transfer rate in the problems studied. Therefore, refuting some literature premisses, the inclusion of a dispersed phase itself does not increase local thermal transfer rate, as seen in some numerical results from the present work.

The OB and NOB provided adequate thermal transfer rate results; however, the differences between the literature and OB were higher than for NOB. Therefore, NOB is presented as a useful mathematical formulation for modeling incompressible flows with a temperature-dependent specific mass approach in single-phase or multiphase problems instead of solving the full compressible mathematical formulation. In addition, the differences between the literature and OB results increased as the Rayleigh number was raised, especially in the turbulent regime. The results of the NOB were closer to the literature than were those of the OB for the entire range of Rayleigh numbers tested. Therefore, the numerical results confirmed the higher accuracy of NOB compared to OB despite the NOB's still being an approximate model. Lastly, flow visualization allowed the identification of coherent turbulent structures near the cavity walls in the simulation with Rayleigh number 10^{10}. The presence of hairpin and Tollmien–Schlichting instabilities revealed the importance of modeling the three-dimensional effects of natural convection in the turbulent regime.

The evaluation of spurious currents in phase change problems using a diffuse interface treatment for pressure showed the presence of important spurious currents for mass density fluxes higher than 0.1 kg/m^2s. Since the latter ratio is considered a moderate phase change intensity, the diffuse interface treatment may be considered a good numerical method.

The evaluation of the influence of the recoil force in phase change problems demonstrated none relevant influence in the interface behavior. More studies should be conducted in order to quantify this force as well as to propose new ways of modelling the recoil effect.

The additional term discovered in the present thesis from the non-divergent form of momentum equation in phase change problems was considered not important in the mathematical model.

The adaptive mesh refinement (AMR) strategy is an interesting numerical tool allowing the reduction of time and computational power required in phase change problems. The AMR efficiency computed in several cases simulated demonstrated the importance of using AMR instead

of uniform grids without affecting the accuracy of the results found.

Finally, the case study of a water condensing vapour jet in cross-flow with liquid water demonstrated the high potential of the model developed in the present thesis to investigate complex flows with phase change.

CHAPTER VII

FUTURE WORKS

The implemented phase change model in MFSim code could be extended to model multicomponent flows, allowing the performance of some engineering applications where a mixture of substances simultaneously are subjected to phase change. In order to make progress in the extension of the phase change model, it would be necessary to follow the next steps:

- The transport of multiple scalars would be coupled with the phase change model;
- Different source terms would be included in the mathemacal model to account the effect of multiple substances simultaneously boiling;
- The input data would allow the user to include the information about the substances to be investigated in the phenomenon or a external bibliotec as Cantera would be called.

The eulerian phase change model studied in the present thesis could be coupled with a lagrangin phase change model which has being developed in MFSim code recently. The combination of both methods would allow the performance of simulations of phase change which has a great industrial interest.

Since the variations of the Grashof and the Prandlt numbers presented an important impact on the thermal transfer rate in non-isothermal flows; the authors suggest the performance of similar simulations, however using smaller physical domains. In addition, it would be interesting to model the influence of these dimensionless numbers considering multiple bubbles.

From the study between the traditional Oberbeck-Boussinesq approximation and the new approach of a temperature-dependent specific mass approach, we recommend the performance of simulations for even higher Rayleigh number, e. g. $Ra > 10^{10}$. It is expected that OB would fail to model excessively turbulent flows while the proposed NOB approach would produce accurate results.

The performance of more complex simulations are recommended to evaluate the influence of the recoil force in phase change problems, especially in problems where large temperature gradients at the interface are not uniform.

BIBLIOGRAPHYC REFERENCES

AKHTAR, M.; KLEIS, S. Boiling flow simulations on adaptive octree grids. *International journal of multiphase flow*, v. 53, p. 88–99, 2013. Disponível em: <http://dx.doi.org/10.1016/j.ijmultiphaseflow.2013.01.008>.

ANDREWS, M. J.; DALZIEL, S. B. Small atwood number rayleighâtaylor experiments. *Philosophical transactions of the royal society*, v. 368, p. 1663–1679, 2010. Disponível em: <http://dx.doi.org/10.1098/rsta.2010.0007>.

BERENSON, P. J. Film boiling heat transfer from a horizontal surface. *Jornal of Heat Transfer*, v. 83, p. 351–356, 1961. Disponível em: <http://dx.doi.org/10.1115/1.3682280>.

BOUSSINESQ, J. Theorie analytique de la chaleur. *Gauthier-Villars*, v. 2, 1903. Disponível em: <http://dx.doi.org/10.1017/CBO9780511693229>.

BRACKBILL, J. U.; KOTHE, D. B.; ZEMACH, C. A continuum method for modeling surface-tension. *Journal of Computational Physics*, v. 100, p. 335–354, 1992. Disponível em: <http://dx.doi.org/10.1016/0021-9991(92)90240-Y>.

BUKHARI, S.; SIDDIQUI, M. Characteristics of air and water velocity fields during natural convection. *Heat mass transfer*, v. 43, p. 415–525, 2007. Disponível em: <http://dx.doi.org/10.1007/s00231-005-0072-8>.

CENTRELLA, J. M.; WILSON, J. R. Planar numerical cosmology. ii - the difference equations and numerical tests. *The Astrophysical Journal Supplement Series*, v. 54, p. 229–249, 1984. Disponível em: <http://dx.doi.org/10.1086/190927>.

CHANDRA, A.; CHHABRA, R. P. Effect of prandtl number on natural convection heat transfer from a heated semi-circular cylinder. *International Journal of Mechanical, Aerospace, Industrial, Mechatronic and Manufacturing Engineering*, v. 6, p. 106–113, 2012. Disponível em: <http://dx.doi.org/10.1016/j.ces.2014.09.006>.

CHEN, Z.; UTAKA, Y. On heat transfer and evaporation characteristics in the growth process of a bubble with microlayer structure during nucleate boiling. *International Journal of Heat and Mass Transfer*, v. 81, p. 750–759, 2015. Disponível em: <http://dx.doi.org/10.1016/j.ijheatmasstransfer.2014.10.058>.

CHORIN, A. J. Numerical solution of the Navier–Stokes equations. *Mathematics of Computation*, v. 22, p. 745–762, 1968. Disponível em: <http://dx.doi.org/10.1090/s0025-5718-1968-0242392-2>.

CLERX, N.; DEURZEN, L. G. M. van; PECENKO, A.; LIEW, R.; GELD, C. W. M. van der; KUERTEN, J. G. M. Temperature fields induced by direct contact condensation of steam in a cross-flow in a channel. *Heat and mass transfer*, v. 47, p. 981–990, 2011. Disponível em: <http://dx.doi.org/10.1007/s00231-011-0868-7>.

CLERX, N.; GELD, C. van der; KUERTEN, J. G. Turbulent stresses in a direct contact condensation jet in cross-flow in a duct with implications for particle break-up. *International journal of heat and mass transfer*, v. 66, p. 684–694, 2013. Disponível em: <http://dx.doi.org/10.1016/j.ijheatmasstransfer.2013.07.062>.

COWAN, G. H.; LOVEGROVE, P. C.; QUARINI, G. L. Turbulent natural convection heat transfer in vertical single water-filled cavities. *International heat transfer conference 7*, v. 15, p. 195–203, 1982.

DABIRI, S.; TRYGGVASON, G. Heat transfer in turbulent bubbly flow in vertical channels. *Chemical engineering science*, v. 122, p. 106–113, 2015. Disponível em: <http://dx.doi.org/10.1016/j.ces.2014.09.006>.

DARBOULI, M.; METIVIER, C.; LECLERC, S.; NOUAR, C.; BOUTEERA, M.; STEMMELEN, D. Natural convection in shear-thinning fluids experimental investigations by MRI. *International Journal of Heat and Mass Transfer*, v. 95, p. 742–754, 2016. Disponível em: <http://dx.doi.org/10.1016/j.ijheatmasstransfer.2015.12.056>.

DECKWER, W. D. On the mechanism of heat transfer in bubble column reactor. *Chemical Engineering Science*, v. 92, p. :1341–1346, 1980. Disponível em: <http://dx.doi.org/10.1016/0009-2509(80)85127-X>.

DEEN, N.; KUIPERS, J. Direct numerical simulation of wall-to liquid heat transfer in dispersed gas-liquid two-pahse flow using a volume of fluid approach. *Chemical Engineering Science*, v. 102, p. 268–282, 2013. Disponível em: <http://dx.doi.org/10.1016/j.ces.2013.08.025>.

F. DUARTE, B. A. de; M. M. VILLAR, R. R. da S. Melo an; SERFATY, R.; SILVEIRA NETO, A. da. An extension of oberbeckâboussinesq approximation for thermal convection problems. *Journal of the Brazilian Society of Mechanical Sciences and Engineering*, v. 40, p. 201–225, 2018. Disponível em: <http://dx.doi.org/10.1007/s40430-018-1181-x>.

FRANCOIS, M. M.; CUMMINS, S. J.; DENDY, E. D.; KOTHE, D. B.; SICILIAN, J. M.; WILLIAMS, M. W. A balanced-force algorithm for continuous andsharp interfacial surface tension models within avolume tracking framework. *Journal of Computational Physics*, v. 213, p. 141–173, 2006. Disponível em: <http://dx.doi.org/10.1016/j.jcp.2005.08.004>.

GERMANO, M.; PIOMELLI, U.; MOIN, P.; CABOT, W. H. A dynamic subgrid-scale eddy viscosity model. *Physics of Fluids A: Fluid Dynamics*, v. 3, p. 1760–1765, 1991.

GRAY, D. D.; GIORDINI, A. The validity of the boussinesq approximation for liquids and gases. *International journal of heat and mass transfer*, v. 19, p. 545–551, 1976. Disponível em: <http://dx.doi.org/10.1016/0017-9310(76)90168-X>.

HAELSSIG, J.; THIBAULT, A.; ETEMAD, S. Direct numerical simulation of interphase heat and mass transfer in multicomponent vapour-liquid flows. *International journal of heat and mass transfer*, v. 53, p. 3947–3960, 2010. Disponível em: <http://dx.doi.org/10.1016/j.ijheatmasstransfer.2010.05.013>.

HARVIE, D.; DAVIDSON, M.; RUDMAN, M. An analysis of parasitic current generation in volume of fluid simulations. *Applied Mathematical Modelling*, v. 30, p. 1056–1066, 2006. Disponível em: <http://dx.doi.org/10.1016/j.apm.2005.08.015>.

HIRT, C. W.; NICHOLS, B. D. Volume of fluid (vof) method for the dynamics of free boundaries. *Journal of Computational Physics*, v. 39, p. 201–225, 1981. Disponível em: <http://dx.doi.org/10.1016/0021-9991(81)90145-5>.

JURIC, D.; TRYGGVASON, G. Computations of boiling flows. *International journal of multiphase flow*, v. 24, p. 387–410, 1998. Disponível em: <http://dx.doi.org/10.1016/S0301-9322(97)00050-5>.

KAMEI, S.; HIRATA, M. Condensing phenomena of a single vapor bubble into subcooled water. *Experimental Heat Transfer*, v. 3, p. 173–182, 1990. Disponível em: <http://dx.doi.org/10.1080/08916159008946385>.

KANG, S.; IACCARINO, G.; HAM, F. Dns of bouyancy-dominated turbulent flows on a bluff body using the immersed boundary method. *Journal of Computational Physics*, v. 228, p. 3189–3208, 2009. Disponível em: <http://dx.doi.org/10.1016/j.jcp.2008.12.037>.

KIM, D. G.; JEON, C. H.; PARK, I. S. Comparison of numerical phase-change models through stefan vaporizing problem. *International Communications in Heat and Mass Transfer*, v. 87, p. 228–236, 2017. Disponível em: <http://dx.doi.org/10.1016/j.icheatmasstransfer.2017.07.013>.

KITANO, T.; NISHIO j.; KUROSE, R.; KOMORI, S. Effects of ambient pressure, gas temperature and combustion reaction on droplet evaporation. *Combustion and Flame*, v. 161, p. 551–564, 2014. Disponível em: <http://dx.doi.org/10.1016/j.combustflame.2013.09.009>.

KRANE, R. J.; JESSEE, J. Some detailed field measurements for a natural convection flow in a vertical square enclosure. *Proceedings of the first ASME-JSME Thermal Engineering Joint Conference*, v. 1, p. 323–329, 1983.

LEE, M. S.; R., A.; AUTE, V. Direct numerical simulation of incompressible multiphase flow with phase change. *Journal of Computational Physics*, v. 344, p. 381–418, 2017. Disponível em: <http://dx.doi.org/10.1016/j.jcp.2017.04.073>.

LEONG, W. H.; HOLLANDS, K. G. T.; BRUNGER, A. P. Experimental nusselt numbers for a cubical cavity benchmark problem in natural convection. *International journal of heat and mass transfer*, v. 42, p. 1979–1989, 1999. Disponível em: <http://dx.doi.org/10.1016/S0017-9310(98)00299-3>.

LESIEUR, M. *Turbulence in Fluids*. Berlin: Springer-Verlag, 2008.

LILLY, D. A proposed modification of the germano subgrid-scale closure method. *Physics of Fluids A: Fluid Dynamics*, v. 4, p. 633, 1992.

LIU, X.-D.; FEDKIW, R.; KANG, M. A boundary condition capturing method for poissonâs equation on irregular domains. *Journal of Computational Physics*, v. 160, p. 151–178, 2000. Disponível em: <http://dx.doi.org/10.1006/jcph.2000.6444>.

MANUILOVICH, S. V. A new technique of Tollmien–Schlichting wave cancellation in a sound-exposed boundary layer. *Nonlinear Instability of Nonparallel Flows*, v. 96, p. 160–163, 1994. Disponível em: <http://dx.doi.org/10.1007/978-3-642-85084-413>.

MARKATOS, N. C.; PERICLEOUS, K. A. Laminar and turbulent natural convection in an enclosed cavity. *International journal of heat and mass transfer*, v. 27, p. 755–772, 1984. Disponível em: <http://dx.doi.org/10.1016/0017-9310(84)90145-5>.

MONTIEL-GONZALEZ, M.; HINOJOSAB, J.; VILLAFÃ¡N-VIDALESC, H.; BAUTISTA-OROZCOC, A.; ESTRADA, C. Theoretical and experimental study of natural convection with surface thermal radiation in a side open cavity. *Applied Thermal Engineering*, v. 75, p. 1176–1186, 2015. Disponível em: <http://dx.doi.org/10.1016/j.applthermaleng.2014.05.047>.

NIKOLAYEV, V.; CHATAIN, D.; GARRABOS, Y.; BEYSENS, D. Experimental evidence of the vapor recoil mechanism in the boiling crisis. *Physical Review Letters*, v. 97, p. 253–260, 2016. Disponível em: <http://dx.doi.org/10.1103/PhysRevLett.97.184503>.

NIKOLOPOULOS, N.; THEODORAKAKOS, A.; BERGELES, G. A numerical investigation of the evaporation process of a liquid droplet impinging onto a hot substrate. *Intenational Journal of heat and mass transfer*, v. 50, p. 303–319, 2007. Disponível em: <http://dx.doi.org/10.1016/j.ijheatmasstransfer.2006.06.012>.

NINGEGOWDA, B. M.; PREMACHANDRAN, B. A coupled level set and volume of fluid method with multi-directional advection algorithms for two-phase flows with and without phase change. *International Journal of Heat and Mass Transfer*, v. 79, p. 532–550, 2014.

ORESTA, P.; VERZICCO, R.; LOHSE, D.; PROSPERETTI, A. Heat transfer mechanisms in bubbly rayleigh-bÃ©nard convection. *Physical review*, v. 80, p. 259–293, 2007. Disponível em: <http://dx.doi.org/10.1103/PhysRevE.80.026304>.

PADILLA, E.; LOURENCO, M.; SILVEIRA-NETO, A. Natural convection inside cubical cavities: numerical solutions with two boundary conditions. *Journal of the Brazilian Society of Mechanical Sciences and Engineering*, v. 35, p. 275–283, 2013. Disponível em: <http://dx.doi.org/10.1007/s40430-013-0033-y>.

PAN, Z.; WEIBEL, J.; GARIMELLA, S. V. A saturated-interface-volume phase changemodel for simulating flow boiling. *International journal of heat and mass transfer*, v. 93, p. 945–956, 2016. Disponível em: <http://dx.doi.org/10.1016/j.ijheatmasstransfer.2015.10.044>.

PATEL, G.; TANSKANEN, V.; R.KYRKI-RAJAMÃ¤KI. Numerical modelling of low-reynolds number direct contact condensation in a suppression pool test facility. *Annals of Nuclear Energy*, v. 71, p. 376–387, 2014. Disponível em: <http://dx.doi.org/10.1016/j.anucene.2014.04.009>.

PESKIN, C. S. The fluid dynamics of heart valves: experimental, theoretical and computational methods. *Annual Reviews*, v. 14, p. 235–259, 1982. Disponível em: <http://dx.doi.org/10.1146/annurev.fl.14.010182.001315>.

POLING, B. E.; PRAUSNITZ, J. M.; O'CONNELL, J. P. The properties of gases and liquids. *McGraw-Hill*, 2001. Disponível em: <http://dx.doi.org/10.1036/0070116822>.

QIU, R.; WANG, A.; JIANG, T. Lattice boltzmann method for natural convection with multi-component and multiphase fluids in a two-dimensional square cavity. *The canadian journal of chemical engineering*, v. 92, p. 1121–1129, 2014. Disponível em: <http://dx.doi.org/10.1002/cjce.21950>.

RAGHUPATHI, P. A.; KANDLIKAR, S. G. Bubbe growth and departure trajectory under asymetric temperature conditions. *International journal of heat and mass transfer*, v. 95, p. 824–832, 2016. Disponível em: <http://dx.doi.org/10.1016/j.ijheatmasstransfer.2015.12.058>.

ROACHE, P. J. Verification of codes and calculations. *AIAA Journal*, v. 36, p. 696–702, 1998. Disponível em: <http://dx.doi.org/10.2514/2.457>.

ROBERTS, M. S.; JACOBS, J. W. The effects of forced small-wavelength, finite-bandwidth inital pertubations and miscibility on the turbulent rayleigh-taylor instability. *Journal of fluid mechanics*, v. 787, p. 50–83, 2016. Disponível em: <http://dx.doi.org/10.1017/jfm.2015.599>.

S., S. G.; CANDLER, G. V.; DIMOTAKIS., P. Baroclinic torque and implications for subgrid-scale modeling. *7th AIAA Theoretical Fluid Mechanics Conference*, p. 1–13, 1991. Disponível em: <http://dx.doi.org/10.2514/6.2014-3214>.

SAMKHANIANI, N.; ANSARI, M. R. Numerical simulation of bubble condensation using cf-vof. *Progres in nuclear energy*, v. 89, p. 120–131, 2016. Disponível em: <http://dx.doi.org/10.1016/j.pnucene.2016.02.004>.

SCRIVEN, L. E. On the dynamics of phase change. *Chemical Engineering Science*, v. 10, p. 1–13, 1959. Disponível em: <http://dx.doi.org/10.1016/0009-2509(96)81820-3>.

SHARP, D. H. An overview of rayleigh-taylor instability. *Physica*, v. 12, p. 3–18, 1984. Disponível em: <http://dx.doi.org/10.1016/0167-2789(84)90510-4>.

STROTOS, G.; GAVAISES, M.; THEODORAKAKOS, A.; BERGELES, G. Numerical investigation of the evaporation of two-component droplets. *Fuel*, v. 90, p. 1492–1507, 2011. Disponível em: <http://dx.doi.org/10.1016/j.fuel.2011.01.017>.

TAMARI, M.; NISHIKAWA, K. The stirring effect of bubbles upon the heat transfer to liquids. *Heat transfer â japonese research*, v. 5, p. 31–44, 1976. Disponível em: <http://dx.doi.org/10.1299/kikai1938.33.87>.

TANGUY, S.; MENARD, T.; BERLEMONT, A. A level set method for vaporizing two-phase flows. *Journal of Computational Physics*, v. 221, p. 837–853, 2007.

TANGUY, S.; SAGAN, M.; LALANNE, B.; COUDERC, F.; COLIN, C. Benchmarks and numerical methods for the simulation of boiling flows. *Journal of Computational Physics*, v. 264, p. 1–22, 2014. Disponível em: <http://dx.doi.org/10.1016/j.jcp.2014.01.014>.

TANSKANEN, V.; JORDAN, A.; PUUSTINEN, M.; KYRKI-RAJAMÃ¤KI, R. Cfd simulation and pattern recognition analysis of the chugging condensation regime. *Annals of Nuclear Energy*, v. 66, p. 133–143, 2014. Disponível em: <http://dx.doi.org/10.1016/j.anucene.2013.12.007>.

TRYGGVASON, G. Numerical simulations of the rayleigh-taylor instability. *Journal of computational physics*, v. 75, p. 253–282, 1988. Disponível em: <http://dx.doi.org/10.1016/0021-9991(88)90112-X>.

TRYGGVASON, G.; LU, J. Direct numerical simulations of flows with phase change. *Procedia IUTAM*, v. 15, p. 2–13, 2015. Disponível em: <http://dx.doi.org/10.1016/j.piutam.2015.04.002>.

TRYGGVASON, G.; SCARDOVELLI, R.; ZALESKI, S. [S.l.: s.n.].

TSUI, Y.; LIN, S. W.; LAI, Y. N.; WU, F. C. Phase change calculations for film boiling flows. *International journal of heat and mass transfer*, v. 70, p. 745–757, 2014. Disponível em: <http://dx.doi.org/10.1016/j.ijheatmasstransfer.2013.11.061>.

WACHEM, B. G. M.; SCHOUTEN, J. C. Experimental validation of 3-d lagragian vof model: bubble shape and rise velocity. *AIChE Journal*, v. 48, p. 253–282, 2002. Disponível em: <http://dx.doi.org/10.1002/aic.690481205>.

WAN, D.; PATNAIK, B.; WEI, G. A new benchmark quality solution for the buoyancy-driven cavity by discrete singular convolution. *Numericaal heat transfer*, v. 40, p. 199–228, 2001. Disponível em: <http://dx.doi.org/10.1080/104077901752379620>.

WANG, P.; ZHANG, Y.; GUO, Z. Numerical study of three-dimensional natural convection in a cubical cavity at high rayleigh numbers. *International Journal of Heat and Mass Transfer*, v. 113, p. 217–228, 2017. Disponível em: <http://dx.doi.org/10.1016/j.ijheatmasstransfer.2017.05.057>.

WELCH, S. W. J.; WILSON, J. A volume of fluid based method for fluid flows with phase change. *Journal of Computational Physics*, v. 160, p. 662–682, 2000. Disponível em: <http://dx.doi.org/10.1006/jcph.2000.6481>.

WHITE, F. M. Viscous fluid flow. *McGraw-Hill.*, 1974.

WISSEN, R. J. E. van; SCHREEL, K.; GELD, C. W. M. van der. Particle image velocimetry measurements of a steam-driven confined turbulent water jet. *Journal of Fluid Mechanics*, v. 530, p. 353–368, 2005. Disponível em: <http://dx.doi.org/10.1017/S0022112005003769>.

XU, Q.; GUO, L.; CHANG, L.; WANG, Y. Velocity field characteristics of the turbulent jet induced by direct contact condensation of steam jet in crossflow of water in a vertical pipe. *International Journal of Heat and Mass Transfer*, v. 103, p. 305–318, 2016. Disponível em: <http://dx.doi.org/10.1016/j.ijheatmasstransfer.2016.07.047>.

YANG, Y.; PAN, L.-M.; XU, J.-J. Effects of microgravity on marangoni convection and growth characteristic of a single bubble. *Acta Astronautica*, v. 100, p. 129–139, 2014. Disponível em: <http://dx.doi.org/10.1016/j.actaastro.2014.04.005>.

ZARE, S.; JAMALKHOO, M. H.; PASSANDIDEH-FARD, M. Experimental study of direct contact condensation of steam jet in water flow in a vertical pipe with square cross section. *International Journal of Multiphase Flow*, v. 1, p. 74–88, 2018. Disponível em: <http://dx.doi.org/10.1016/j.ijmultiphaseflow.2018.03.009>.

ZEYTOUNIAN, R. K. Joseph boussinesq and his approximation: a contemporary view. *Comptes Rendus Mecanique*, v. 331, p. 575–586, 2003. Disponível em: <http://dx.doi.org/10.1016/S1631-0721(03)00120-7>.

ZOHOU, L.; WANG, L.; CHONG, D.; YAN, J.; LIU, J. Cfd analysis to study the effect of non-condensable gas on stable condensation jet. *Progress in nuclear energy*, v. 98, p. 143–152, 2017. Disponível em: <http://dx.doi.org/10.1016/j.pnucene.2017.03.011>.